LA-8758-MS

A Compact-Toroid Fusion Reactor Based on the Field-Reversed Theta Pinch

University of California

LOS ALAMOS SCIENTIFIC LABORATORY
Post Office Box 1663 Los Alamos, New Mexico 87545

CONTENTS

A COMPACT-TOROID FUSION REACTOR BASED ON THE FIELD-REVERSED THETA PINCH

by

R. L. Hagenson and R. A. Krakowski

ABSTRACT

Early scoping studies based on approximate, analytic models have been extended on the basis of a dynamic plasma model and an overall systems approach to examine a Compact Toroid (CTOR) reactor embodiment that uses a Field-Reversed Theta Pinch as a plasma source. The field-reversed plasmoid would be formed and compressionally heated to ignition prior to injection into and translation through a linear burn chamber, thereby removing the high-technology plasmoid source from the hostile reactor environment. Stabilization of the field-reversed plasmoid would be provided by a passive conducting shell located outside the high-temperature blanket but within the low-field superconducting magnets and associated radiation shielding. On the basis of this batch-burn but thermally steady-state approach, a reactor concept emerges with a length below ~ 40 m that generates 300-400 MWe of net electrical power with a recirculating power fraction less than 0.15.

I. INTRODUCTION

In order to facilitate the assessment of reactor potential for Alternative Fusion Concepts (AFC), a three-tiered structure has been established wherein a Level I study (Engineering Design Phase) is the most detailed, and a Level III study (Conceptual Physics Design Phase) is the most preliminary. The highest level of study (Level I) would include, in a multiman-year effort, considerable conceptual design and economics analysis, in addition to sophisticated, state-of-the-art physics and operating-point analyses. The lowest level of study (Level III) would characterize less understood and developed confinement schemes using relatively simple physics models and parametric analysis of potential reactor operating points. Generally, a Level III study would not provide a reactor embodiment <u>per se</u>,

and, because of obvious gaps in the physics understanding of these relatively unexplored concepts, only a range of potential reactor operating points may be parametrically identified. This study is based on time-dependent burn models that incorporate results from a developing experimental and theoretical data base in describing the plasma behaviour. The resulting confidence in the plasma model coupled with a reactor system that appears to require only near state-of-the-art technology classifies this study of a Compact-Toroid Reactor (CTOR) somewhere near the Level II, although only preliminary identification of major subsystem parameters is performed. Additional more detailed work is required in order to substantiate or to disprove the initially positive prognoses that has emerged from the work reported herein.

A Compact Toroid (CT) is a plasma configuration in which no magnetic coils or structural walls extend through the torus, as is schematically illustrated in Fig. I-1. Although conceptually not a new idea,[1] interest in this configuration was re-kindled with the proposal of the Spheromak reactor.[2,3] The level of interest in CT reactors is reflected by international

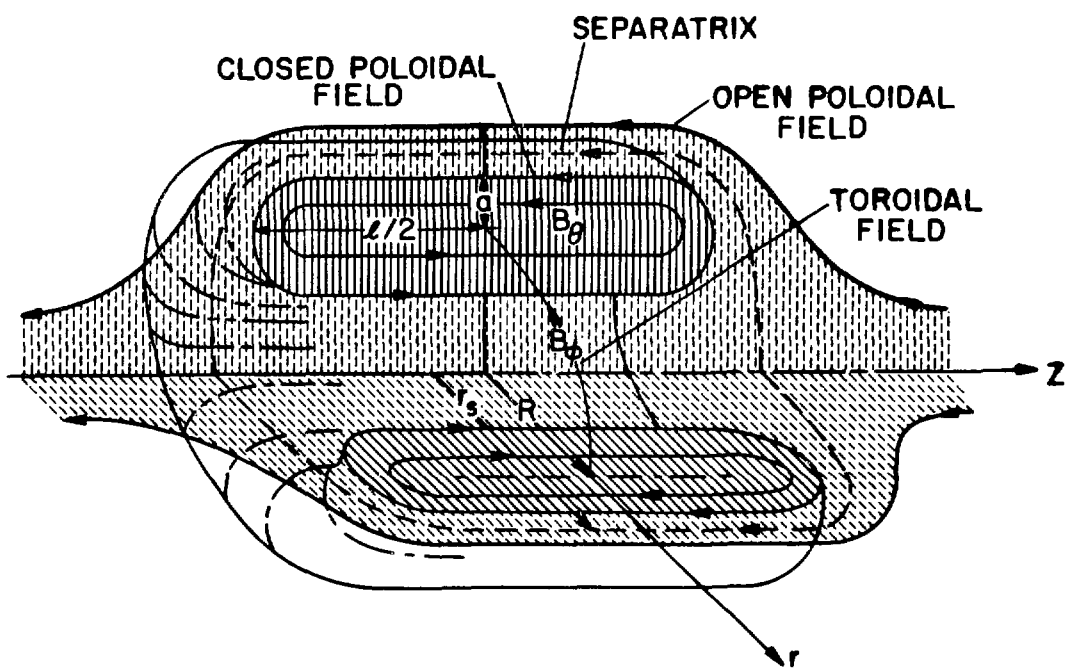

Fig. I-1. Schematic diagram of Compact Torus plasma configuration. For some CT configurations the toroidal field, B_ϕ, is zero.

workshops[3,4] on that topic and the large number of conceptual reactors that have been proposed and/or designed around the CT configuration: Field-Reversed Mirror (FRM);[5-7] the moving-ring FRM;[8-10] the moving-ring Spheromak;[11-13] the slowly-imploding liner (LINUS);[14-15] the Trigger-Reconnected Adiabatically-Compressed Torus (TRACT);[16,17] Astron-like ion-ring devices;[17-20] and the Field-Reversed Theta-Pinch (FRΘP) reactor (CTOR).[21] In one instance even the Reversed-Field Pinch (RFP)[22,23] has been claimed[13] as a member of the CT family. Generally, plasmoids without toroidal field are classified as Field-Reversed Configurations (FRC), whereas systems containing toroidal fields are termed spheromaks.

The CT reactor systems (Sec. III) may be categorized, according to Fig. I-2, as using either a steady-state or a pulsed plasmoid. The key questions that must be addressed for each approach are also shown on Fig. I-2 in terms of startup, stability/equilibrium and plasma engineering. No steady-state CT reactor with <u>in situ</u> plasma production has yet been identified. The spheromak[2,3] and field-reversed mirror (FRM)[5-7] are produced by a flux core and plasma gun/beam, respectively, and consequently are translated into a final position for steady-state operation. Crucial equilibria/stability questions must be addressed for these steady-state configurations, requiring the imposition of a number of stabilization techniques including a conducting shell, axis-encircling particles (AEP), finite-Larmor-radius (FLR) effects, multipole fields and quite probably an active feedback system. Upon achieving a stable configuration, additional plasma engineering problems, including fueling, heating, impurity/ash control, flux drive and profile control, must be overcome to maintain a steady-state system with no first-wall pulsed temperature rise. Circumvention of many of these problems leads to pulsed systems.

The pulsed-plasma systems shown in Fig. I-2 are categorized as translating <u>versus</u> stationary. The LINUS[14,15] and TRACT[16,17] reactors envisage a stationary plasma within an engineering system that uniquely combines many reactor functions. The LINUS reactor uses a liquid-metal liner (first wall) to compress and to contain the plasma, while the TRACT approach integrates a shock-heating plasma source with the reactor burn section. The TRACT device introduces stability/equilibrium questions when attempting to use <u>in situ</u> shock heating to achieve a large radius plasma, $r_s/r_c > 0.5$, whose 0.5-s plasma burn is stabilized by a conducting shell.

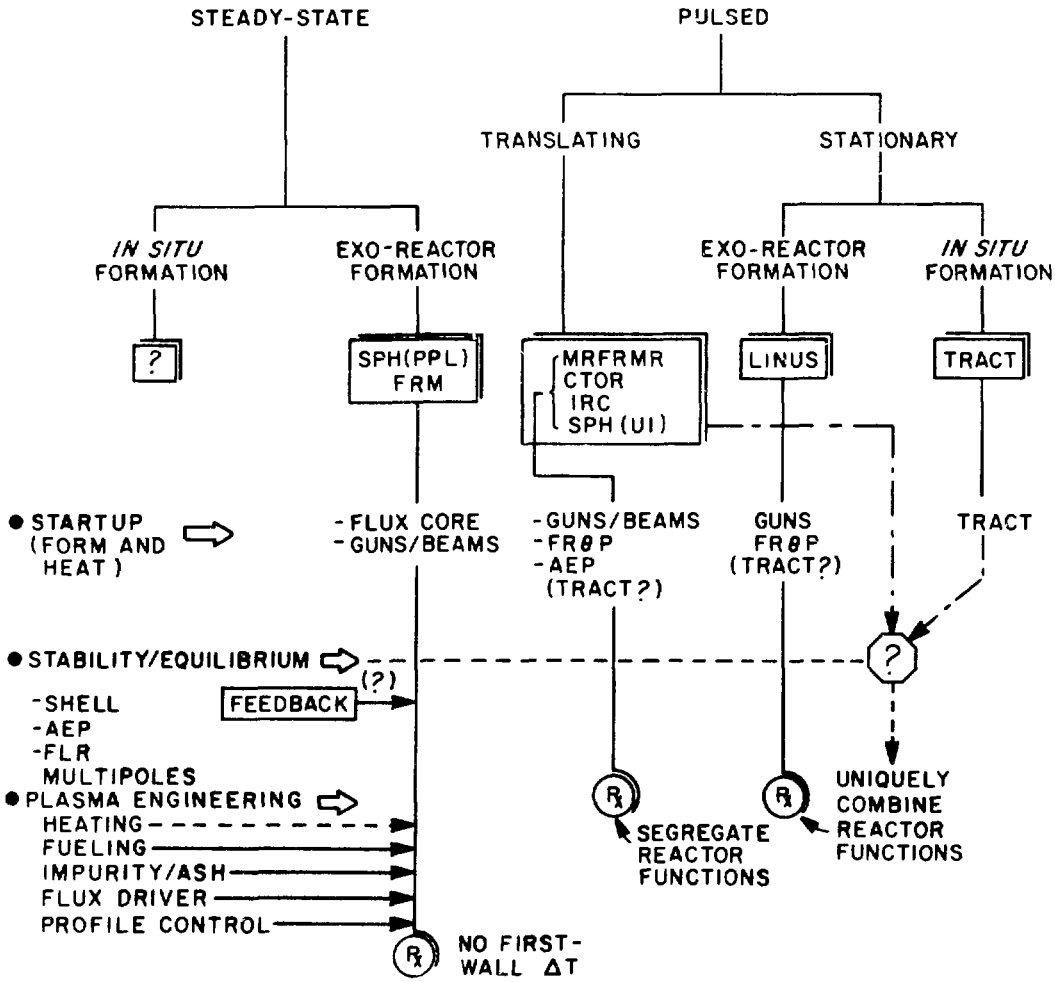

Fig. I-2. Categorization of CT reactor studies.[4]

Attempting to avoid many of the difficulties associated with the stationary-plasmoid reactors, the remaining pulsed systems propose to translate the plasmoid through a linear burn chamber. The Moving-Ring Field Reversed Mirror Reactor (MRFRMR)[8-10], Compact Toroid Reactor (CTOR)[21] and Ion-Ring Compressor (IRC)[20] are similar in overall conceptual design. Highly-prolate ($\ell/r_s \gtrsim 7$) systems (CTOR) require substantial conducting shell stabilization, while adding high-energy axis-encircling particles should provide substantial stabilization requiring less influence from an external shell (MRFRMR and IRC) and allowing the use of less prolate plasmoid shapes ($\ell/r_s \gtrsim 2$). The spheromak is also proposed in a translating configuration although a prolate plasmoid should be used to ensure equilibrium inside the conducting shell. Since the spheromak must be oblate in order to satisfy general equilibrium/stability constraints, this plasmoid configuration is incompatible with the requirements of a translating plasmoid that is stabilized by a conducting shell.

The reactor potential purported by the aforementioned design studies is listed in Table I-I. Key issues that must be addressed by all studies are listed in Table I-II and are also shown schematically in Fig. I-2.

TABLE I-I

COMPACT-TOROID REACTOR PROMISE

- Small plasmoid sizes leading to relatively small reactors.
  - Simpler, less costly systems
  - More flexibility, many approaches may be tried with mistakes less costly in time and dollars.
- High beta and power density.
- Natural "divertor", particle flux (i.e., alpha-particle power) not directed to first wall; possible to use direct conversion at plasma exit region of reactor.
- Primary confinement provided by steady-state superconducting magnets.
- Allows effective use of adiabatic compressional heating (Appendix C).
- Possible to segregate key functions/subsystems (i.e., high technology regions placed external to fusion neutron environment).

TABLE I-II

COMPACT-TOROID REACTOR ISSUES

- Startup/formation
  - In situ
  - Exo-reactor formation
- Equilibrium/Stability
  - Passive conducting shell
  - Axis encircling particles (formation, sustenance, energy)
  - Effects of finite-Larmor radius stabilization
  - Effects of multipole fields
  - Possible requirement of active feedback
- Transport
  - Confinement
  - Stability (profiles)
  - Fueling (generally burn time greater than particle confinement time)
- Steady-state operation
  - How to replenish dissipating magnetic flux?
  - How to maintain profiles?
  - Plasma engineering problems (fueling, heating, alpha-particle ash removal and impurity control).

The approach taken by the Level II CT reactor study reported herein utilizes as much as possible that which is rather than that which might be. Specifically, a FROP is selected to form an elongated field-reversed configuration (i.e., no toroidal field) which is translated through a linear burn section. To minimize source and pulsed power requirements, a tapered axial compressor section, driven by a traveling wave network, maintains the first wall/magnet coil close to the plasma surface, while the translating plasmoid is adiabatically compressed to ignition. The translating FRC would be stabilized by a passive conducting shell that assures the required ratio of

separatrix-to-conductor radius. Plasmoid translational power is provided by simply tapering the conducting shell. The CTOR design reported herein operates with a batch burn and reflects as much as possible a "design-to-state-of-the-art" philosophy. It is recognized, however, that both theoretical and experimental progress in the near future may alter considerably the design approach adopted for this study. This approach is based on preliminary trade-off studies reported in Ref. 21 as a Level III Conceptual Physics Design.

The major assumptions made in arriving at this CTOR design are: stabilization by a passive conducting shell is possible within shell-to-plasmoid radius constraints given by relatively small experiments; energy confinement times are given by scaling laws obtained from tokamak experiments (i.e., Alcator or 200 Bohm); nearly constant particle inventories are assumed during the burn period (i.e., few seconds), implying particle confinement times, τ_p, much longer than energy confinement times, τ_E, or considerable injestion of neutral density if $\tau_p \simeq \tau_E$. Lastly, active feedback of either gross or local MHD modes is not invoked by the CTOR design reported herein; active feedback systems placed within the reactor environment is considered unattractive compared to stabilization by a passive, exo-blanket shell and present understanding of CT equilibrium/stability is not sufficiently developed at this time to permit a quantitative analysis of the physics/technology requirements of an in-blanket active feedback system.

The scope of this study includes in Sec. VII the preliminary plant layout and identification of major subsystem specifications. In Sec. II an executive summary gives the plasma model, reactor operating scenario and design point determination. The design point is also presented along with a description of the preliminary plant layout. A review of previous CT reactor designs is presented in Sec. III. Details of the reactor operating scenario, energy balance computation and reactor physics model is given in Sec. IV. A parametric evaluation of numerous design points is given in Sec. V. with the characteristics of the final design point that has emerged from this study listed in Sec. VI. Concluding remarks and suggested future directions are given in Sec. VIII.

II. EXECUTIVE SUMMARY

A. Operating Scenario

The CTOR proposes the use of a Field-Reversed Theta Pinch (FRΘP) to produce external to the reactor an FRC plasmoid that is subsequently heated and translated through a linear burn chamber. The high-voltage plasmoid source and compressional heater are removed from the burn chamber to a less hostile environment. The stabilizing conducting shell would be positioned between the blanket and shield. Translation of the ignited plasmoid, shown schematically on Fig. II-1 allows portions of the conducting shell that have not experienced flux diffusion to be continually "exposed". A nearly (thermal) steady-state operation of the first wall and blanket is possible for appropriate plasmoid speeds and injection rates. Locating the stabilizing

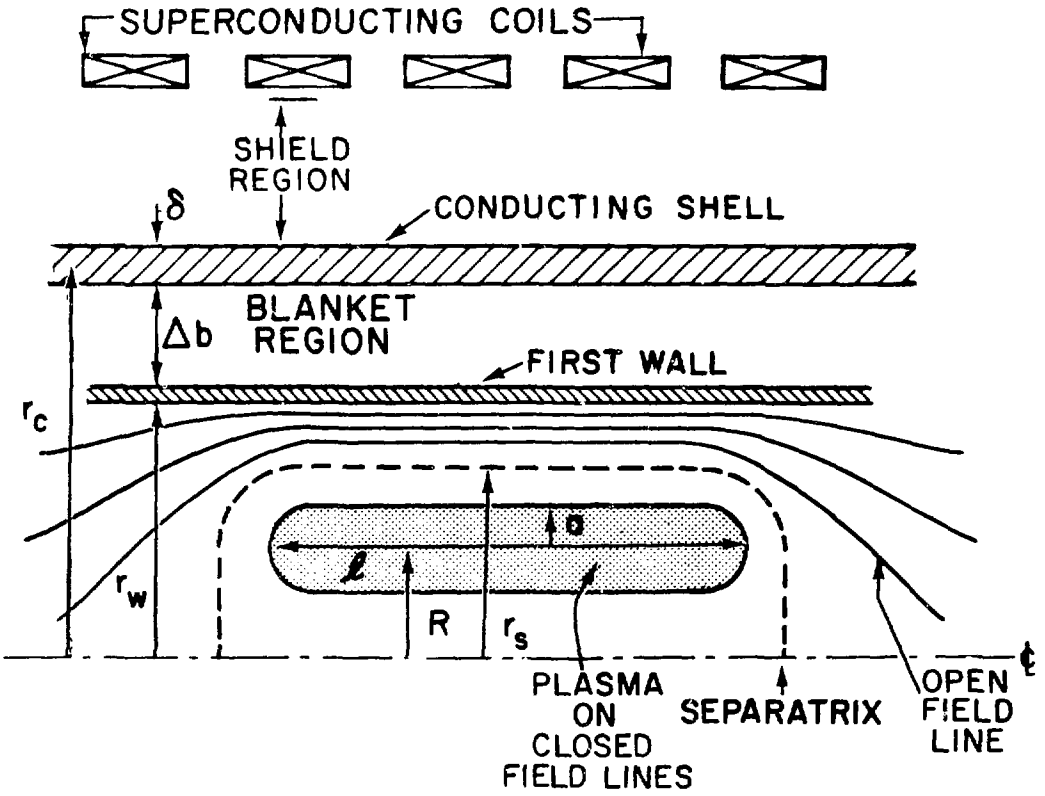

Fig. II-1. Compact toroid geometry showing radius of conduction shell, r_c, first wall, r_w, separatrix, r_s, and plasmoid length, ℓ. This FRC plasmoid would be stabilized by a passively conducting shell of current radius r_c and thickness δ. This shell is located outside a breeding blanket of thickness Δb = 0.5 m.

conduction shell outside the blanket permits room-temperature operation and minimizes the translational power, which appears as Joule-heating losses in the exo-blanket shell; for the operating conditions chosen these losses can be supplied directly by alpha-particle heating through modest radial expansion of the plasmoid inside a slightly flared conducting shell, blanket and first wall. Translational runaway is prevented by the presence of a thin (~ 1-mm) first-wall "shell" that is highly permeable to magnetic flux penetration but which nevertheless stabilizes the linear motion of the FRC down the linear burn chamber. Superconducting coils are located outside the blanket, conducting shell and radiation shield to provide a continuous bias field that is compressed between the conducting shell and the plasmoid; MHD stability would thereby be provided throughout the burn without invoking active feedback stabilization.

The plasma simulation code used to model the CTOR is based on a three-particle, time-dependent zero-dimensional ("point-plasma") model that incorporates an analytical equilibrium expression[24] (Appendix B), allowing three-dimensional spatial variations to be followed computationally in time. Starting with the post-implosion (FRΘP) phase, the plasma trajectory is followed through the tapered compression chamber into the burn section where conducting shell losses (translational drag) are supplied by radial plasma expansion that in turn is driven by alpha-particle heating. Referring to Fig. II-1, the required radius of the conducting shell, r_c, which is positioned outside a blanket of thickness, Δb = 0.5 m and the plasmoid length, ℓ, are defined by experimental results ($x_s = r_s/r_c \gtrsim 0.5$ and $\ell/r_c \gtrsim 3.5$). In addition to the plasma burn dynamics, an overall energy balance is performed, as is shown in Fig. II-2, along with a spatial calculation of thermal and structural response of the first wall.

Parameter studies using the plasma simulation code were performed for a range of plasmoid radii, reactor lengths, plasma densities and confinement time scalings. A plasmoid is produced by the FRΘP at 1.6 keV and is subsequently compressed to 8 keV in 0.1 s, requiring a radial compression ratio of ~ 2.9 and a reduction of ~ 1.9 in the axial dimension according to the assumed equilibrium relationships. The ignited plasmoid enters the burn chamber with an initial plasmoid velocity equal to 2-5 times ℓ/τ_s, where the electrical skin time of the stabilizing shell, τ_s, describes the decay of magnetic flux within the annular area between the first wall and the plasma

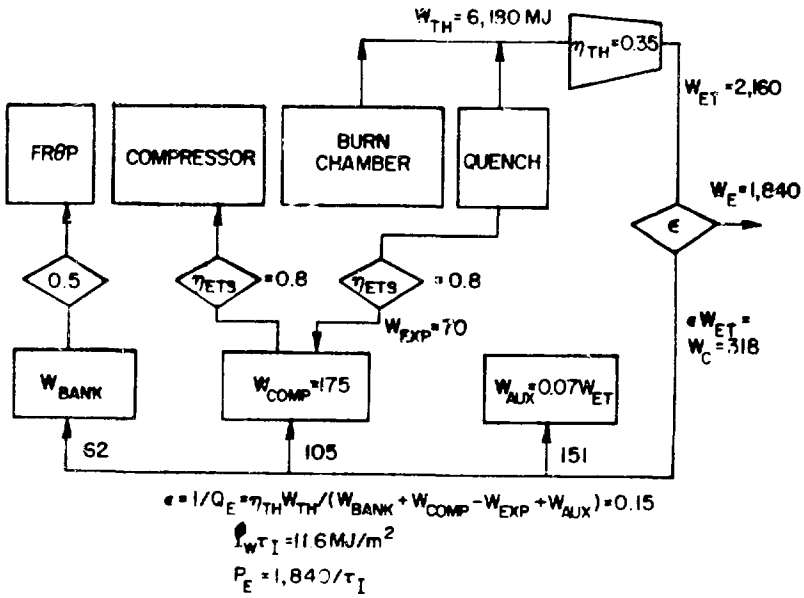

Fig. II-2. Energy balance for the Compact Toroid Reactor (CTOR). The CTOR energy balance includes the FRΘP capacitor bank, W_{BANK}, homopolar motor/generator, W_{COMP}, auxiliary, W_{AUX}, total thermal, W_{TH}, gross electric, W_{ET} net electric, W_E and circulating energy, W_C. The energy transfer/storage efficiencies shown have been used throughout this study and for the operating conditions assumed are considered to be conservative.

separatrix. The velocity of the plasmoid is reduced during the translation by tailoring the flare of the burn chamber in order to maintain a constant first-wall neutron current along the length of the burn chamber while simultaneously assuring that the alpha-particle-driven plasma expansion supplies all drag (Joule) losses incurred in the passive stabilizing shell. The plasmoid velocity varies approximately as $v \propto P_\alpha/r_w$, where $P_\alpha(W)$ is the instantaneous alpha-particle power. Motion proceeds until $v/(\ell/\tau_s) \lesssim 1$ at which time the translation is terminated and the plasma expansion/quench phase is allowed to occur.

Results from a typical burn trajectory are shown in Fig. II-3 for an assumed energy confinement equal to 200 Bohm times. This energy loss rate is extrapolated from tokamak experiments and has been subjected to parametric study (Appendix D). The plasmoid is assumed not to lose particles during the

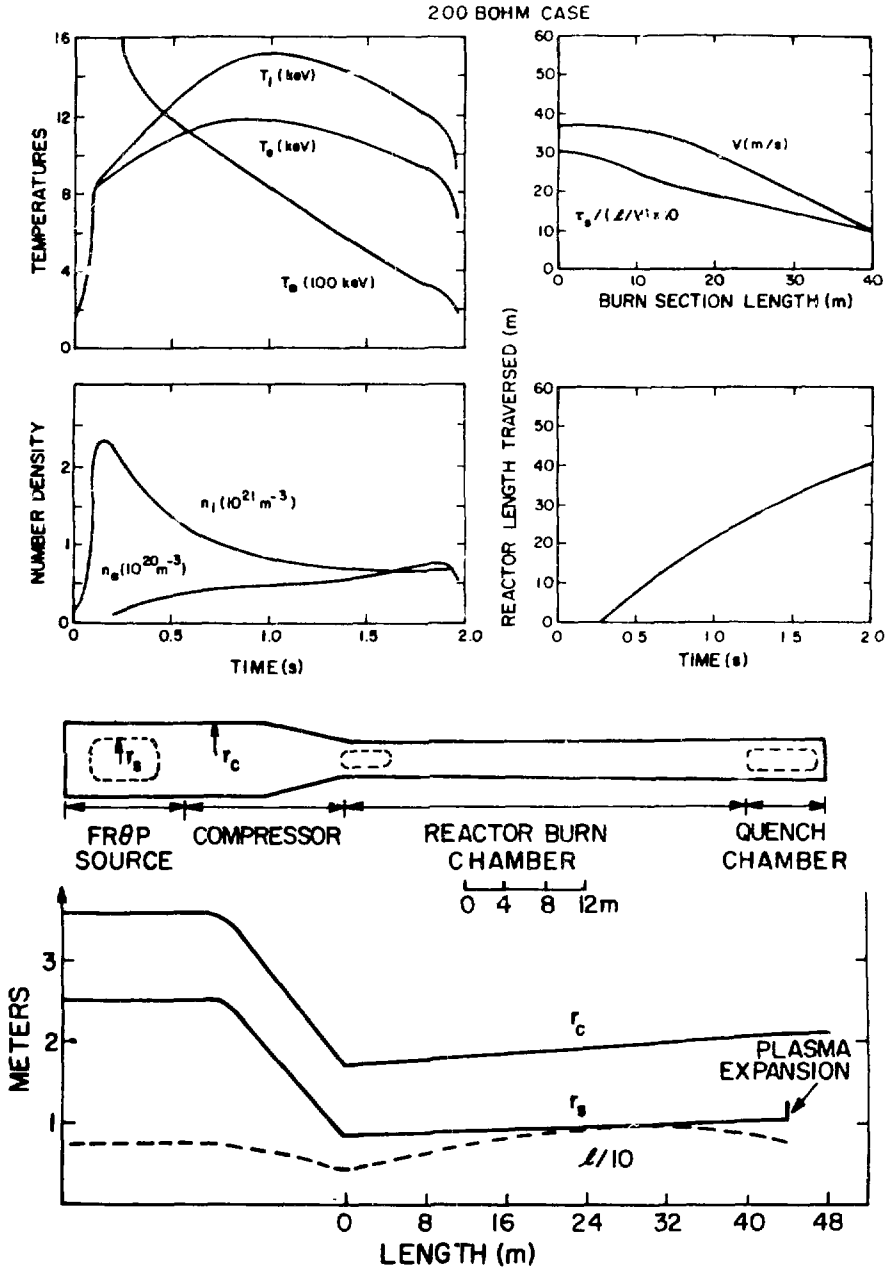

Fig. II-3. Sample CTOR plasma burn response showing the time dependence of plasma temperature, T_e, T_i and T_α, the plasmoid velocity, v, or $\tau_s/(\ell/v)$, the plasma density, n_e and the plasmoid and conductor dimensions along the length of the burn chamber.

1-2 s trajectory down the linear burn chamber. In effect, if the particle confinement time is on the order of τ_E, complete particle recycle with a cold

gas blanket surrounding the slowly moving plasmoid is assumed to occur. A thermally-stable burn results at a nearly optimal temperature (Fig. II-3A) of $T_i \simeq 10\text{-}14$ keV, achieving a fuel burnup of $f_B \sim 0.17$ in $\tau_B = 1.96$ s for the sample case shown in Fig. II-3. The burn is terminated as fuel depletion, alpha-particle burnup and plasmoid expansion result in losses that ultimately overcome alpha-particle heating. The taper required of the conducting shell needed to compensate for translational drag (Joule) losses in the stabilizing shell is shown in Fig. II-3C for both an actual geometrical scale and an exaggerated scale, the latter better illustrating radial variations. The first-wall radius must increase from 1.2 m to 1.64 m over a total reactor (burn section) length of 40 m for a conducting shell thickness of $\delta = 0.05$ m. Specifying the first-wall neutron loading to be uniform over the reactor length requires the plasmoid velocity to decrease from an initial 38 m/s to 10 m/s at the burn-chamber outlet (Fig. II-3B), where the ratio, r_v, of actual velocity to minimum allowed velocity (ℓ/τ_s) is also plotted. The reactor length traversed, as defined by the trailing edge of the FRC, is also given as a function of time in Fig. II-3B. The CTOR response depicted in Fig. II-3 is typical of the optimal design point reported quantitatively in the following section.

B. Design Point

The design point finally chosen utilizes a confinement time equal to 200 Bohm times, which also yields the same results as Alcator scaling. These confinement scalings produce attractive reactor designs at relatively low thermal power and minimized FROP source sizes (Sec. V., Fig. V.-17). The physics parameters for this design are listed in Table II-I.

The energy flow for this reactor design point is listed in Table II-II, from which the recirculating power, as described in Sec. IV.B., is computed. These energy flows are also listed on the energy diagram given in Fig. II-2. The system power is specified by choosing the injection time, τ_I. Taking $\tau_I = 5.8$ s to give a 14.1 MeV neutron wall loading of 2 MW/m^2, a thermal output of 1050 MWt results with a net electric power of 310 MWe for an engineering Q-value (inverse of recirculating power, ε) of $Q_E = 6.8$ ($\varepsilon = 0.15$) and $\eta_{TH} = 0.35$. Listed in Table II-III are key engineering parameters for this CTOR design point.

TABLE II-I

PHYSICS PARAMETERS FOR CTOR DESIGN POINT

PARAMETER	VALUE (INLET/OUTLET)
Separatrix radius, r_s(m)	0.85/1.05
Plasmoid length, ℓ(m)	5.0/8.0
Conducting-shell radius, r_c(m)	1.7-2.1
Shell skin time, τ_ε(s)	0.48/0.8
Burn time, τ_B(s)	1.95
Energy confinement time, τ_E(s)	0.1
Plasmoid translational velocity, v(m/s)	30/10
Plasma density, n_i ($10^{21}/m^3$)	2.5/0.5
Plasma temperature, T_i(keV)	~ 15
Ion-gyroradii in column, R/ρ_{io} [(a)]	170
Ion-gyroradii in minor radius, $S = a/\rho_i$ [(b)]	30.
Beta, $\beta_s = 1 - 0.5\ x_s^2$	0.87
Separatrix ratio, $x_s = r_s/r_c$	0.5
Burnup, f_B	0.17
Lawson parameter, $n\tau_B$(10^{20} s/m^3)	21.0

(a) Value of ρ_{io} calculated using vacuum field.

(b) Value of ρ_i uses one-half vacuum field value. Actual sheath width expected to be 0.33 of this value (Appendix A).

C. Preliminary Plant Layout

A preliminary plant layout for the CTOR is shown in Fig. II-4. Future engineering studies will focus on the mechanical and electrical design of the FR@P source and the compressional heater, rather than the relatively standard technology expected to be associated with the linear burn chamber.

For this 300-MWe CTOR power plant, the plasma is formed in a FR@P driven by a 62-MJ, 20-kV capacitor bank. A 175-MJ homopolar motor/generator powers the traveling-wave-network compressor which increases the plasma temperature from 1.5 to 8 keV at the inlet of the burn section. A 48-m long burn/quench section consists of 24 cylindrical 2-m-long modules with a solenoidal superconducting coil located every 4-m (12 required). A beam dump is provided at both ends to intercept the neutron streaming with most of the alpha-

TABLE II-II

ENERGY INVENTORY FOR CTOR DESIGN POINT[a]

PARAMETER	VALUE (MJ)
Initial plasma	16.4
Final plasma	81.7
Neutron (16.5 MeV/n)	5090.
Alpha particle	1090.
Direct conversion	32.6
Bremsstrahlung	9.1
Thermal conduction	897.
Trapped poloidal flux (quench)	7.0
Quench	88.8
Total thermal, W_{TH}	6170.
Conducting shell transport losses[b]	46.3
Auxiliary, W_{AUX}	151.
ETS losses (η_{ETS} = 0.8), W_{ETS}	80.
FROP source bank, W_{BANK}	61.8
Homopolar compressor, W_{COMP}	175.
Homopolar recharge at quench, W_{EXP}	70.
Gross electric (η_{TH} = 0.35)	2160.
Circulating electric	318.
Net electric	1840.

[a]Refer to CTOR energy balance, Fig. II-2.

[b]Provided by alpha-particle expansion of the FRC plasmoid.

particle energy retained by the plasmoid (i,e., transport losses incurred during the traverse along the burn chamber) expected to exit the quench end of the device and be extracted thermally. Flaring the magnetic field at the quench section into a 40-m-radius x 8-m-long cylindrical beam dump (Sec. VII.B.3) provides 200 m^2 of heat transfer area.

The burn section could be similar to the nuclear island used in the Reverse-Field Pinch Reactor.[22,23] The 0.5-m thick stainless steel blanket would contain a 40 v/o Li_2O packed bed into which penetrates radially oriented water steam cooled U-tubes. A low-pressure (0.1 MPa) helium purge gas is

TABLE II-III

CTOR ENGINEERING PARAMETERS

PARAMETER	VALUE (INLET/OUTLET)
Burn section first-wall radius, r_w(m)	1.2/1.6
Burn section length, L(m)	40
Superconducting coil field, B_s(T)	3.1/1.5
Required FROP energy, W_{BANK}(MJ)	62
Required compressor section energy, W_{COMP}(MJ)	175
Burn time, τ_B(s)	2.0
Injection time, τ_I(s)	5.8
First-wall loading, I_W(MW/m^2)	2.0
Engineering Q-value, Q_E	6.8
Recirculating power fraction, ε	0.15
Total thermal power, P_{TH} (MWt)	1050
Gross electric, P_{ET}(MWe)	365
Recirculating power, P_c(MWe)	55
Net electric power, P_E(MWe)	310
Thermal conversion efficiency, η_{TH}	0.35
Plant efficiency, $\eta_p = \eta_{TH}(1-\varepsilon)$	0.30

drifted t' .ough the granular Li_2O bed to extract tritium as an oxide. The slightly superheated (5-K) steam emerging from this blanket would be used to drive a turbogenerator. Despite the pulsed (plasma) nature of the burn, the inherent thermal capacity of this blanket results in less than a 5-K temperature excursion within the blanket structure, although a 1.0-mm-thick copper first-wall undergoes a bulk rise of 26 K (ΔT = 6 K across the material, leading to thermal stresses of 1.2 MPa at the inlet end of the burn chamber,. A shield composed of a 0.1-m thick lead and a 1.4-m thick borated-water region protects the relatively low field (1.5-3.0 T) NbTi-Cu superconducting magnet coils (15 MA/m^2 average current density exclusive of support structure) from thermal loading and neutron/gamma-ray damage. Each of the 2-m long burn section modules would be electrically and thermohydraulically independent. The solenoidal field coils would be fixed structures that are adequately spaced to permit removal of the shield and blanket modules. The magnet coils and shield modules are of equal dimensions along the length of the burn

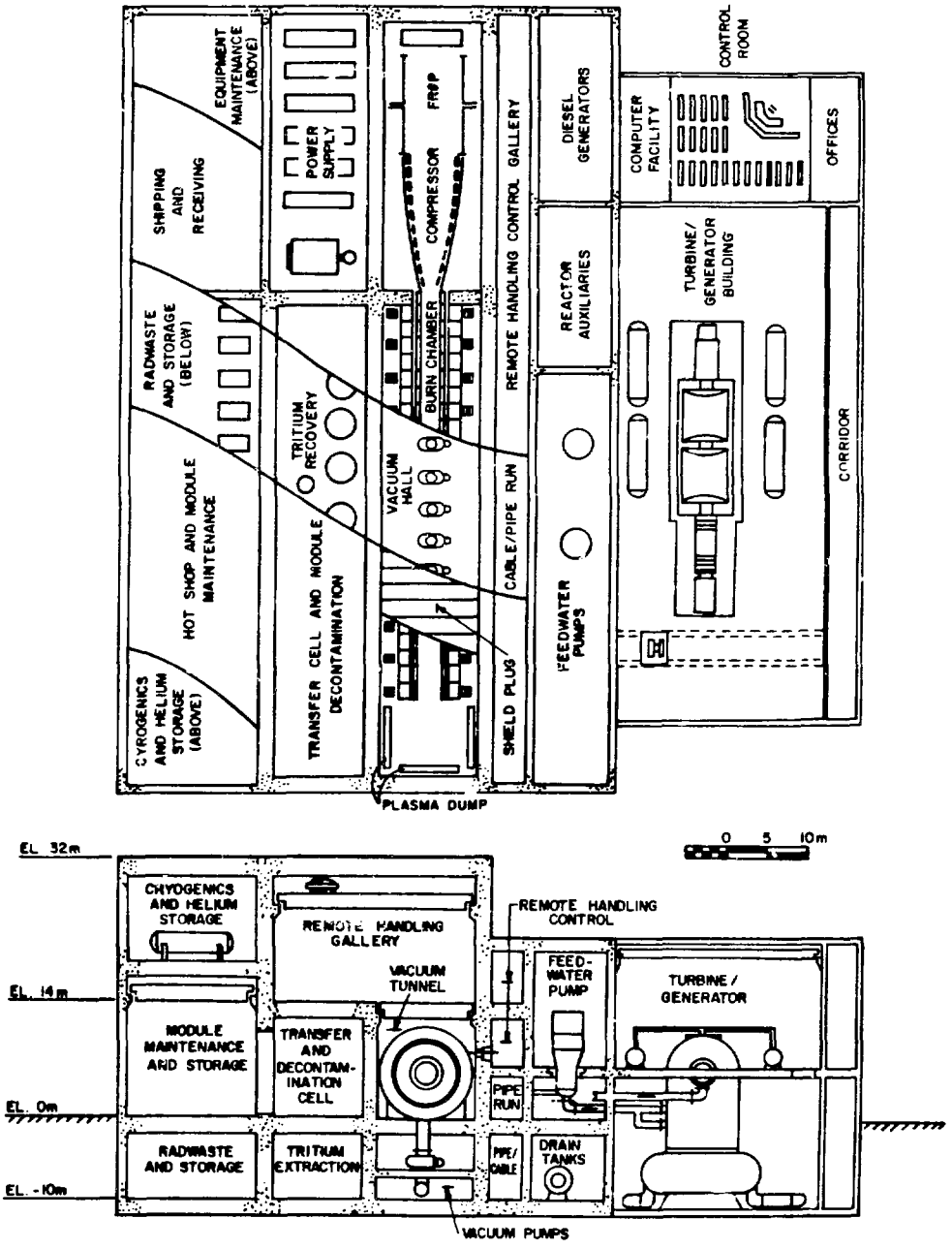

Fig. II-4. Preliminary plant layout for the CTOR.

section, while the elements of the first wall and blanket are made progressively larger (in a step-wise fashion) along the axial length to provide the modest taper required for alpha-particle-driven plasmoid expansion and translation.

Maintenance equipment for this system is also indicated in Fig. II-4. The entire CTOR is located inside a vacuum tunnel which allows relatively easy access to the vacuum seals (shield plugs). Upon removal of three adjacent 2-m-long shield plugs, two solenoidal magnet coils are uncovered. The top-hemicylindrical half of the water shield would be removed between the fixed superconducting coils. Simple translating motions then allow the other two shield sections (located under the magnet coils) to be removed, uncovering three 2-m long first-wall/blanket modules. These modules are transferred to the adjacent decontamination cell and ultimately are moved into the hot cell facility. It is emphasized that the level-of-effort devoted to this Level II study has not allowed a detailed or self-consistent CTOR plant design to be made. Consequently, the engineering approach suggested above represents a direct extrapolation from other studies.[22,23] Similarly, the reactor engineering approach that has emerged from more detailed studies of tokamaks, the ELMO Bumpy Torus or the Tandem-Mirror Reactor could just as well be applied to the CTOR. In fact, the application of first-wall/blanket/shield, magnet, reactor layout and vacuum, BOP and general maintenance schemes emerging from more detailed designs associated with STARFIRE, EBTR or TMR to the CTOR would in all likelihood be more straightforward, in that CTOR does not require impurity control, active fuelling, plasma heating (in the burn chamber), etc..

D. Conclusions

Generally, the CTOR is represented as a high-Q system (Q_E = 6.8) of modest size (310 MWe). The pulsed energy storage requirements are only ~ 60 MJ of capacitive energy for the FROP, a 175-MJ homopolar generator and 25, 7-MJ homopolar machines distributed along the traveling-wave network. Direct energy recovery is achieved in the quench region without the use of opening switches, with the plasma motion inherently providing the necessary switching characteristics. Furthermore, this high-Q performance is not sensitive to the direct-energy recovery aspects of the overall reactor operation. The high-voltage and active plasmoid source elements can be completely disassociated from the passive burn section. The linear system with an open magnet configuration simplifies maintenance and construction procedures. A natural divertor is also presented by the open-field line geometry outside the separatrix.

The realization of this attractive system is contingent upon the transport properties assumed for the plasma. Systems with high losses ($\tau_E \sim 0.1$ s for the design plant) will either require higher operating densities (leading to a more serious first-wall thermal cycle) or to systems of larger radial dimensions (increased FRC source requirements). Since the size of the source requirements increase as $\sim nr_w^3$, larger pulsed power requirements are imposed. Particle transport may also have adverse effects on the burn cycle. The batch burn system used here is based on little change occurring in the particle inventory, during the ~ 2 s burn. Particle loss is likely to occur along with injestion of gas streaming to the plasmoid from the quench region. The competition of these two process will determine the time-dependent particle inventory, a process that requires more detailed modeling.

The reactor study presented herein in conjunction with other CT design efforts (Sec. I. and Sec. III.) has led[4] to several general conclusions that are summarized in Table II-IV.

TABLE II-IV

GENERAL CONCLUSIONS FOR THE COMPACT TOROID REACTOR

- Steady-state, in situ plasma startup CT reactor does not exist. A mechanism other than active feedback is needed to stabilize such a steady-state device.
- MRFRMR/CTOR/IRC are moving independently toward similar reactor embodiments using pulsed-plasmoids translating in a linear burn chamber.
  - Fractional GW(e) systems
  - High-Q, low recirculating power systems
  - Relatively low pulsed power requirements
  - Segregation of systems needed to perform key functions (startup, burn, exhaust etc.)
- Potential for attractive CT reactors exist. Small reactor plasmas appear achievable without extravagant extrapolation of technology.
- Level of CT reactor studies is not sufficient to make quantitative economic intercomparisons with other more developed systems.

- Physic basis is not adequate to make a clear-cut choice between concepts, and economic analysis should be used ultimately to examine tradeoffs within a given system.

- Present knowledge allows a pulsed-plasmoid CT reactor that reflects to some degree a system of lower reliability, higher design constraints and potentially higher cost. In these systems only the plasmoid, the plasmoid source and the first-wall are pulsed with all major engineering systems operating in a steady state.

  - A search for a truly steady-state CT reactor should continue

  - The actual cost of pulsed operation should be quantified; steady-state operation requires new physics, new plasma engineering systems and added costs

- CT reactor studies are beginning to provide some feedback to experimental and theory efforts, and this useful symbiosis should continue. Reactor physics models should strive for more uniformity of assumption and level of detail resulting from enhanced communication between physicists and reactor designers.

The theoretical and experimental effort needed to resolve these issues is at a relatively low level, although substantial progress has been made during the last few years. This enhanced level of understanding has been reflected by the reactor studies, as a general convergence has occurred in the design of translating plasmoid systems. Stationary pulsed-plasmoid systems are also being pursued using the same theoretical base as the translating-plasmoid reactors. Finally, consistent operating scenarios for steady-state plasmoid CT reactors have not been developed, however, design effort for such devices should continue.

III. PREVIOUS CT REACTOR DESIGNS

A number of conceptual reactor designs based upon reversed-field configurations (FRC's) have been documented, although few detailed reactor designs exists. The first considerations of using a reversed-field plasmoid to produce power were based upon the ASTRON[18] concept shown schematically in Fig. III-1. Electrons accelerated to relativistic energies (20-50 MeV) are injected at the end of a cylindrical vacuum chamber. The electrons gyrate poloidally about the central axis while traveling back and forth between the mirrors; an electron layer is thereby generated. The current carried by this e-layer reverses the externally applied magentic field and produces closed field lines that are potentially capable of confining a thermonuclear plasma.

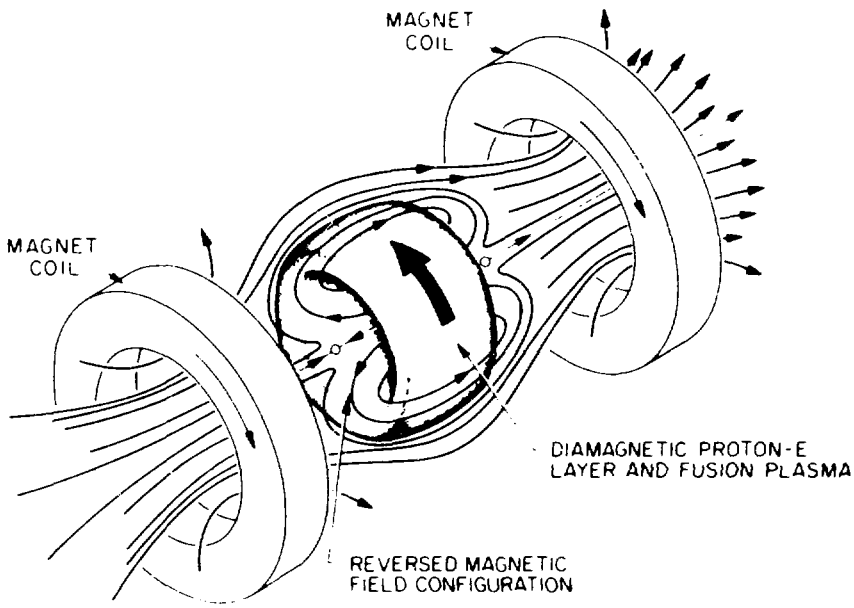

Fig. III-1. The original ASTRON[18] concept.

Particle interactions between the e-layer and deuterium/tritium atoms would produce the thermonuclear plasma immediately after formation of the closed field lines. More detailed analysis of this concept revealed, however, that the slowing-down time of fast electrons, because of synchrotron radiation, would be shorter than that required for an energy breakeven, unless the electron energy was less than 20-50 MeV. This constraint limits the plasma and fusion-power density to values that would be too low for economic power production.

To avoid the synchrotron radiation problem, the injection of high-energy ions rather than electrons was proposed.[19] Electron-ring energies near 300 MeV were found to give optimal confinement properties. Producing and sustaining these electron rings solely by particle accelerators was deemed unfeasible[20] because of the difficulties in making an acceptable energy balance. Assuming instead a steady-state ion ring, the overall power gain, Q, is defined as $\varepsilon_a \varepsilon_t \eta (E_p/E_r)(n\tau_r/n\tau_p)$, where ε_a, ε_t and η are accelerator, beam-trapping and thermal-conversion efficiencies, respectively. Taking the ratio of plasma thermal energy to the ion-ring energy as $E_p/E_r \sim 1\text{-}2$ and the corresponding

ratio of $n\tau_r/n\tau_p \sim 10\text{-}15$ for the same two species gives $Q \sim (10\text{-}30)\varepsilon_a\varepsilon_t\eta$. If the overall efficiency of energy deposition in the plasma versus electrical input to the accelerators is $\varepsilon_a\varepsilon_t \sim 0.07$ and if $\eta \approx 0.4$, the system would not achieve an energy breakeven. In order to compensate for the poor energy balance a much more efficient ring heating source would be required; an adiabatic ion-ring compression cycle was then proposed.[20]

Producing the ion-ring at somewhat lower energies (~ 30 MeV) by particle beams, the inefficiencies become less significant, since the bulk of the plasma energy is added to the ring by a highly-efficient adiabatic compression. A schematic diagram of this device is shown in Fig. III-2, and a summary of expected reactor parameters is listed in Table III-I.

In both the ASTRON and ion-ring devices, the azimuthal current is carried predominantly by the high-energy particles. As the pressure of the background particles is increased, a significant fraction of this field-reversing current is provided by plasma diamagnetic currents. The field-reversed mirror (FRM)

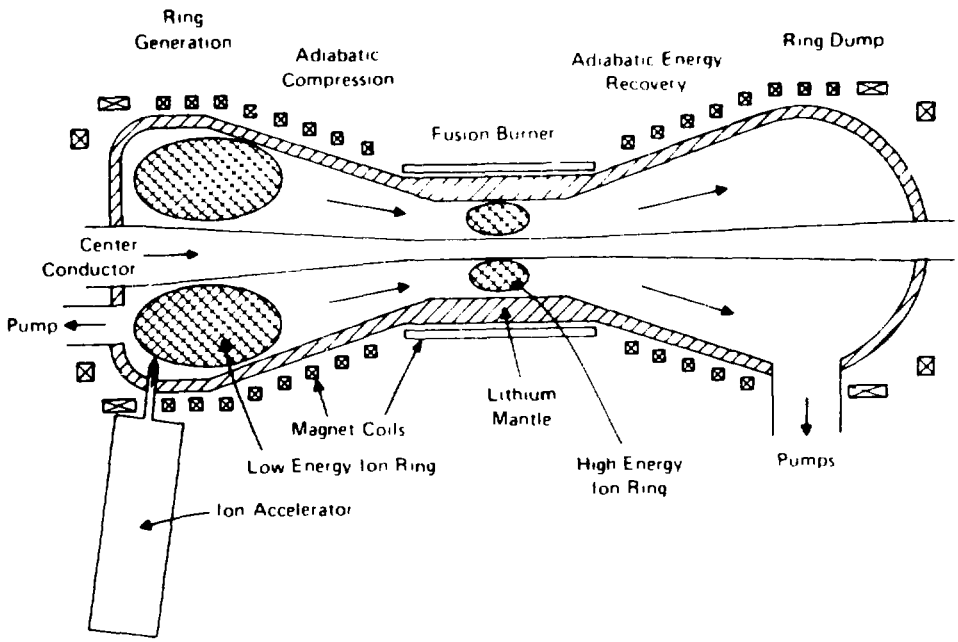

Fig. III-2. The ion-ring compressor reactor concept.[20]

TABLE III-I

ESTIMATED PARAMETERS FOR ION-RING COMPRESSOR REACTOR[20]

PARAMETER	BURN CHAMBER	COMPRESSION CHAMBER
Deuteron energy (MeV)	300	30
Total fast-ion charge (C)	1.5	1.5
Major ring radius (m)	3	10
Radial ring thickness (m)	3	10
Axial ring length (m)	4.5	15
Plasma temperature (keV)	20	low
Plasma density ($10^{20}/m^3$)	0.63	0.1
Fusion power per ring (MW)	300	0
Total energy per ring (MJ)	540	50
Ring lifetime (s)	5	0.1
External axial magnetic field (T)	1.4	0.14
Magnetic field at ring radius (T)	0.67	0.20
Axial current (MA)	10	10
First-wall radius (m)	4.5	15
First-wall loading (MW/m^2)	2.3	0.1
Compression time (s)	--	0.2-0.5
Duty cycle	0.8-0.9	--
Ring energy gain, Q	3	--

relies solely on these plasma currents to provide field reversal without the use of a high-energy, circulating layer of particles. The difference between the ASTRON and FRM geometries can be described in terms of a parameter $S = a/\rho_i$, which is a measure of the number of ion-gyroradii, ρ_i, enclosed by the plasma radius, a. A class of particles with $S \lesssim 1$ exists in an ASTRON device, while the FRM configuration would operate with $S \sim 5$-10. In the absence of a conducting shell, finite-Lamor-radius (FLR) stabilization is considered crucial to the FRM stability, and an upper limit on a/ρ_i is generally taken[5-10] to be ~ 10. In either case, Ioffe bars are required to provide a radial magnetic well for plasma stability. The FRM has been investigated[5-7] as a possible means to increase the energy gain for a simple mirror fusion reactor. A sample field line configuration with $R/a \sim 2$ and $\ell/a \sim 14$, based on results from the particle code SUPERLAYER,[5] is used as the

FRM reactor model. All plasma quantities are integrated over an assumed isothermal plasma using a cubic density profile; a coupled set of time-dependent zero-dimensional equations results. Including neutral-beam interactions, alpha-particle burnup, radiation losses (Bremsstrahlung and cyclotron), ion-electron equilibration, diffusion and thermal conduction, steady-state solutions to these reactor equations are determined. The particle loss rate was taken as $\tau_p \simeq A_p a^2 \tau_{ii}/\rho_i^2$, where A_p represents a profile-related constant of order of unity, and τ_{ii} is the ion collision time. This *ad hoc* scaling is proportional to the ion-ion collision time, which is taken to represent a conservative or "worst-case" limit for the particle confinement. The ion heat conduction is taken to be small while the electron conduction is assumed to characterize the major plasma energy loss and is expressed as $\tau_E = 0.2\ a^2 \tau_{ei}/\rho_e^2$, where the constant, 0.2, is inferred from tokamak experiments and the electron-ion collision time is used.

Fixing S at 5 and assuming 10% of the alpha-particle energy is deposited in the plasma, curves of Q *versus* neutral-beam energy are generated for an assumed steady state. A maximum Q is achieved for a neutral-beam energy of 200 keV; a summary of plasma parameters for the FRM are listed in Table III-II. The calculated plasma parameters are used as input to a

TABLE III-II

PLASMA PARAMETERS AT OPTIMAL Q FOR THE FRM REFERENCE REACTOR[5]

PARAMETER	VALUE
Plasma minor radius, a(m)	0.07
Aspect ratio, R/a	2
Length-to-radius ratio, ℓ/a	14
$S = a/\rho_i$	5
Plasma beta, value β	1.5
Plasma centerline density, $n_o(10^{20}/m^3)$	6.5
Electron temperature (keV)	32
Plasma temperature (keV)	96
Vacuum field (T)	4.1
Fusion power (MW/cell)	20
Fusion power/injected power	5.5

computer code which determines required reactor sizes and component costs. A minimum unit reactor cost ($/kWe) is achieved for the plasma parameters given in Table III-II; a summary of the FRM reactor design is given in Table III-III.

Like the CTOR design presented here, no detailed reactor design of the FRM reactor has been made, although estimates of system maintenance and overall plant design are available.[5] The helium-cooled FRM reactor proposes solid, lithium-containing compounds for tritium breeding. Cylindrical components are used to construct the first wall, blanket, shield and

TABLE III-III

REFERENCE FRM REACTOR DESIGN PARAMETERS[5]

PARAMETER	VALUE
First-wall radius (m)	0.73
Cell length, ℓ(m)	2.0
Number of cells	11
Superconducting field (T)	4.1
Axial magnetic well on axis (mirror coils)	1.0013
Radial magnetic well at plasma edge (Ioffe bars)	1.0001
Injected power to plasma (MWt)	40
Fusion power[(a)] (MWt)	220
Gross electric power [(b)] (MWe)	136
Power to 200-keV neutral-beam injectors (MWe)	54
Power recirculated to copper coils (MWe)	8
Net electric power (MWe)	74
Recirculated power fraction, ε	0.46
System efficiency, $\eta_p = \eta_{TH}(1-\varepsilon)$[(b)]	0.29(η_{TH} = 0.4)
Direct capital cost ($/kWe)	1210

[(a)]Losing 16 MWt of the fusion neutron power in the room-temperature copper coils positioned inside the first wall and taking a blanket multiplication of 1.2 results in a total blanket power of 192 MWt.

[(b)]The 84 MWt injected plus 20% of fusion power of charged particles pass through a 50% efficient single-stage direct-energy convertor. The remaining thermal energy, along with the blanket energy, is converted to electricity with a thermal efficiency of 0.4. This improves the system efficiency from 0.22 to 0.29.

superconducting coils. Advantages of linearity and axial modularity are emphasized, with each 2.04-m long cell weighing ~ 550 tonne and being removable from the system as a single unit. The original FRM reactor design[6] is shown schematically in Fig. III-3 as a vertically-oriented device. Because of maintenance problems, the FRM reactor is presently being proposed in a horizontal orientation, with a vacuum shell surrounding the coil structure. Plan and elevation views of this system are given in Ref. 5.

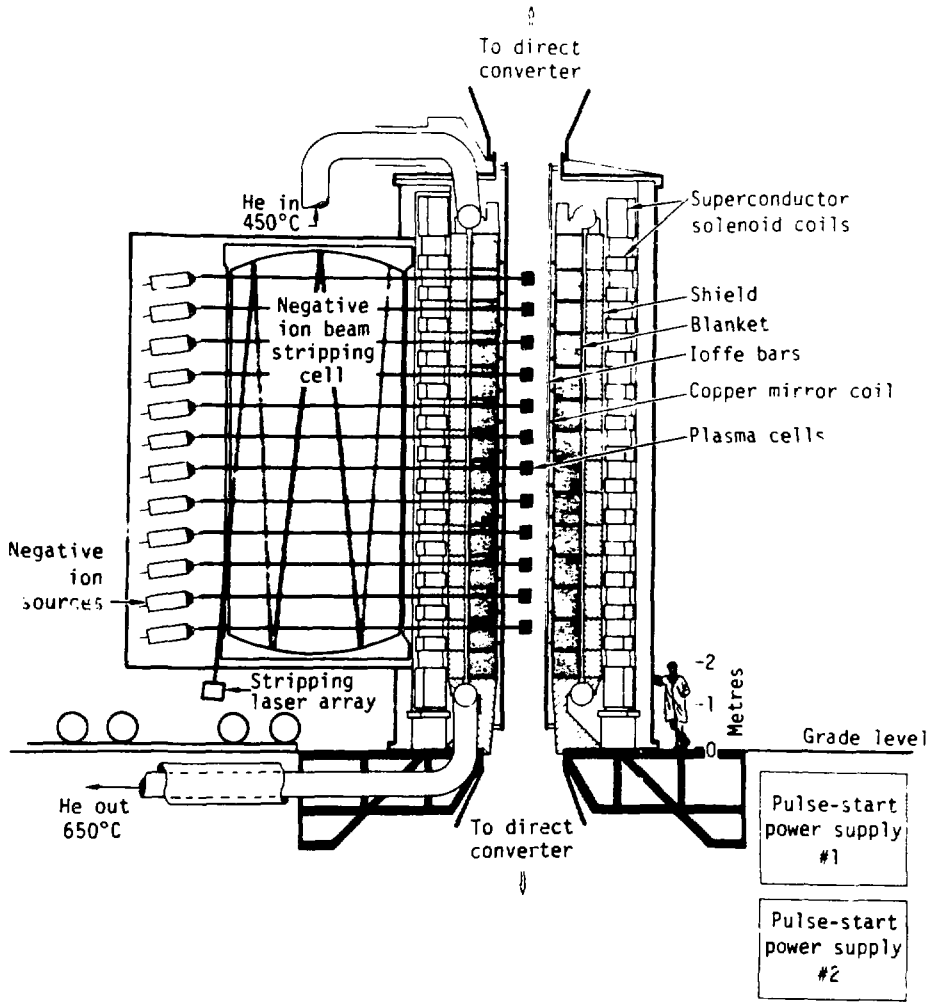

Fig. III-3. Layout of multicell field-reversed mirror reactor.[6]

Major engineering concerns focus on the severe technology problems associated with electrical insulators and lifetime of the mirror coils, which are located immediately inside the first wall; the Ioffe bars, which are also positioned near the first wall also represent serious design concerns. The development of negative-ion-beam neutral-particle injectors (200 keV) needed to sustain the steady-state FRM would require a major effort. Startup of the FRM presents an uncertainty that is only qualitatively discussed.[5] Slow buildup of this FRC by neutral-atom beams, intense pulsed ion-neutral-atom sources, reversed-field theta-pinch, rotating electron or ion-beam, conical theta-pinch guns, coaxial guns and remote magnetic compression of field-reversed plasma rings are methods that have been considered for startup. Coupling of the initial or starting plasma to the assumed steady-state reactor burn has not been investigated computationally. Noting that $\tau_{ii} \sim T_i^{3/2}$ and $\tau_{ei} \sim T_e^{3/2}$, it follows that $\tau_p \sim a^2\tau_{ii}/\rho_i^2 \sim T_i^{1/2}$; similarily $\tau_{Ee} \sim T_e^{1/2}$. These approximate scalings imply substantially higher powers may be requigld for startup (i.e., lower temperatures) than is needed for sustenance of the burn. The maintenance of stability and equilibrium throughout this startup phase represents an additional uncertainty requiring further quantitative study.

Conceptual design studies for a FRM pilot plant have also been performed.[7] This system has as a primary objective net power production using near-term technology. Only one FRM cell is used to produce 22 MW of fusion power and requires 4.4 MW of neutral-atom beam injection power. Parametrically increasing $S = a/\rho_i$ from 5 to 7 increases the fusion power from 22 to 42 MW with 3.2 MW of injected power being required. The sensitivity of reactor performance to the efficiency of alpha-particle heating vis a vis the assumed value of S is very strong. The target plasmoid is assumed to be formed by a coaxial plasma gun and is subsequently heated, fueled and sustained by 200-keV (negative ion) neutral beam injectors with an assumed efficiency of 50%. A pair of superconducting coils provide the solenoidal field and small axial well, while the radial magnetic well is provided by four superconducting saddle coils. With S = 5, 90% of the 11.6-MWe gross electrical power must be recirculated, yielding a net power of 1.2-MWe. For the case where S = 7, 46% of the 19.8-MWe gross power is recirculated, giving a net power of 10.7 MWe. The technology, lifetime and economics problems associated with locating magnet coils near the first wall have been avoided in

this latest design;[7] superconducting coils are positioned outside the blanket and shield. The unknown issues associated with plasma startup, equilibrium, stability and neutral-beam construction and utilization, however, remain to be resolved.

The Moving-Ring Field-Reversed Mirror Reactor (MRFRMR)[7-10] exhibits many similarities to the FRM reactor; the same plasma physics model is used. The major difference between the two concepts rests with the means by which a plasmoid is utilized in the burn chamber. The FRM reactor uses high-energy neutral beams for refueling and sustaining a confined plasma ring in a fixed (stationary) magnetic well. The MRFRM reactor, on the other hand, proposes magnetically compressing the plasmoids to the initial burn temperature and transporting these ignited FRC's down the burner section of the reactor by means of mirror coils; this scheme is illustrated in Fig. III-4. The external

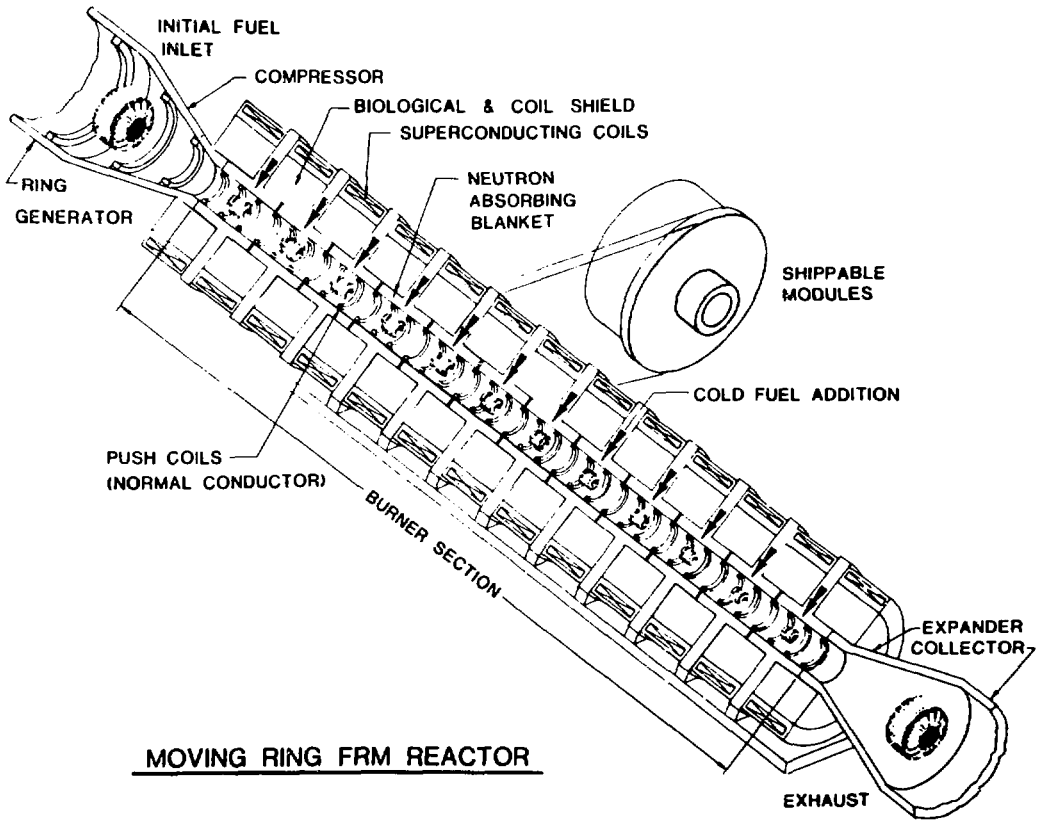

Fig. III-4. Moving-Ring FRM Reactor.[8]

energy added to the FRC during this translation is small, although relatively cold plasma may be used to refuel the plasmoid during its transit. In the preliminary design[8] the plasmoids are not ignited, and thermal quenching of the burn because of the cold-plasma refueling determines the FRC lifetime; the magnetic diffusion time (tens of seconds) is considerably longer than the plasma burn time (~ 0.3 s). An electrically conducting first wall provides wall stabilization, centers the moving plasmoid within the burn section and eliminates the need for multipole fields (i.e., first-wall Ioffe bars) to provide radial stabilization.

The basic physics assumptions invoked by the MRFRMR design are similar to those used for the FRM reactor. A multi-species, non-thermal relativistic Fokker-Planck code calculates the time dependence of an isothermal plasma on the basis of an assumed cubic radial density profile. The particle confinement time is required to be three times longer than that assumed for the FRM approach in order to achieve the same overall plasma Q-value. Electron and ion heat conduction are neglected because of the assumed rapid particle loss along the open field lines outside the separatrix. The fraction of alpha particles retained by the plasma is again assumed to be 0.1. A summary of key plasma parameters for the reference MRFRMR is given in Table III-IV. Systems with and without cold fuel addition were investigated, with the fueled plasmoid case serving as a reference case. Adding fuel causes a significant decrease in plasma temperature from 75 keV to ~ 8 keV at the end of the burn, although the power is maintained at a nearly constant 10.6 MWt because of the doubling of the time-average ion density during the 0.32-s burn. Without fuel addition a nearly constant ion temperature is maintained, although the fusion power varies from 10.6 to 4 MWt during the same burn period. Plasma refueling by pellet injection is assumed; a CO_2 laser is used to heat and to propel the refuelling pellet with a pulse energy of a few hundred joules, pulse width ~ 0.5 μs, repetition rate of 10 Hz and spot of focus 0.5-mm diameter over a distance of 30 mm. For an input laser power of 15 kWe, pellet velocites of ~ 10^5 m/s could be achieved.

Plasma startup is qualitatively addressed by the MRFRMR design study. Using one of the plasma initiation techniques discussed for the FRM reactor, the plasmoids would be subsequently compressed to the initial burn temperatures, as illustrated by Fig. III-4. Specific parameters are not given, although a substantial final ion temperature (~ 75 keV) would be

TABLE III-IV

KEY PLASMA PARAMETERS FOR THE MOVING RING FRM REACTOR (MRFRMR)[8-9]

PARAMETER	VALUE
Initial plasma major radius (m)	0.096
Final plasma major radius (m)	0.066
Plasmoid aspect ratio	2
Ratio of length to minor radius	6
Initial value of $S = a/\rho_i$	5
Peak plasma beta, β	1.5
Initial ion temperature (keV)	37.5
Initial ion density ($10^{20}/m^3$)	4.8
Initial electron temperature (keV)	37
Initial electron density ($10^{20}/m^3$)	9.6
Vacuum field (T)	6.5
Burn time (s)	0.32
Fueling injection energies for D/T/e (keV)	3.3/4.9/0.9
Average particle injection rate per species (10^{20}/s)	0.2
Energies per plasmoid (MJ)	
• Fusion energy	3.38
• Initial plasma energy	0.41
• Refueling energy	0.008
• Expansion/compression work on plasma	0.181

required. Using analytical equilibrium results given in Appendix B for a separatrix radius, r_s, equal to the conducting shell radius, r_c, the quantity $Tr_s^{8/5}$ is a constant. A linear radial compression of ~ 15 would then be required if the starting plasma is ~ 1 keV. These conditions correspond to a starting plasma radius of ~ 1.5 m before compression.

Having achieved the desired temperature, the plasmoid would be driven through the device by a set of active mirror coils that are positioned internally to the first wall. The electrical and mechanical integrity of these coils, which would be subjected to an intense heat flux and radiation environment, is not addressed in detail. A 20-mm thick aluminum conducting shell in conjunction with the mirror coils provides necessary stabilization

against the precessional mode. The residence time of the MRFRMR plasmoid does not exceed 20% of the classical L/R decay time for currents induced in an infinitely long conducting shell. For a 20-mm-thick shell this residence time is ~ 0.015 s, and the plasmoid speed is taken as $2(0.29\ \text{m})/0.015\ \text{s} \sim 40$ m/s, where twice the maximum axial length is used. At this speed the resistive drag on the plasmoid at the beginning of the burn amounts to ~ 3 kJ/m, while the smaller end-of-burn configuration presents a resistive loss of only ~ 0.3 kJ/m. The drag equations derived in Appendix E substantially overestimate the resistive drag loss if applied to the MRFRMR design. These equations require $\ell/r_c \gg 1$ (axial uniformity), whereas for the MRFRMR $\ell/r_c \lesssim 1$. Using the aforementioned plasmoid speed and taking the burn time of 0.32 s, the length of the reactor would be 12.5 m. Establishing a magnetic well that is stable against the precessional mode leads to the reactor

TABLE III-V

MOVING-RING FIELD-REVERSED MIRROR REACTOR PARAMETERS[8,9]

PARAMETER	VALUE
First-wall radius (m)	0.325
First-wall conducting shell thickness[(a)] (m)	0.02
Cell length (m)	1.05
Mirror coil centerline radius[(b)] (m)	0.255
Mirror coils axial spacing (m)	0.35
Mirror coil dimension (mm x mm)	40 x 40
Plasmoid speed (m/s)	40
Reactor burn section length (m)	12.5
$Li_7\ Pb_2$ breeding blanket thickness (m)	0.4
Stainless steel/B_4C shield thickness (m)	0.97
First-wall average neutron loading[(c)] (MW/m^2)	3.85
First-wall peak neutron loading (MW/m^2)	6.2
Gross electric power (MWe)	7.4-8.2
Net electric power (MWe)	1.25-4.75

[(a)] Aluminum shell operating at reactor blanket temperatures.
[(b)] Water-cooled copper coil.
[(c)] Assumes one plasmoid per cell length at any given time.

parameters listed in Table III-V. The helium-cooled blanket is constructed of annular cylindrical components containing solid lithium compounds for tritium breeding. Several blanket configurations were explored, including low-activation systems. A range of electrical outputs are given, since a detailed energy balance has yet to be completed.

The high recirculating powers computed for the earlier MRFRMR design[8] have led to investigations of alternative burn cycles that could result in higher plasma Q-values. The most sensitive plasma parameters appear to be $S = a/\rho_i$ and the fraction of alpha-particle power retained in the plasma. Increasing S from 5 to 10-15 allows the plasma to ignite, resulting in substantially higher Q-values. Increasing S also dramatically increases the fraction of alpha-particle energy retained in the plasma. These results have been incorporated into the MRFRM plasma model and a commercial prototype reactor design study based on the use of ignited plasmoids is presently in progress.[9,10]

The sensitivity of the reactor design on $S = a/\rho_i$ has led theta-pinch experiments[25] to investigate the particle/energy transport as a function of this parameter. In contrast to past assumptions that an upper bound of ~ 3-5 may exist for S, the maximum stable times are found at the highest values of S (~ 10) achievable by the device. Experimentally stable times ($\gtrsim$ 50 μs) are ~ 100 times greater than characteristic MHD e-folding times. This experimental finding implies that values of S in excess of 10 may be realistic and are, therefore adopted by the CTOR designs proposed herein.

Two reactor concepts[16,26] have also been proposed based directly on the FRΘP system. A multiple-cell device[26] has been proposed to "end stopper" a linear theta pinch. A multiple-mirror geometry would be stabilized by internal plasma cells consisting of reversed-field configurations. Using a long FRΘP, multiple cells are produced by weak mirror coils that in turn induce resistive tearing modes within the plasma column. The FRΘP multiple mirror appears to offer advantages over a simple multiple-mirror device because the effective ion mean-free-path is reduced from a collison mean-free-path (5-10 m) to the intercell distance (0.05-0.1 m). Also, a significant fraction of the fusion yield would arise from plasma trapped on open field lines. A reactor length of ~ 20 m is projected[26] for a plasma with a ~ 20-mm radius, requiring a 10-T magnetic field to achieve a Lawson parameter of $\sim 10^{21}$ s/m^3 at T = 8 keV with a total plasma energy of 18 MJ for this high-

beta ($\beta \simeq 1$) system. The reduced size is significant when compared to lengths in excess of 10 km projected for conventional linear theta pinches.[27]

The Triggered Reconnection Adiabatically Compressed Torus (TRACT) reactor concept[16,17] is based on the use of a single FRCP cell. A superconducting bias field maintains a 7-T field during the 0.5-s plasma burn. During the startup a normal coil is positioned near the first wall and is used to cancel the superconducting field to establish a reverse-bias field inside the plasma chamber. A rapid decrease in the normal coil current causes a radial shock to be driven in the plasma; and reverses the magnetic field while a cusp field at each end delays field-line reconnection until the vertical flux peaks. Reversal of the cusp current subsequently triggers the field-line reconnection, resulting in a rapid axial compression and strong plasma heating. As the current in the first-wall normal coil is reduced to zero, the plasma is adiabatically compressed by the raising superconducting magnet field. The reactor parameters for TRACT are summarized on Table III-VI. This reactor design and plasma burn on a per unit length basis are similar to the Reference Theta-Pinch Reactor (RTPR) concept,[28] with the toroidal configuration being replaced by a compact torus of much smaller axial length in a cylindrical reactor. Both the multiple-mirror[26] and TRACT[17] concepts initiate and burn the plasma in the same chamber. The potential engineering difficulties of handling high-voltages in a radiation environment are introduced; the required voltage, however, may be reduced compared to the RTPR design[28] as a result of additional heating caused by the axial shock. These pulsed reactor systems must also address first-wall thermal fatigue problems in conjunction with voltage requirements.

Lastly, the LINUS[14,15] reactor concept proposes the compression of an FRC plasmoid by a rotating liquid-metal (Li or LiPb) liner. This system has advantages of compactness and high power density, while possessing a renewable first wall that also functions as a neutron moderating and tritium breeding medium. A helium reservoir is used to drive the lithium liner and to compress the plasma to ignition. This concept is significantly different from those investigated in this report and is, therefore, not explored here in detail. Table III-VII gives key reactor parameters that have emerged from two independent LINUS studies.[14,15]

TABLE III-VI

TRACT REACTOR PARAMETERS[16]

PARAMETER	VALUE
Length (m)	5.0
First-wall radius (m)	0.5
Magnetic field (T)	7.0
Plasma temperature (keV)	15
Plasma average density ($10^{20}/m^3$)	20
Plasma separ atrix radius (m)	0.34
Plasma length (m)	2.12
Assumed confinement time (s)	0.5
Shock heating energy (MJ)	8
Adiabatic compression energy (MJ)	80
Electric field at first wall (kV/m)	$\lesssim$ 50
Peak thermal power (MWt)	367
Burn time (s)	0.5
Repetition rate (1/s)	1
Peak first-wall neutron loading (MWt/m^2)	15
Recirculating power fraction[(a)]	0.11
Net electric power[(a)] (MWe)	90

[(a)] A total output energy of 278 MJ/pulse would be converted with an efficiency of 0.36 to electricity; 1.9 MJ/pulse is recirculated for Joule heating, 4.2 MJ for switching losses, 4.5 MJ for plasma preparation and 1 MJ for coolant pumping losses.

IV. REACTOR DESIGN BASIS

A. CTOR Operating Scenario

This conceptual design of the compact toroid reactor (CTOR) has been driven by a goal to produce the simplest possible engineering system in order to minimize maintenance and operational problems, and to emphasize increased system reliability. In addition, the use of near-term technology wherever possible is emphasized throughout this design effort. This approach provides the most accurate assessment of system desirability and allows the most rapid experimental advancement toward the reactor system. The minimization or elimination of certain long-term developmental items, usually required in

TABLE III-VII

LINUS REACTOR PARAMETERS[14,15]

PARAMETER	VALUE[a]
Minor radius (m)	0.08/0.037
Major radius (m)	0.19/0.11
Length (m)	3.1/10.0
Plasma volume (m^3)	0.35/0.50
Density ($10^{20}/m^3$)	2400/1900
Temperature (keV)	15/20
Averaged beta	0.55/0.60
Plasma power density (MW/m^3)	4000/6500
Ignited/Driven burn	DRVN/IGN
Magnetic field (T)	54/60
Pulsed Energy (MJ)	NA
Burn time (s)	0.0004/0.0010
Off time (s)	1.0/0.5
Neutron current (MW/m^2)	305/259
Heat Flux (MW/m^2)	4.7/7.0
Thermal Power (MWt)	1790/3350
Net power (MWe)	507/910
System power density (MWt/m^3)	4.1[b]/4.1
Recirculating power fraction	0.15/0.22
Net plant efficiency	0.28/0.27

[a] NRL/LASL parameters

[b] Calculated using reactor volume including the gas reservoir used to drive the liner.

fusion systems, greatly enhances the desirability of the compact-toroid reactor. This design rationale is believed to represent an inherently economically attractive system in which long-term development is minimized. Small reactor systems allow proof-of-principle without large economic investment and conventionally engineered systems are most likely to result in minimized power costs. An economic evaluation of CTOR is not performed, however, at this early stage of development and many of the above claims remain to be substantiated or disproved by future study.

The desired design objectives and consequential impact on the CTOR design are listed in Table IV-I; a reactor schematic is shown in Fig. IV-1. The primary experimental evidence for elongated compact-toroid plasmas has come from the Field-Reversed Theta Pinch (FROP). This plasmoid source is considered to be scaleable to larger sizes when using a Marshall coil as described in Sec. VII.B.1 and Appendix F. These considerations have led to the adoption of this source for the CTOR reactor design. This choice may not be an optimal plasma source, however, and startup devices that require slower

TABLE IV-I

SUMMARY OF CTOR DESIGN RATIONALE

OBJECTIVE	DESIGN-CONSEQUENCE
Use near state-of-the-art technology.	Plasma source taken to be field-reversed theta pinch (FROP). The ~ 1 keV plasma is adiabatically heated to ignition.
Removal of high-voltage regions from burn section.	Translation of plasma from source to burn section.
Minimize source and pulsed power requirements.	Tapered axial compressor section maintains the wall and magnet coil close to the plasma surface.
Continuous presence of conducting shell along with a nearly steady-state operation (thermally) of the reactor burn section and minimization of first-wall thermal cycle.	Translating plasma in burn section allows "new" portions of conducting shell to be continually uncovered.
Minimize complexity of system required for translation and avoid recirculation of electrical losses in conducting shell.	Passive translation provided by flaring conducting shell with expansion (translational) power provided by alpha particles.
Minimize plasmoid dimensional changes required for providing translational power.	Place room-temperature conducting shell outside blanket.
Prevent translational runaway	First wall "shell" is highly permeable to flux penetration, although stabilizes translation.
Maximum conversion of internal plasma energy to electrical energy by direct-conversion work.	Translate, stop and expand in end region. Translation provides the necessary switching.

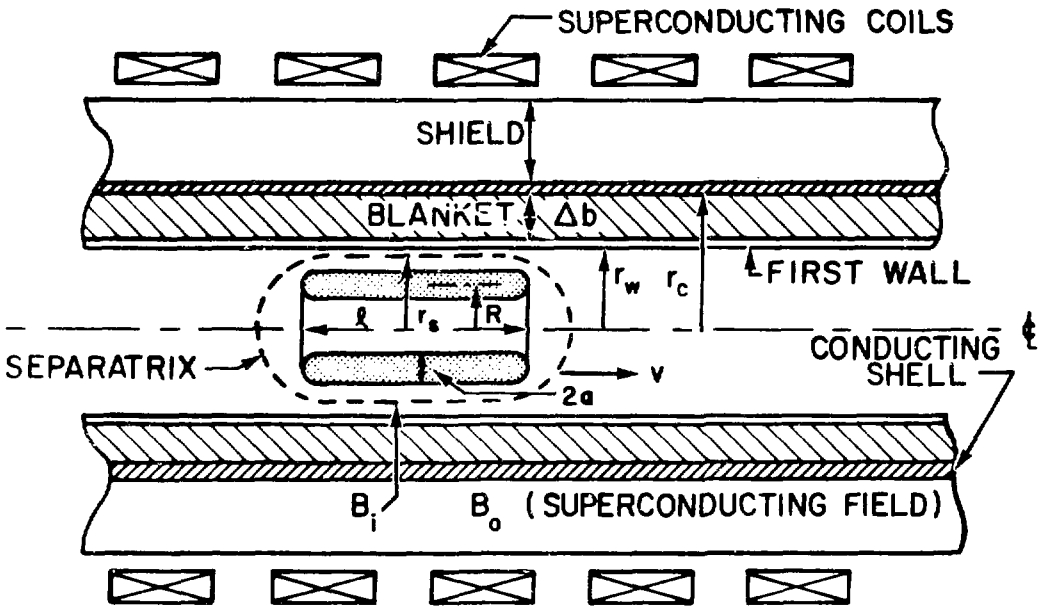

Fig. IV-1. Schematic view of the Compact Toroid Reactor (CTOR) based on a translating Field-Reversed Theta Pinch.

timescales, such as a coaxial theta pinch, may produce the plasmoid on a slower timescale, thereby relaxing certain engineering constraints associated with a FROP (see Sec. VII.B.1).

Separation of the plasma source from the reactor burn region is considered highly desirable to avoid high-neutron and thermal fluxes in the high-voltage source region. This separation of the high technology subsystems from the reactor environment is easily achieved by the CTOR because of the compact nature of the plasmoid. During initiation of the plasmoid a small translational velocity is given to the plasmoid by the FROP source, drifting the plasma into a compressor section. Beginning with a hot plasma ($T \sim 1$ keV) with relatively good confinement properties, allows compression to ignition by the capacitive energy stored in a rotating machine having a risetime of $\tau_R \sim 0.1$ s. Minimizing the size of this source requires the compression chamber to be tapered, maintaining a constant ratio, r_c/r_s of stabilizing-shell to separatrix radius. This operational mode is also desirable on the basis of stability considerations, where $r_c/r_s \lesssim 2$. The compressor section is

constructed from an appropriately-coupled (Sec. VII.B.2.) set of magnet coils which produce a traveling-wave electrical pulse. The resultant magnetic wave translates the plasmoid while providing three-dimensional compression without requiring complex multi-switch, multi-element electrical networks. Compressional work is performed on the plasma, and increases in temperature are modeled by equilibrium calculations given in Appendix D.

Emerging from the compression section at ignition (T ~ 4-5 keV), the FRC is translated through a linear burn section. A large translational drag force is exerted on the plasma that is generated by resistive losses in the conducting shell (Appendix E). This drag force (power) may be counteracted by simple flaring of the conducting shell, thereby allowing an alpha-particle-driven expansion of the plasma to provide the drag power. This passive drive mechanism appears more desirable when compared to active moving-mirror coils for several reasons; maintaining equilibrium and stability of the plasmoid while imposing mirror fields may be difficult; energizing a set of active drive coils could take a substantial amount of electrical recirculation energy for an elongated compact toroid because of the high dissipation in the conducting shell and using a passive translation method avoids the complexity of the moving-mirror coils located in the power-producing regions of the reactor. Providing the translation by expansion of the plasmoid as a result of flaring the conducting shell directly converts alpha-particle energy to translational power, leading to a totally passive burn section.

Minimizing the translational drag is crucial if the translation is to be provided by simply flaring the conducting shell. Location of a room-temperature conducting shell (typically a $\lesssim$ 0.05-m-thick, litzed and transposed copper coil to eliminate eddy current losses) outside the tritium breeding blanket but within the radiation shield reduces the resistive heating by approximately an order of magnitude when compared to a solid-metal conducting shell ($\lesssim$ 0.05-m thick) located at or acting as the first wall. Locating the conducting shell outside the blanket also avoids both severe neutron irradiation problems in a thick metallic structure and potential tritium breeding difficulties (although, if not too thick, copper does act as a neutron multiplier[23]). Also, a relatively large portion (~ 40% in a 0.02-m thick copper shell[23]) of the neutron energy is deposited in a first-wall shell, creating cooling difficulties along with problems of neutron-induced dimensional and mechanical/electrical-properties changes.

Passively translating the plasmoid by expansion of the plasma, however, reduces the instantaneous power and varies the first-wall neutron loading along the axial length. This effect can be minimized by locating the shell outside of the blanket region as noted above. Maintaining an axially uniform power density is desirable to minimize obvious engineering complexities and should produce the most economically viable system. By properly flaring the conducting shell, the plasmoid velocity may be tailored to give a nearly constant first-wall loading (or axial power density) along the length of the burn chamber. The velocity must be varied approximately as $v \propto P_N/r_w$, where $P_N(W)$ is the instantaneous neutron power. As the plasmoid translates along the burn section, continued expansion lowers the instantaneous power density requiring the plasmoid velocity to be reduced if a constant axial power density is desired. Specifying the inlet velocity as a multiple of ℓ/τ_s (typically 2-5 times), where the skin depth, τ_s, is associated with loss of magnetic flux enclosed by the area between the first-wall and plasma separatrix, the reactor length, L, is determined when $v \lesssim \ell/\tau_s$. The inlet velocity then determines the length of the reactor. Because the inlet velocity is variable the resultant reactor length to some extent tends to be arbitrary and must be determined primarily be economic considerations.

Movements of the FRC inside a flared shell is inherently unstable to axial motion.[29] For a thick shell surrounding a translating plasmoid the resistive dissipation, P_{DRAG}, is nearly a constant irrespective of speed; the drag force on the plasma is P_{DRAG}/v. Once the plasmoid begins to move, acceleration to a velocity near the Alfvén speed is expected to occur rapidly, (the plasmoid mass is very small) causing the drag force to be reduced to nearly zero. This implies the reacting plasma would quickly be ejected through any burn chamber of reasonable length with little resultant neutron yield. Inserting a thin shell (highly-permeable to flux on a time scale of τ_s) near the first wall introduces a stabilizing drag force proportional to the plasmoid velocity (Sec. VII.B.3.). The drag force associated with this particular component stabilizes the system while requiring only a minimal extraction of energy from the translating toroid; this loss is estimated to be $\lesssim$ 1% of the conducting shell losses.

Upon reaching the end section of the reactor, a portion (0.3-0.5) of the plasma and magnetic field energy is extracted electrically by expansion of the depleted plasmoid. The conducting shell at this point is electrically

connected as a magnet coil allowing flux to escape and energy to be extracted by a capacitive element (i.e., a rotating machine). Movement of the plasmoid into this end region provides all necessary electrical switching, and no opening switches are required to extract the stored plasma/magnetic energy. The remaining energy after plasma expansion and quench is recovered thermally and converted to electricity by a conventional thermal conversion cycle.

B. Energy-Balance Computation

Overall reactor energy balance provides a performance measure of the electrical power plant. Figure IV-2 schematically depicts the CTOR energy balance. A capacitor bank energy W_{BANK} is transferred into the implosion heating chamber with an electrical efficiency of 0.5, with losses occuring in the external circuit and, therefore, not recoverable. The remaining energy applied to the FRΘP source heats the plasma to an initial starting temperature and provides the initial bias field. No reversibility of electrical energy is assumed in this region (i.e., energy is not assumed to "ring" back into the FRΘP capacitor bank). The preheated plasma is subsequently compressed to

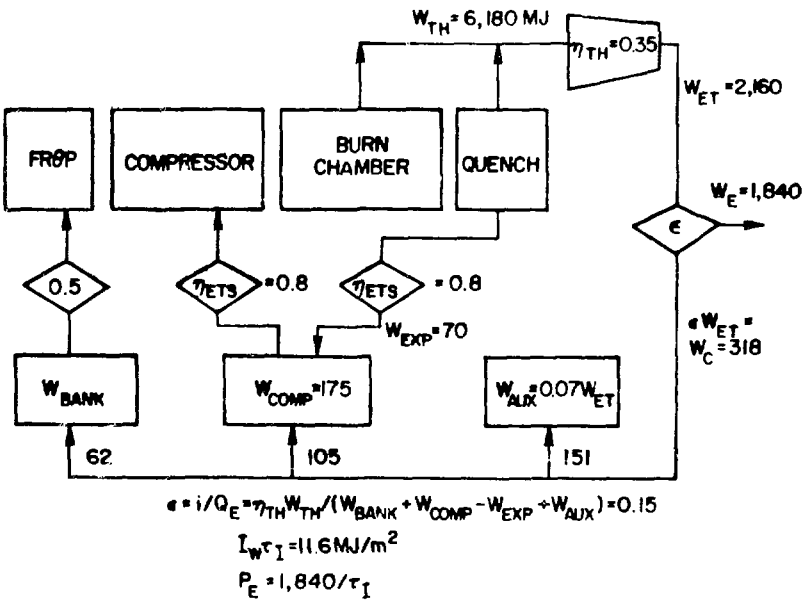

Fig. IV-2. CTOR energy balance used in conjunction with time-dependent model to evaluate reactor performance.

ignition using the energy from a mechanical energy store, W_{COMP}, this compressional energy store having a transfer efficiency $\eta_{ETS} \simeq 0.8$. Once again, reversibility in transfer from the energy store to the compressor is not assumed. Upon entering the burn chamber, the translation power required to overcome conducting shell losses (Appendix E) is provided by alpha-particle energy via the natural dynamics of a burning plasma. As the burn proceeds, the plasma thermal output includes neutron, W_N, radiation, W_{RAD}, conduction, W_{COND}, and internal plasma W_{INT} energies. The plasmoid motion is terminated in a quench region where plasma expansion converts a portion of magnetic field and internal plasma energy directly to electrical energy; this direct-conversion energy would be used to recharge the mechanical energy store used to compress the plasmoid initially. The remaining plasmoid energy is extracted through a conventional thermal cycle and contributes to the total thermal energy, W_{TH}, which is converted to electricity with an efficiency η_{TH} to produce a gross electric energy W_{ET}. Auxiliary energy requirements W_A (pumps, cryogenics, plant operation, etc.), given as a fraction f_A of W_{ET}, completes the energy balance. A fraction ε of the total electrical energy, W_{ET}, must be recirculated as makeup energy $W_c = \varepsilon W_{ET}$, the net electric energy is then $W_E = (1-\varepsilon)\ W_{ET}$, and the overall plant efficiency is $\eta_p = (1-\varepsilon)\ \eta_{TH}$. On the basis of this energy balance, an engineering Q-value, Q_E, is defined as

$$Q_E = \frac{W_{ET}}{W_c} = \frac{1}{\varepsilon} = \frac{\eta_{TH}\ W_{TH}}{W_{BANK} + W_{COMP} - W_{EXP} + W_{AUX}} \quad . \tag{IV-1}$$

The quantity Q_E is used as a primary measure of CTOR performance (Sec. VI.C.).

C. Reactor Physics

1. Stability Properties. As noted in Sec. IV.A., only the FRΘP approach to the formation of an FRC has a substantial experimental basis at this time. The physics parameters and constraints, consequently, are based upon this approach for the particular reactor design presented here. This specific design decision is based on present state-of-knowledge, but certainly does not preclude other more technologically attractive schemes, should future experiments so indicate. Recent experimental evidence[24,25,30,31] has been encouraging for the FRΘP, with confinement times of ~ 100 μs and temperatures

$T_i \simeq 2T_e \simeq 200$ eV in a plasmoid having a separatrix radius of only ~ 0.05 m. The MHD stability reflected by present FROP experiments is thought to be a consequence of establishing an elongated configuration with the plasmoid surface near the conducting shell. These two conditions are imposed on the reactor calculations by requiring sufficient elongation ($\ell/r_s \gtrsim 7$) and a large ratio of separatrix to conduction shell radius ($x_s = r_s/r_c \gtrsim 0.5$) as is achieved in present experiments. Experimental evidence indicates enhanced transport as the plasmoid is moved away from the conducting shell.[30] As calculated in Appendix B, the fraction of plasma inside the separatrix is given by $\beta_s = 1 - 0.5x_s^2$, a relationship that appears to be independent of plasma density profiles. Large values of beta, therefore, are achieved as x_s is reduced, requiring steep plasma gradients (Appendix A) and resulting in enhanced transport.

Earlier FRC studies as applied to the field-reversed mirror (FRM)[5-9] have stressed the need for finite-Larmor-radius (FLR) stabilization. Consequently, these FRM reactor studies have directly constrained the ratio, $S = a/\rho_i$, of plasma radius to ion Larmor radius to be $\sim$ 4-5. The constraint that $S \lesssim 5$, although conceivably valid for plasmoids with $\ell/r_c \simeq 1$ and without toroidal field, has a dramatic impact upon the ultimate plasma parameters for the reactor; generally, FRM/FRC systems with $S \lesssim 5$ must operate at high fields (> 5-6 T) and plasma temperatures (70-100 keV) in order to achieve a modest Q-value ($Q \gtrsim 5$).[5-9] Furthermore, since values in excess of $S \sim 10$ are generally required before the level of alpha-particle retention is sufficient for a self-sustained (ignited) operation, FRC plasmoids with $S \lesssim 5$ generally result in driven systems. Given the correctness of the assumptions of wall stabilization, elongated plasmoid equilibria and a relatively unconstrained value of S ($\lesssim$ 20-30, rather than $\lesssim 5$), the FROP/FRC reactor embodiment naturally develops into one that is translating, high-beta and ignited; such a system must move its plasmoid continually at a velocity that is compatible with the plasmoid length and the electrical skin time, τ_s, of an electrically conducting shell (i.e., $v \sim \ell/\tau_s$). It should be emphasized, however, that the stability requirements of FRC configurations without toroidal field, as inferred by plasmoid S-value and/or shape, represents a major uncertainty for any reactor projection, and, therefore deserves more theoretical emphasis; relevant experimental evidence is not expected to clarify this important issue for at least a few years.

Analytical equilibrium calculations described in the following section and Appendix B have provided insight into the expected shape of the pressure profile. These results predict actual gradient lengths at the plasma edge to be 0.3 - 0.5 times a/ρ_i for values of $x_s \lesssim 0.5$, with the gradient length approaching a/ρ_i as $x_s \to 1$. Thus, even the large radius ($r_s \sim 1$ m) plasmas in a reactor may have gradient lengths of only approximately ten ion-gyroradii at operating temperatures of 10-20 keV. This condition implies FLR stabilization may still play a prominent role in the reactor systems envisaged in this study, this issue requiring considerably more theoretical analysis.

2. Plasma Model. A detailed description of the computer code used to perform the CTOR systems design is given in Appendix D along with a development of the plasma burn model. An analytic equilibrium expression is determined from an axial force balance that has been performed in conjunction with radial pressure balance. As discussed in Appendix B, three-dimensional equilibrium expressions are derived for a sharp-boundary model plasma. The resulting equations allow the use of a point-plasma numerical burn computation to follow three-dimensional spatial variations. A key result from these equilibrium calculations is that the fraction of plasma inside the separatrix is $\beta_s = 1 - x_s^2/2$. This expression is shown to be generally valid (Appendix B) for any pressure profile and is used to show that the sharp-boundary model is a good representation of the expected profiles (Appendix A). This model is further substantiated by diffuse profile equilibrium expressions which yield essentially the same result (Appendix B) as the sharp-boundary model. Experimental evidence[24] also indicates a nearly uniform temperature across the bulk of the plasma, indicating the presence of steep gradients near the plasma edge. Equilibrium arguments dictate edge gradients of approximately 10 ion-gyroradii for values of $S = a/\rho_i \simeq 30$ which are typical of the reactor burn calculation.

In summary, equilibrium results for diffuse profiles yield essentially the same results as the sharp-boundary case (Appendix B). The sharp-boundary model is expected to be a good representation of the plasma profile for $x_s \lesssim 0.75$ (Appendix A). The bulk temperature of the plasma is expected to be nearly isothermal. Sharp-boundary profiles, therefore, are used throughout this study.

A consistent calculation of the multi-species plasma (ions, electrons and alpha-particles) follows the three-dimensional spatial variations of the plasmoid. Alpha-particle thermalization using a Fokker-Planck formalism, Bremsstrahlung radiation losses, thermal conduction and particle diffusion are included in this time-dependent model. Starting with the post-implosion phase, the plasma trajectory is followed through the tapered compression chamber into the burn section where conducting shell losses (translational drag) are counteracted by radial plasma expansion. The required conducting shell radius, outside a 0.5-m thick blanket and plasmoid length, ℓ, are defined by experimental results ($r_c/r_s \lesssim 2$ and $\ell/r_s > 7$). An overall energy balance is performed along with a spatial calculation of thermal and structural response of the first wall (one-dimensional calculations at various axial positions along the machine).

The following subsections summarize the numerical simulation of startup, burn (translation) and quench. Further details of the plasma simulation model are found in Appendix D.

3. Startup. Plasma startup includes the initiation phase and compressional phase needed to achieve ignition. The proven source for generation of the elongated field-reversed configuration is the Field-Reversed Theta-Pinch (FRΘP) which is also used in this reactor study as the plasma generation device. Appendix F contains a summary of relationships for a FRΘP based upon a Marshall-coil[28,32] startup. These equations relate external parameters (voltages, currents, capacitor bank energy, etc.) to the plasma post-implosion conditions used as the initial conditions in the plasma simulation code. Even though the FRΘP is used in this study, other sources are potentially more attractive. For example, a coaxial theta-pinch may allow a technologically simpler startup involving slower timescales. The ultimate goal would be plasma startup using rotating machinery (homopolar motor/generator), omitting the need for the FRΘP capacitor bank.

Upon achieving 1-15 keV from the FRΘP, the plasmoid enters the traveling-wave compressor[33] section and is adiabatically compressed to ignition (~ 6 keV) using the energy from a homopolar motor/generator. Typical trajectories are calculated analytically in Appendix C and are shown to agree well with two-dimensional magnetohydrodynamics calculations. The high-efficiency of this tapered shell compressor is also illustrated. Using the equilibrium expressions, the plasma burn code numerically follows the

compression which occurs over a period of 0.1 s. The energy required to drive the compressor is associated with energy added to the plasma and field over the plasmoid length, ℓ. Actual numerical simulations of the traveling-wave network are also shown in Sec. VII.B.2.

4. Thermonuclear Burn. Upon entering the thermonuclear section, the plasma ignites and moves through the system at a velocity tailored to provide a nearly uniform first-wall neutron loading. The required velocity variation is found to be $v \propto P_\alpha/r_w$ with the magnitude of the inlet velocity parametrically varied from 2-5 (ℓ/τ_s) with τ_s being associated with the loss of flux between the first wall and separatrix. Radial plasmoid expansion is required to overcome image current losses in the conducting shell. The expanding plasma inside the flared shell results in a lower alpha power, P_α, which decreases the plasmoid velocity until $v < \ell/\tau_s$ and quench occurs. Specific equations describing the burn model and translational properties are described in Appendix D and E, respectively.

Providing translational power by expansion of the conduction shell results in a plasmoid motion that is inherently unstable.[29] An electrically thick conducting shell dissipates power, P, nearly independent of plasmoid velocity. The resulting drag force is simply $F_D \propto P/v$. The large amount of power required to overcome the drag force is capable of accelerating the plasmoid to near the Alfvén velocity with $F_D \to 0$ as $v \to \infty$. Slightly excessive flare in the conducting shell accelerates the plasma into the quench region before significant burn could occur. Placing a thin conducting shell (only ~ 1 mm of Cu) near the first wall (inside the conducting shell) that is highly permeable to flux, produces a drag force that stabilizes the translation, $F_D \propto Pv$.

5. Quench. Upon termination of motion, plasma expansion allows the separatrix radius to closely approach the first wall. This is achieved by allowing the trapped flux between the separatrix and conducting shell to be electrically withdrawn. Using the conducting shell as a normal conducting coil connected to a homopolar motor/generator allows approximately 30-40% of the residual plasma/field energy inside the conducting shell to be extracted directly as electrical energy. No opening switches are required as the plasma motion provides the switching. Final quench is achieved *via* a gas blanket having a density comparable to the plasma density.[34]

V. DEVELOPMENT OF POINT DESIGN

A. Analytic Calculation

Analytic calculations are performed for an optimal power cycle in which the ignited burn is sustained at ~ 10 keV by alpha-particle heating. These calculations are made only to examine parameter tradeoffs and sensitivities as well as to guide the more detailed numerical simulation of the CTOR design point. For the analytic model transport losses are assumed to prevent the plasma from overheating, although the magnitude and mechanism of particle/energy transport was left unspecified. All burn cycles investigated are presumed to be unrefueled or "batch", in which the initial fuel charge is partially burned as the plasmoid moves at velocity $v \simeq \ell/\tau_s$ through the linear burn section. This approximation implies the flow velocity, v, is taken as a constant of the plasmoid length, ℓ, which in turn is presumed fixed. This idealized situation could only be achieved using a system of active mirror coils that enforces the constant velocity constraint.

The total thermal power developed by the reactor is

$$P_{TH} = 2\pi r_w \, I_w \, L \, (M + E_\alpha/E_N) \quad , \tag{V-1}$$

where $I_w(W/m^2)$ is the first wall 14.1-MeV neutron loading, and M is the total neutron fusion release in the blanket relative to the 14.1-MeV primary fusion neutron; typically, for a blanket multiplication M = 1.16, $(M + E_\alpha/E_N) = 1.42$. The neutron wall loading is given by

$$I_w(W/m^2) = 0.25(n\tau_B)^2 \langle\sigma v\rangle \, E_N \beta_s \, f_\ell \, \pi r_s^2/2\pi r_w \, \tau_B^2 \quad , \tag{V-2}$$

where $E_N = 2.26(10)^{-12}$ J/fusion (14.1 MeV/n). The fraction of the area inside r_s filled with plasma is $\beta_s = 1-0.5\, x_s^2$ (Appendix B), while the fraction of burn-chamber length filled with plasma at any given time is denoted by f_ℓ. For example, a 50-m-long burn chamber containing one 5-m long plasmoid, would operate with $f_\ell = 0.1$. The first-wall neutron loading, I_w, has been expressed in terms of the Lawson-like parameter $(n\tau_B)$ where the total burn time, τ_B, can be expressed as follows in terms of the burn-chamber length, L

$$\tau_B = \tau_s \, (L/\ell) \quad , \tag{V-3}$$

which imposes the constraint of plasmoid velocity. Substituting Eq. (V-3) into Eq. (V-2) for τ_B, solving for the reactor length, L, and using the result in Eq. (V-1) gives the following expression for the thermal power

$$P_{TH}(W) = 5.37(n\tau_B)(M + E_\alpha/E_N)(I_W\langle\sigma v\rangle)^{1/2}(\eta/\delta)(\Delta b+\delta/2)^{3/2} f_\ell^{1/2} R_\ell f(y)$$

$$f(y) = \frac{\beta_s^{1/2} x_s (1 - y)^{1/2}}{[(1 - y)^2 - x_s^2] y^{3/2}} \quad , \tag{V-4}$$

where $y = (\Delta b + \delta/2)/r_c$, $x_s = r_s/r_c$ and $R_\ell = \ell/r_c$. The expression for skin depth, τ_s, as derived in Appendix E, and the geometric definition for the conducting-shell radius, $r_c = r_w + \Delta b + \delta/2$ has been used in the formulation of Eq. (V-4).

The total thermal power as given by Eq. (V-4) is dependent upon a set of known (or desired) quantities and the radial dimensions of the burn section grouped in f(y). Operating the plasma at 10 keV requires that $\langle\sigma v\rangle = 1.12(10)^{-22}$ m^3/s, and desiring a relatively high DT fuel burnup ($f_B = 0.22$) requires that $n\tau_B = 5(10)^{21}$ s/m^3.

Use of a room-temperature copper shell fixes η at $2(10)^{-8}$ Ω m, although the shell thickness, δ, must be determined. The cross-sectional area for flux diffusion in the conducting shell must be significantly less than the area between the separatrix and the first wall. Establishing image currents throughout the shell requires rapid flux penetration until the currents established in the shell have reached a maximum. Taking $\delta = 0.05$ m, the shell conductor cross section represents 24% of the cross-sectional area encompassed by the first-wall and separatrix radii for $r_s = 0.85$ m, $r_w = 1.2$ m and $\Delta b = 0.5$ m. The corresponding loss of magnetic flux into the conducting shell for this particular system as the plasmoid traverses the bore is considered reasonable (Appendix E).

Applying the geometric physics constraints (Sec. IV.C.1.) of $x_s = 0.5$, $R_\ell = 3.5$ and using $r_w = r_c - \Delta b - \delta/2$, where $\Delta b = 0.5$-m is the blanket thickness, a curve of total thermal power versus separatrix radius shown in

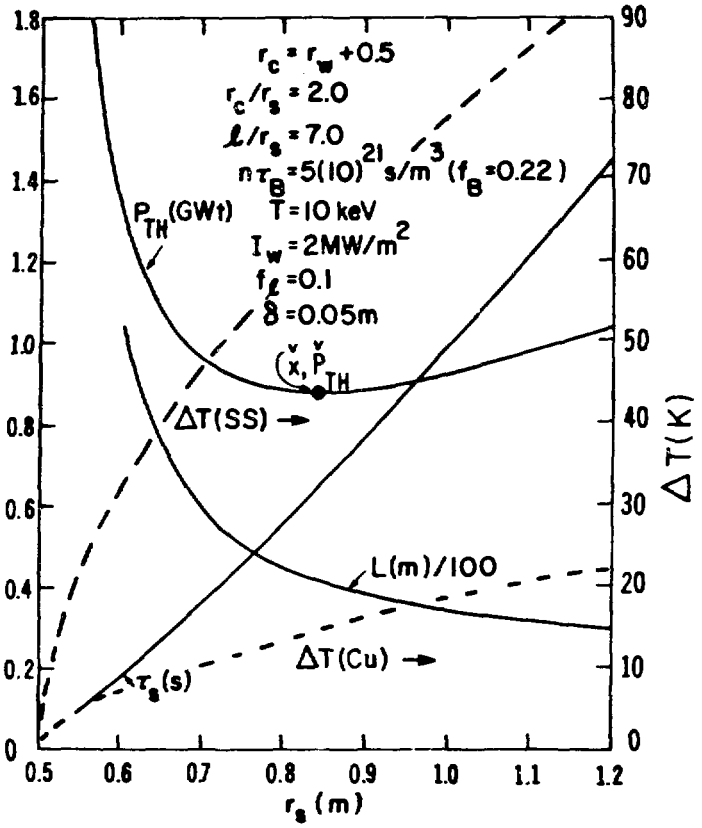

Fig. V-1. Dependence of P_{TH}, L, τ_s and first-wall thermal excursion for f_ℓ fixed at 0.1.

Fig. V-1 results. For this case I_w is taken as $2(10)^6$ W/m^2, and the fraction of axial length filled with plasma, f_ℓ, is taken as 0.1. A minimum reactor power equal to 880 MWt occurs for L = 40 m, r_s = 0.83 m, r_w = 1.2 m and r_c = 1.7 m. The reactor power decreases as r_s is reduced, which is primarily a consequence of the decrease in cross-sectional area. As r_s decreases below 0.83 m, the effective skin time, τ_s, dramatically decreases, causing the plasmoid velocity required for shell stabilization to increase. To satisfy the Lawson-like criterion in this regime, the reactor must become much longer and the total power correspondingly rises as r_s is further decreased.

The position of minimum exhibited in Fig. V-1 depends only upon radial geometric variables in Fig. V-2, as defined by the function f(y) in Eq. (V-4). The spectra of minima for various x_s is then determined by evaluating df(y)/dy = 0; a cubic equation in y results with one real and two imaginary roots. The real root can be approximated (within 1%) as

$$y = \frac{\Delta b + \delta/2}{r_c} = 0.6\ (1-x_s) \qquad (V-5)$$

for the region of interest, $0.5 \leq x_s \leq 1.0$. The minimum values of the function f(y) are plotted in Fig. V-2 using Eq. V-5 for $y = (\Delta b + \delta/2)/r_c$. The geometric minima of thermal power are then predicted by Eq. (V-5) to be $r_c = 1.75$ m, $r_w = 1.22$ m, $r_s = 0.87$ for $x_s = 0.5$. The value f(y) = 10 from Fig. V-2 predicts a thermal power of 880 MWt from Eq. (V-4), as verified by Fig. V-1. The curve f(y) is derived for a constant value of f_ℓ, which as

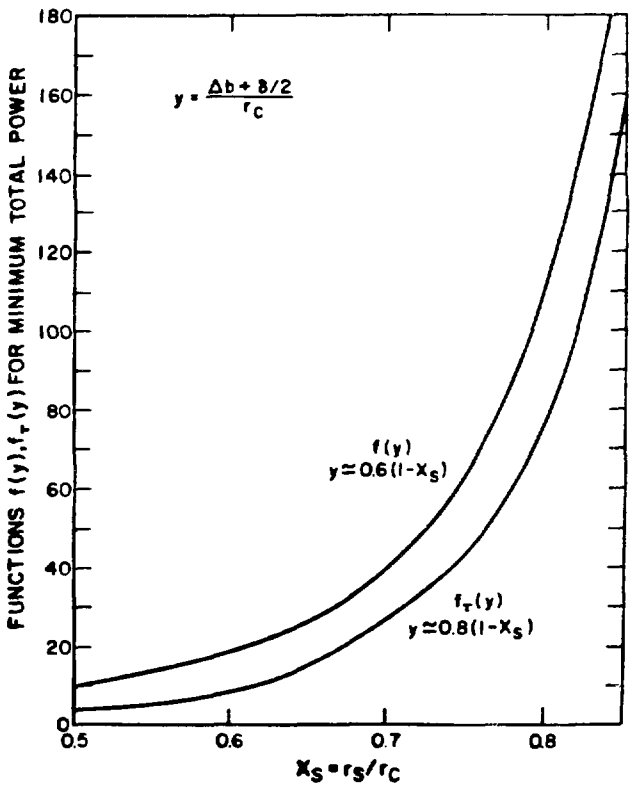

Fig. V-2. Minimum values of the function f(y) and $f_T(y)$ for the values of y shown.

inferred in Eq. (V-2), corresponds to $\tau_B \sim r_w^{1/2}$ for I_w fixed. As will be shown later in this section, this case is of particular importance because the subsequent numerical calculations also predict $\tau_B \sim r_w^{1/2}$ for the conditions imposed above.

Another optimization may be performed assuming the dwell time between the injection of plasmoids, τ_I, is a fixed parameter. Noting that

$$f_\ell = \tau_s/\tau_I \quad , \tag{V-6}$$

for a plasmoid of fixed dimensions (approximation of time-independence), the total thermal power is expressed by

$$P_{TH} = 4.26(10)^{-3} \; (n\tau_B)(M+E_\alpha/E_N)(I_w\langle\sigma v\rangle)^{1/2}(n/\delta)^{1/2} \; (\Delta b + \delta/2)^2 \; R_\ell \; f_\tau(y)/\tau_I^{1/2}$$

$$f_\tau(y) = \frac{\beta_s^{1/2} \; x_s \; (1 - y)^{1/2}}{(1 - y)^2 - x_s^2 \; y^2} \quad . \tag{V-7}$$

The spectra of minimum power values in this case is found from the condition that $df_\tau(y)/dy = 0$, which gives to within 3%

$$y = \frac{\Delta b + \delta/2}{r_c} \simeq 0.8 \; (1-x_s) \quad , \tag{V-8}$$

for the region of interest, $0.5 \leq x_s < 1.0$. The minimum values of $f_\tau(y)$ are also plotted in Fig. V-2 using Eq. (V-8). Both cases yield essentially the same behavior with both f(y) and $\sim f_\tau(y)$ being proportional to $\sim r_c^3$ (or y^{-3}). For a fixed neutron wall loading, I_w, the radial variation of the burn chamber through the first wall radius, r_w, contributes only a linear dependence to the total thermal power, P_{TH}. The total reactor length then increases as r_c^2 when x_s is increased.

TABLE V-I

TYPICAL CTOR PARAMETERS FOR MINIMUM POWER AS DETERMINED FROM THE SIMPLE ANALYTIC MODEL

PARAMETER	CONSTANT f_ℓ	CONSTANT τ_I
Total thermal power, P_{TH}(MWt)	880	1141
Burn chamber length, L(m)	42	85
Separatrix radius, r_s(m)	0.83	0.63
Plasmoid length, ℓ(m)	5.8	4.4
First-wall radius, r_w(m)	1.2	0.75
Conducting shell radius, r_c(m)	1.7	1.25
Shell skin time, τ_s(s)	0.6	0.2
Burn time, τ_B(s)	4.5	4.2
Injection time, τ_I(s)	6.2	2.2(f_ℓ = 0.1)
Translational velocity, v(m/s)	9.4	20.4
Plasma density, n(10^{21}/m^3)	1.1	1.2
Compressed field, B_i(T)	3.0	3.1
Vacuum field, B_o(T)	2.3	2.3
Engineering power density, $P_{TH}/\pi r_c^2 L$(MW/m^3)	2.4	2.7
First-wall temperature rise for copper, ΔT(K)	14.2	14.9
First-wall temperature rise for stainless steel, ΔT(K)	62.1	65.3
ASSUMED OR FIXED PARAMETERS		
Blanket thickness, Δb(m)	0.5	
Plasma temperature, T(keV)	10	
Fusion-neutron wall loading, I_W(MW/m^2)	2.0	
Conducting shell thickness, δ(m)	0.05	
Duty factor, $f_\ell = \tau_s/\tau_I$	0.1	
Lawson parameter for 22% DT burnup, $n\tau_B$(10^{21}s/m^3)	5.0	
Equilibrium/Stability constraints		
• x_s	0.5	
• ℓ/r_s	7.0	

Table V-I lists the minimum thermal powers at the optimized radial dimensions obtained by imposing the minimum power constraint for both f_ℓ and τ_I held constant and taking $x_s = 0.5$. The assumed and/or fixed parameters are also given. The parameter f_ℓ has been taken as 0.1 for both cases which yields nearly identical temperature excursions on the first wall. These thermal excursions are computed on the basis of an exposure of the first wall to Bremsstrahlung radiation for a time, τ_s, and are also shown in Fig. V-1. A "thermally-thick" wall of copper or stainless steel is used to compute the thermal loadings for this analytical estimate; more detailed numerical results are given in Sec. VII.B.3. for the CTOR design point.

A plot of P_{TH}, L, τ_B, and ΔT for a copper first wall is given in Fig. V-3, where f_ℓ is treated parametrically for both the f_ℓ-and τ_I-constrained cases. In either case the reactor power decreases as f_ℓ is reduced as a results of the decreased reactor length required to achieve the desired value of $n\tau_B$. This length reduction occurs at the cost of higher first-wall temperature excursions and larger energy requirements for the plasmoid source (increasing density). Minimizations for both constant f_ℓ or τ_I yield similar results for a given f_ℓ, as illustrated in Fig. V-3.

These analytic results are useful for estimating the minimum reactor power under ideal burn conditions. The most sensitive parameter is the blanket thickness ($P_{TH} \sim \Delta b^{3/2} \rightarrow \Delta b^2$), although the value for Δb can only be reduced from 0.5 to ~ 0.35 m[28] depending on the tritium breeding materials used in the blanket; the reactor power can potentially be reduced by a factor of approximately two. The value of $n\tau_B$ is determined by economic considerations requiring a good energy balance (low recirculating power fraction). Interestingly, the first-wall loading, I_w, impacts the total power constraint only as a square root. This parameter is primarily determined by wall lifetime and economic considerations, with 2-4 MW/m^2 being near optimal. Increasing the conducting shell thickness, δ, also reduces the reactor output according to a practical dependence that varies by $\delta^{1/2}$ to δ; the cross-sectional area of this shell must be much less than the area between r_w and r_s to avoid a large instantaneous loss of magnetic flux as the plasmoid moves. The parameter that allows greatest variation in the reactor power is f_ℓ (or correspondingly, τ_I). Reducing f_ℓ (or $1/\tau_I$) reduces the power by $f_\ell^{1/2}$ (or τ_I -1/2), although the size of the plasma FRCP source increases correspondingly ($f_\ell^{-1/2}$, $\tau_I^{1/2}$) while the first-wall temperature excursion

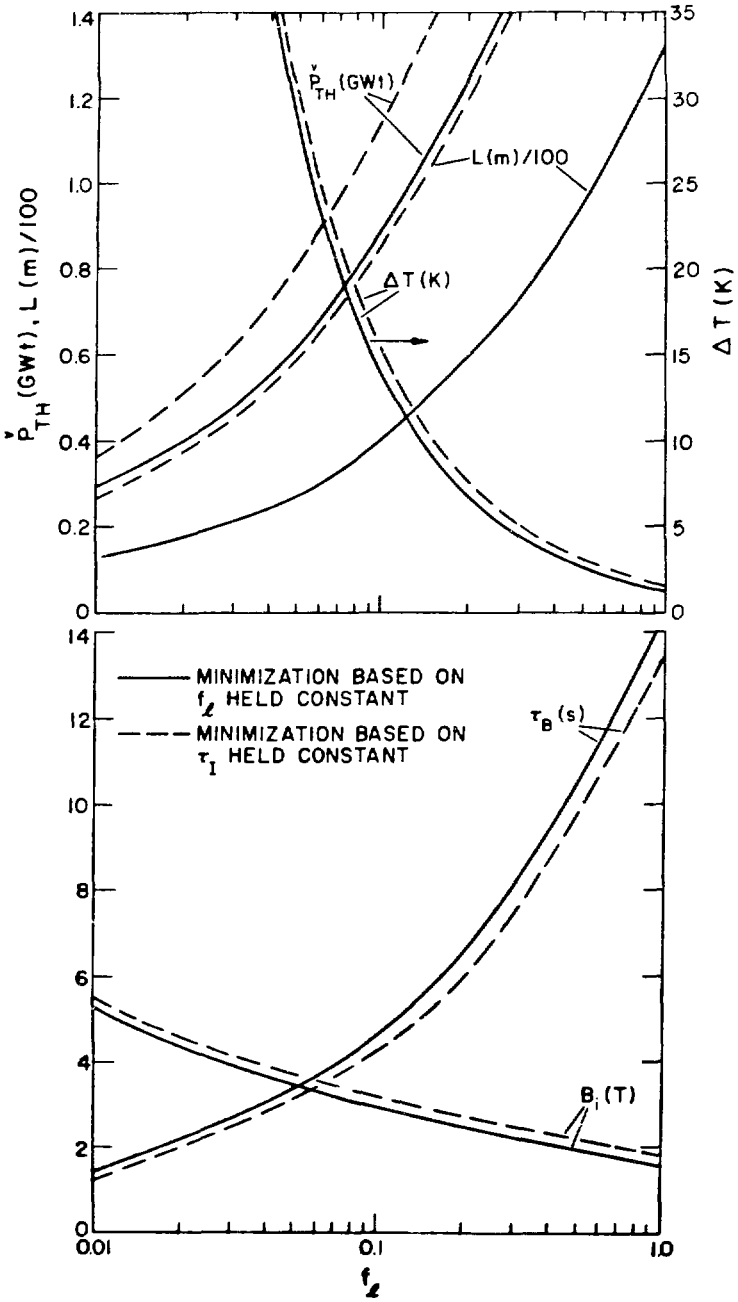

Fig. V-3. Dependence of P_{TH}, L, τ_B, and ΔT on f_ℓ for both f_ℓ and τ_I-constrained cases.

increases as f_ℓ (or τ_I^{-1}). This particular variation corresponds to increasing the plasmoid density, which allows a shorter burn time, τ_B, to achieve a given plasma yield (i.e., $n\tau_B$).

As noted above, the specific choice of I_w, $n\tau_B$, Δb and f_ℓ is largely determined by engineering and/or economic considerations. Plasma transport considerations will ultimately determine the minimum allowable separatrix radius, r_s, along with the required value of x_s. By imposing a minimum power constraint, these variables are actually coupled via Eq. (V-5) for the case where f_ℓ is held constant. The only variable remaining to be determined is the value of the shell thickness, δ. For a given value of x_s, Eq. (V-4) for P_{TH} is plotted in Fig. V-4 on an arbitrary scale versus $\delta/\Delta b$. A strong reduction in power is seen as $\delta/\Delta b$ is increased until $\delta/\Delta b \sim 0.25$; beyond this point little is gained for much greater increases in $\delta/\Delta b$. This reduction in power, however, is not achieved without the penalty of increased size of the FRΘP source, E_s. This particular plasmoid source essentially increases in size as r_c^3 or $(1 + \delta/2\Delta b)^3$, which is also plotted on Fig. V-4. The increase in the FRΘP source, as measured by E_s, provides a strong incentive to keep

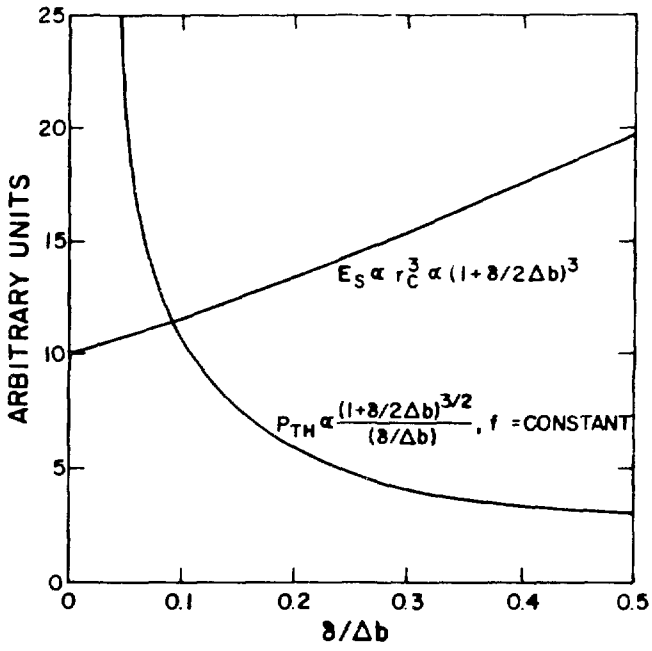

Fig. V-4. Relative magnitude of thermal power, P_{TH}, and required size of theta-pinch source, E_s, for x_s fixed.

$\delta/\Delta b$ within the range 0.1-0.25, which corresponds to an increase in E_s of 16%-40%, respectively, relative to the base case.

The analytic design point listed in Table V-I correspond to $\delta/\Delta b = 0.1$, indicating that the power could be reduced a factor of two (actually the reactor would be reduced in length by ~ 2) at the cost of a ~ 20% increased FROP size. As seen in Fig. V-4 much larger decreases in power would probably not be attractive because of large increases in the FROP source requirements. Using Fig. V-3 and V-4, a minimum power design may be identified at larger values of x_s, which may be required by physics considerations. For example, taking $x_s = 0.75$ increases f(y), or correspondingly P_{TH}, by a factor of 6.4. This increase would result in a power output of 5500 MWt using the same parameters as listed in Table V-I for $x_s = 0.5$. However, increasing $\delta/\Delta b$ from 0.1 to 0.25 decreases this power to 2550 MWt. Also decreasing Δb from 0.5 to 0.4 m further reduces this power to 2,400 MWt and also requires a δ of only 0.1 m. The design point for $x_s = 0.75$ is listed in Table V-II for f_ℓ held constant: this preliminary result from the analytic model is used to predict the results from the detailed numerical simulations.

B. Comparison of Time-Dependent and Analytic Calculation

A more realistic modeling of the plasma burn requires a time-dependent numerical plasma burn simulation. The computer model used for this more detailed description is discussed in Sec. IV.C. The analytical model (Sec. V.A.) is used as a guide, providing the general trends and parameter sensitivities, whenever possible. The major differences between the analytical and time-dependent results must be identified if the analytical calculations are to be useful. The assumptions used in the analytic model are compared to the actual FRC plasma behavior as predicted by the numerical model, in Table V-III. Operating at a constant temperature near 10 keV is the desired goal in each case. The numerical calculation will predict the value of $n\tau_B$ required to achieve a good energy balance. Analytically imposing a constant plasmoid velocity (ℓ/τ_s) and constant plasma density would result automatically in a uniform first-wall loading throughout the burn chamber, which is the constraint imposed on the numerical calculation; in this case, however, the plasma density and plasmoid velocity are variable. Specifically, the density is a maximum at the burn section inlet and decreases along with

TABLE V-II

TYPICAL CTOR PARAMETERS FOR MINIMUM POWER WITH x_s = 0.75 AS DETERMINED FROM THE SIMPLE ANALYTIC MODEL

PARAMETER	VALUE
Total thermal power, P_{TH}(MWt)	2400
Burn chamber length, L(m)	53
Separatrix radius, r_s(m)	2.25
Plasmoid length, ℓ(m)	10.5
First-wall radius, r_w(m)	2.55
Conducting shell radius, r_c(m)	3.0
Shell skin time, τ_s(s)	1.51
Burn time, τ_B(s)	7.6
Injection time, τ_I(s)	15.1
Translational velocity, v(m/s)	6.9
Plasma density, n(10^{21}/m^3)	0.66
Compressed field, B_i(T)	1.3
Vacuum field, B_o(T)	0.57
Engineering power density, $P_{TH}/\pi r_c^2 L$(MW/m^3)	1.6
ASSUMED OR FIXED PARAMETERS	
Blanket thickness, Δb(m)	0.4
Plasma temperature, T(keV)	10
Fusion-neutron wall loading, I_w(MW/m^2)	2.0
Conducting shell thickness, δ(m)	0.1
Duty factor, $f_\ell = \tau_s/\tau_I$	0.1
Lawson parameter for 22% burnup, $n\tau_B$(10^{21}s/m^3)	5.0
Equilibrium/Stability constraints	
• x_s	0.75
• ℓ/r_c	3.5

the velocity as the burn proceeds, in accordance with the constant I_w and stability/equilibrium constraints.

A typical burn trajectory is given in Fig. V-5, showing the electron, ion, and alpha-temperatures along with ion and alpha-particle densities versus time for an energy confinement time equal to 200 Bohm times. The use of this $\tau_E \simeq 200\ \tau_{Bohm}$ energy loss time is extrapolated from tokamak experimental data

TABLE V-III

QUALITATIVE COMPARISON OF ANALYTICAL AND NUMERICAL MODEL

ANALYTIC	NUMERICAL (TIME-DEPENDENT)
Constant operating temperature of 10 keV	Analytic assumption represents desired goal, actual temperature determined by the simulated plasma dynamics.
Assumed value of $n\tau_B$ $(5(10)^{21}$ $s/m^3)$	Calculated $n\tau_B$ based upon detailed plasma energy balance
Moving mirror coils effectively allow constant plasmoid, ℓ/τ_s, velocity	Passive translation by flared conducting shell results in varying plasma velocity (from 2-5 ℓ/τ_s at inlet to ℓ/τ_s at outlet) to give uniform first-wall neutron loading.
Constant density	Variable
Constant plasmoid dimensions	Variable

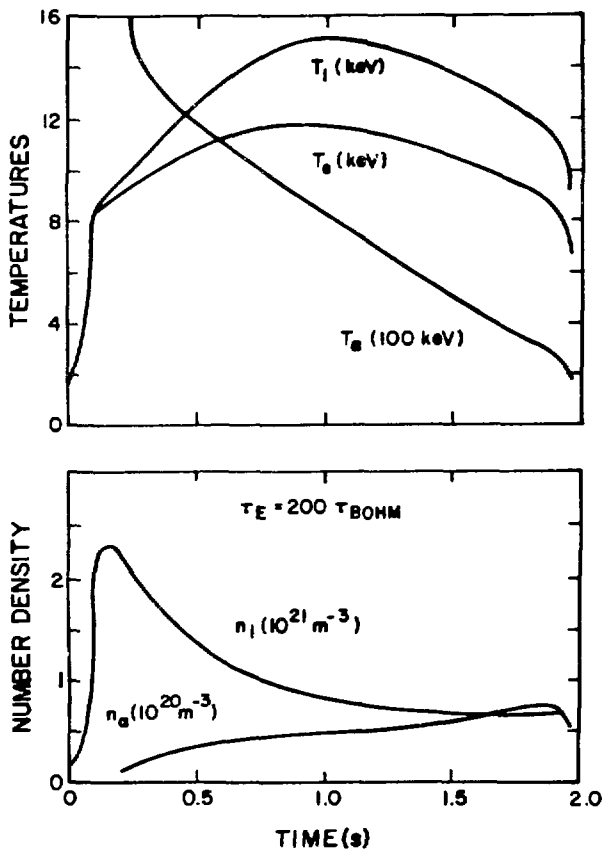

Fig. V-5. Ion, electron and alpha-particle temperatures and densities for the $\tau_E = 200\ \tau_{BOHM}$ case.

(Appendix D). A thermally stable burn results at a nearly optimal ion temperature of $T_i \simeq 10\text{-}14$ keV, achieving a fuel burnup of $f_B \sim 0.17$ in $\tau_B = 1.96$ s. The burn is ultimately terminated as reactivity reduction, alpha-particle buildup and plasmoid expansion result in losses that overcome alpha-particle heating. The plasmoid trajectory versus reactor length, L, is schematically shown in Fig. V-6 for the post-formation, plasma burn and quench phases. The flare required in the conducting shell to overcome translational drag (Appendix E) within the reactor burn section is illustrated in both an actual scale model (top) and on an exaggerated scale (bottom) which better illustrates radial variations. The first-wall radius, r_w, varies only from 1.20-m to 1.64-m over a total burn section length of 40-m using a conducting shell thickness of $\delta = 0.05$-m. The actual velocity versus burn section length is shown in Fig. V-7 for the $\tau_E = 200\ \tau_{BOHM}$ case. Requiring the first-wall neutron loading to be uniform forces the plasmoid velocity to decrease from 38 m/s at the inlet to 10 m/s at the outlet, where the ratio, r_v, of actual velocity to minimum allowed velocity (ℓ/τ_s) is also plotted. The reactor length traversed, as defined at the trailing edge of the FRC, by the plasmoid is also given in Fig. V-7.

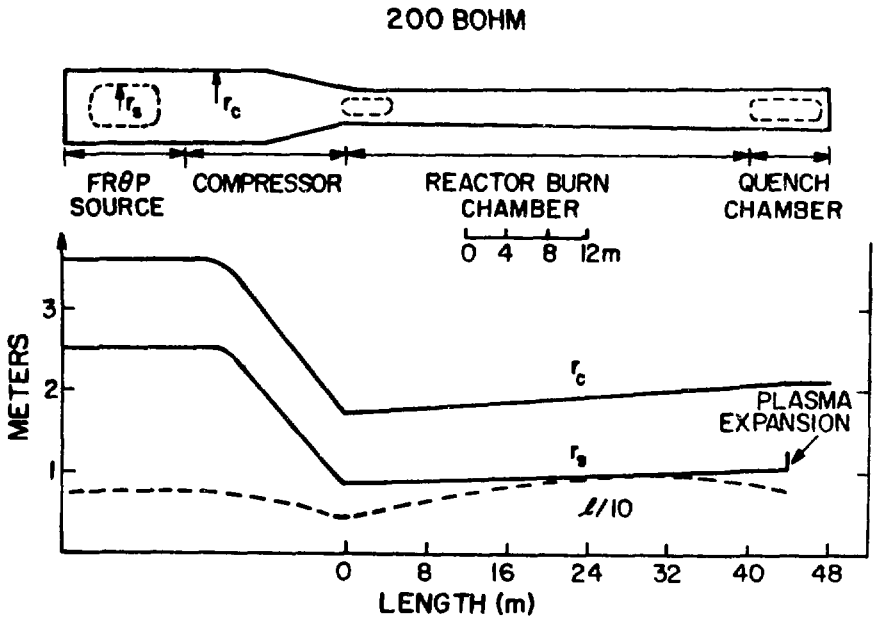

Fig. V-6. Sample case using $200\tau_{BOHM}$ energy confinement time showing variations in FRC plasmoid dimensions (r_s, ℓ) versus reactor length in the FRθP, compressor, burn section and quench chamber.

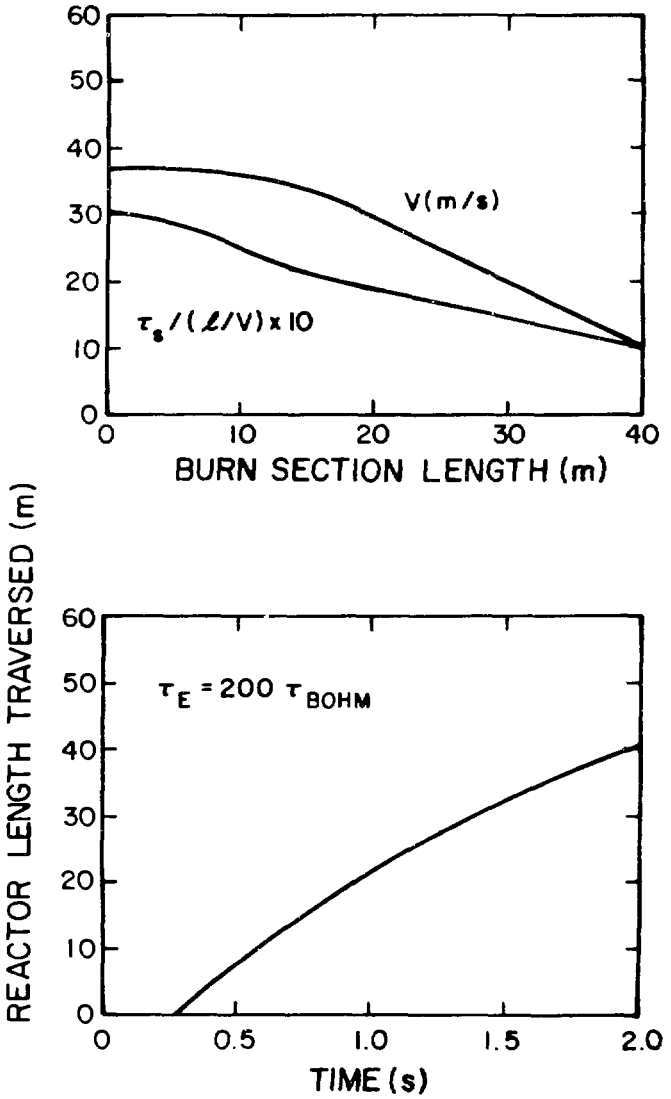

Fig. V-7. Plasmoid velocity as a function of reactor length and reactor-length traversed as a function of time for the $200\tau_{BOHM}$ case in Figs. V-5 and V-6.

A comparison between the sample numerical solution and the analytic results (Sec. V.A.) for constant-f_ℓ case is given in Table V-IV. The first-wall neutron loading is fixed at 2 MW/m^2 in both cases with the slightly higher thermal power for the numerical calculation attributed to a slightly larger reactor bore because of the burn-section flaring. Using a numerical simulation with r_{vo} = 3.0 (inlet velocity/(ℓ/τ_s)) predicts a reactor that is remarkably similar to that deduced by the analytical calculation. The higher

TABLE V-IV

COMPARISON OF ANALYTICAL (f_ℓ = CONSTANT) AND NUMERICAL CASES FOR $\tau_E = 200\tau_{BOHM}$ AND $r_{vo} = 3.0$

	ANALYTICAL	NUMERICAL (INLET/OUTLET)
Total thermal power, P_{TH}(MWt)	880	1060
Burn chamber length, L(m)	42	40
Separatrix radius, r_s(m)	0.83	0.85/1.05
Plasmoid length, ℓ(m)	5.8	5.0/8.0
First-wall radius, r_w(m)	1.2	1.2/1.64
Conducting-shell radius, r_c(m)	1.7	1.7/2.1
Conducting-shell skin time, τ_s(s)	0.6	0.48/0.8
Burn time, τ_B(s)	4.5	2.0
Injection time, τ_I(s)	6.2	5.8
Translational velocity, v(m/s)	9.4	30/10
Plasma density, n(10^{21}/m^3)	1.1	2.5/0.5
		2.0 (10 keV)
Plasma temperature, T(keV)[a]	10	8.5/9.0
Lawson parameter, $n\tau_B$(10^{21}s/m^3)	5.0	2.1
Burnup, f_B	0.22	0.17
Duty factor, f_ℓ	0.1	0.08/0.14
Compressed field, B_i(T)	3.0	4.2/2.0
Vacuum field, B_o(T)	2.3	3.1/1.5
FIXED PARAMETERS		
Blanket thickness, Δb(m)	0.5	0.5
Fusion neutron wall loading, I_w(MW/m^2)	2.0	2.0
Shell thickness, δ(m)	0.05	0.05[b]
Equilibrium/Stability constraints		
• x_s	0.5	0.5
• ℓ/r_s	7	6.0/7.3

[a]Plasma temperature is 12-14 keV during a major part of numerical simulation (Fig. V-5).

[b]The conductor fraction of 0.7 reduces the actual copper thickness to 0.035 m.

plasmoid velocity required in the numerical solution dictates a somewhat longer reactor, although a more energetic burn ($T_i \sim 12$–16 keV) shortens the burn time from 4.5 s (analytic) to 2.0 s (numerical) the resultant burn chamber length, consequently, is approximately the same for both cases.

A direct comparison between the numerical solution and Eq. (V-4) for the minimum power constraint, as calculated analytically, (Sec. V.A.) is made difficult because of the poor correlation between $n\tau_B$ and plasmoid energy yield. This comparison difficulty can be alleviated by recognizing that

$$n_o \tau_B = \frac{2f_B}{(1-f_B)\langle\sigma v\rangle} \quad , \tag{V-9}$$

for constant temperature. Equation (V-4) then becomes

$$P_{TH} = 9.9(10)^5 \; I_w^{1/2} \; \Delta b^{3/2} \; f_\ell^{1/2} \; f_B/(1-f_B)\delta \quad , \tag{V-10}$$

which gives both the minimum power in terms of the fractional burnup, f_B, and is a better indication of plasma yield than the parameter $n\tau_B$. Evaluating this expression for the values listed in Table V-I for the numerical solution ($I_w = 2(10)^6$ W/m^2, $\Delta b = 0.5$ m, $f_\ell = 0.1$, $f_B = 0.17$ and $\delta = 0.035$ m) gives $P_{TH} = 920$ MWt; when adjusted for increased average first wall-radius (1.2 m for the analytic case and 1.4 m numerical case) $P_{TH} = 1070$ MWt, which is nearly identical to the value actually achieved. This agreement is in part fortuitous because of the choice of $r_{vo} = 3.0$ which yields a reactor length that matches the value predicted by the analytic model for a minimum power using the approximation that $v = \ell/\tau_s$ is a constant.

In either case a minimum reactor length is required to achieve an adequate plasma burn and energy balance. The analytic model automatically imposes the minimum length condition by defining the plasmoid velocity to be the lowest achievable value ($v = \ell/\tau_s$), as defined by the condition for magnetic flux loss from the region between r_s and r_w. The numerical solution requires the plasmoid velocity to be greater than ℓ/τ_s at the inlet, allowing the FRC plasmoid to expand and reducing the velocity maintains a uniform

first-wall neutron loading. This reduction in FRC velocity continues until the velocity is reduced to ℓ/τ_s, and a quench is allowed to occur. A parametric evaluation of design points for r_v = 2-5 is shown in Fig. V-8 in terms of Q_E versus burn section length and a range of plasma densities. The plasma density is defined at the burn section inlet for a temperature of 10 keV. The desire for a thermally stable plasma burn (Fig. V-5) dictates the total reactor length as losses quench the burn and translational power (i.e., alpha-particle power) is diminished. For a given plasma density the resultant Q_E is then relatively insensitive to variations in burn-section length. A decrease in Q_E does occur at short lengths (~ 10 m for r_{vo} = 1) because of

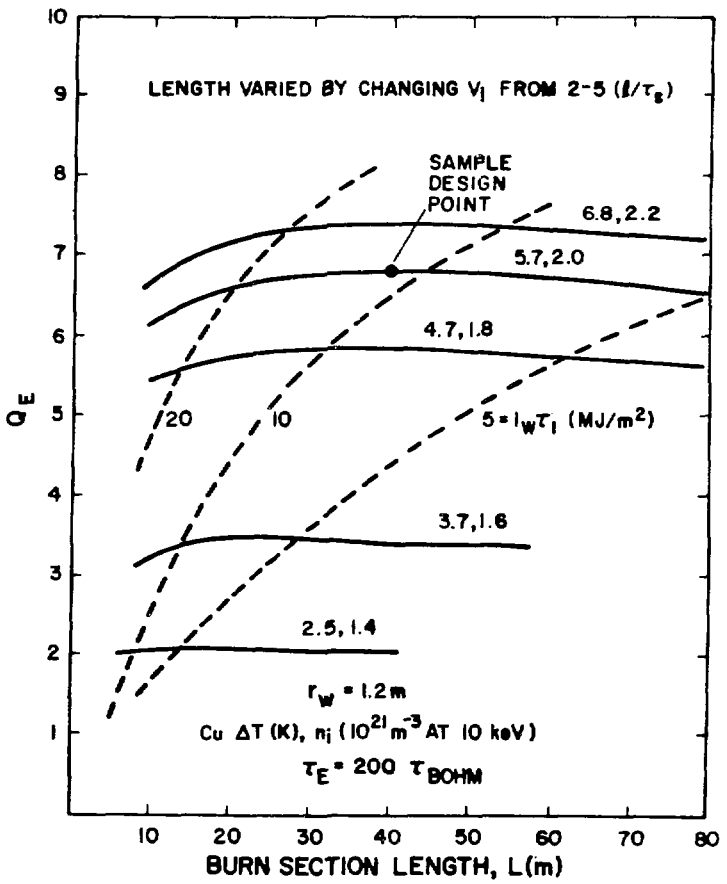

Fig. V-8. A parametric evaluation of design points for v_i = 2-5 for a range of plasma densities. The value for the first-wall temperature rise (at the inlet) ΔT, is the maximum temperature drop (at burn chamber inlet) across 1 mm of water-cooled copper placed at the first wall.

reduced burn times, which prematurely terminate the burn cycle, and at long lengths (~ 80 m for r_{vo} = 5 at n_i = 1(10)^{21}, Fig. V-8) because of increased plasmoid expansion and lower fusion yield in the long burn chamber. The point design given in Table V-IV occurs near the maximum Q_E value, although the weak dependence of Q_E versus L allow an optimum length for this scaling to be chosen on the basis of economics arguments that have yet to be quantified by this study.

Also shown in Fig. V-8 are dotted lines of neutron energy per square meter of first wall, $I_w\tau_I$ (MJ/m^2). A given burn simulation follows the trajectory of a single plasmoid and calculates the first-wall energy density along with all other energy quantities necessary to define a reactor energy balance. The first-wall loading or reactor power need not be defined until an injection time, τ_I, is chosen. As expected, for a given first-wall loading the injection time must decrease as the length, L, increases; more FRC plasmoids are required to supply the power in a larger device.

As shown above, a comparison of the numerical results with the analytic solution requires a judicious choice of r_{vo} = 3.0 to give an equivalent reactor length. Using this parameter, a spectrum of design points is generated for Q_E versus first-wall radius (measured at the inlet of the burn section). These design points are shown in Fig. V-9 for a range of (initial) plasma densities. Contour lines of constant burn-section length are also given in Fig. V-9. Along each iso-density curve a maximum reactor length occurs where the plasma burn optimally provides translational power (direct alpha-particle energy conversion via plasma expansion). The design point listed in Table V-IV is also shown in Fig. V-9 to lie along the optimum (maximum lengths), which generally corresponds to a nearly optimal, (thermally-stable) burn with T_i ~ 10-15 keV. Below this point, excessive losses lead to low-yield burns with a correspondingly low Q_E resulting. As the first-wall radius is increased beyond that required for maximum reactor length, a thermally unstable burn drives excessive FRC length expansion, increased translational drag and correspondingly shorter systems. At first glance, this region appears attractive because of the shorter reactor lengths achievable at somewhat higher values of Q_E. These higher Q_E values, however, result from excessive FRC length expansion, which produce more direct-conversion energy in the burn chamber, and not from higher thermonuclear yields. The physics implications of requiring large FRC length

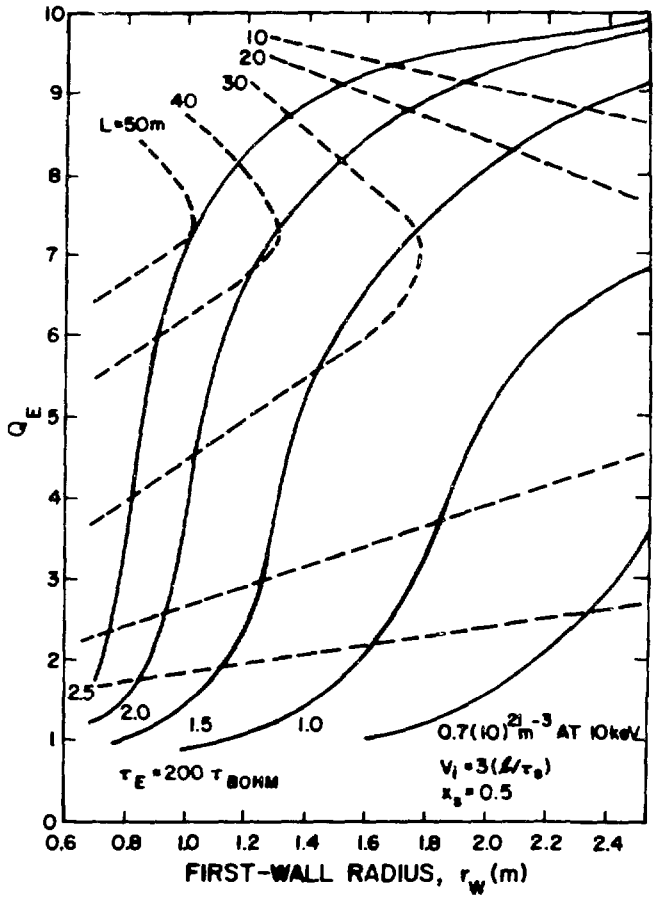

Fig. V-9. Q_E versus first-wall radius at the burn chamber inlet radius, r_w, for $200\ \tau_{BOHM}$ scaling, showing contours of constant plasma densities and reactor lengths, L.

expansions (2-4 times starting values) to achieve high Q_E values are questionable. The thermally stable burns are expected to produce more realistic reactor system.

Minimizing the size of the energy source (i.e., capacitive energy store) required for plasma initiation is highly desirable because of the anticipated complexity of the FRθP source. This energy is expected to scale as

$$E_S \propto r_w^2\, \ell\, n \propto r_w^3\, n \quad . \tag{V-11}$$

The dependencies associated with varying Q_E along constant Q_E, r_w, and n trajectories are illustrated in Fig. V-10. The tendency is to operate at an

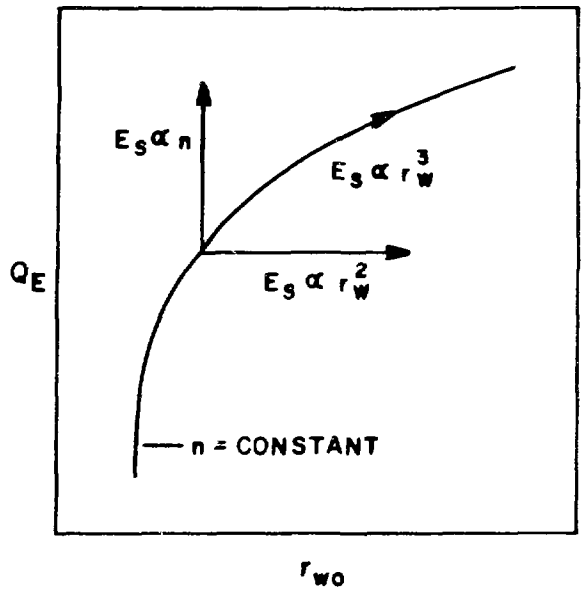

Fig. V-10. This curve used in conjunction with Fig. V-9 illustrates the variation in required FROP source energy, E_s, along various trajectories in the parameter space indicated.

(economically) adequate Q_E at the lowest possible value of r_w. As shown by the analytic model (Fig. V-1), however, the total thermal power increases rapidly if the radius is decreased below r_w = 1.2 m. A comparison between the analytic model (Fig. V-1) and numerical case (Fig. V-9), where Q_E = 7 and I_w = 2.0 MW/m^2, results in good agreement between the analytic and numerical results as shown in Fig. V-11, indicating that a minimum first-wall radius of r_w = 1.2 m should be used for the τ_E = 200 τ_{BOHM} case, as determined by the analytic model.

Using the same Q_E versus r_w radius curves as is given in Fig. V-9, overlay plots of burn time, τ_B, neutron energy per square meter of first wall, $I_w\tau_I$, and maximum first-wall temperature gradient (across 1-mm-thick copper at burn section inlet), ΔT, are shown in Figs. V-12 through V-14. The burn time exhibits little variation over the wide range of radii and plasma densities. The first-wall neutron loading may be specified from Fig. V-13 by choosing the plasmoid injection time, τ_I. The plot of temperature rises at the inlet, ΔT, in Fig. V-14 assumes a 1-mm-thick water-cooled copper surface with the maximum value of ΔT occurring at the burn section inlet. In order to maintain Q_E as

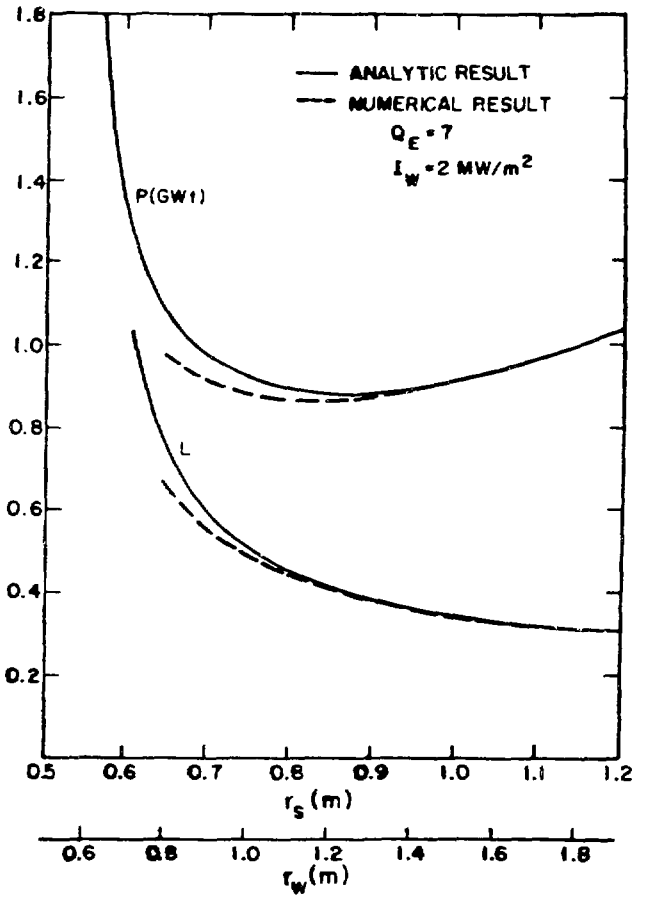

Fig. V-11. Comparison of analytical and numerical predictions of P_{TH} and reactor length, L. The inlet first-wall radius, r_w, is used to calculate P_{TH} in the numerical case which gives the good agreement with the analytic predictions (Sec. V.A.).

the radius is lowered requires higher densities and correspondingly higher temperature excursions (i.e., $\Delta T \sim r_w^{-2.5}$).

C. Investigation of Plasma Transport Scalings

A number of transport scalings were used to evaluate parametrically the CTOR performance. These scalings investigated included classical, Bohm-like, Alcator and lower-hybrid drift (Appendix D).

Figure V-15 shows Q_E versus the first-wall radius at the entrance of the burn chamber, r_{wi}, for energy confinement time scalings ranging from classical to 50 $_{BOHM}$ times ($\tau_{BOHM} = a^2B/62T_e$) at a plasma density of $n_i = 1(10)^{21}$ m^{-3} and a temperature of 10 keV. The initial plasmoid velocity is $3(\ell/\tau_s)$ at the

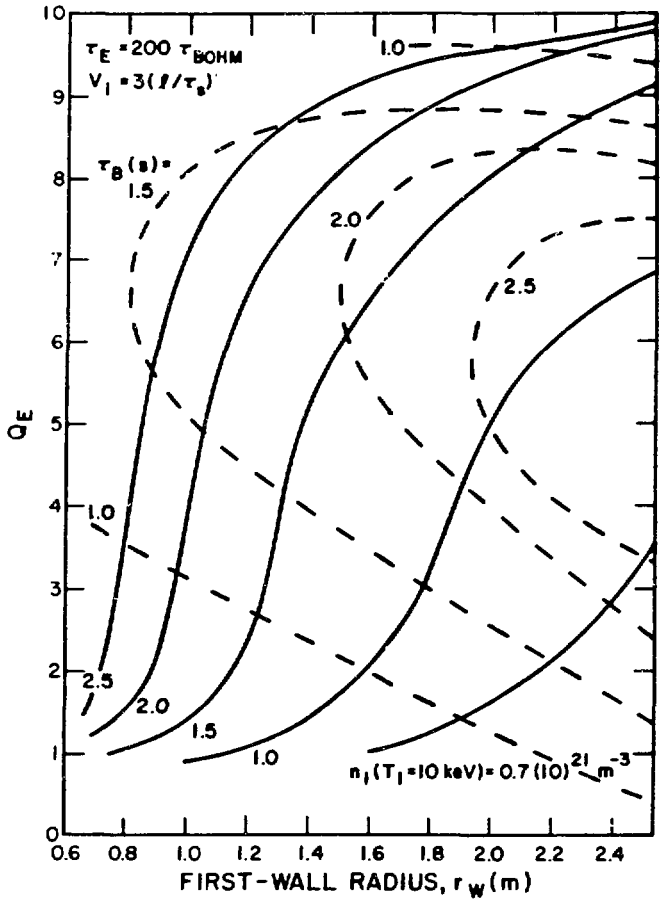

Fig. V-12. Q_E versus first-wall radius at the burn-chamber inlet, r_w, for 200 τ_{BOHM} scalng, showing contours of various plasma densities and plasmoid burn times, τ_B.

entrance of the burn chamber. In each case Q_E increases rapidly as r_{wi} increases leading to enhanced plasma energy confinement. A more energetic plasma burn drives the plasmoid along the plasma burn chamber by direct conversion of alpha-particle (plasmoid expansion) energy to translational motion. Further increases in r_w induces thermal runaway and the plasma overheats (30-50 keV), resulting in excessive plasmoid axial expansion, increased conducting shell losses (increased drag) and reductions in plasma power density; a saturation and eventual reduction in Q_E results.

The effects of varying the initial plasmoid velocity are shown in Fig. V-16 for a first-wall radius r_{wi} = 1.2 m and a range of assumed plasma densities. Both Alcator ($\tau_E \sim 3(10)^{21}$ na^2) and 200 τ_{BOHM} scalings, which have the same functional dependence for a high-beta plasma confined at a constant

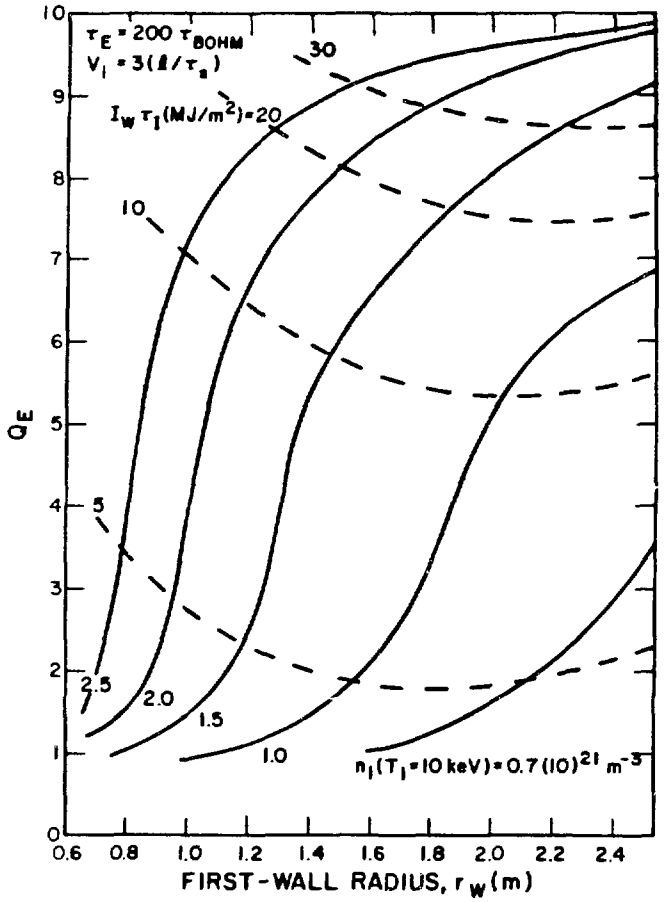

Fig. V-13. Q_E versus first-wall radius at the burn-chamber inlet, r_w, for 200 τ_{BOHM} scaling showing contours of various plasma densities and neutron energy (14.1-MeV) per square meter of first wall, $I_w\tau_I$.

magnetic field, yield thermally-stable burns. For these burns the reactor length is dictated by plasma self-quench, resulting in a loss of translational power capabilities (i.e., diminished alpha-particle power). The resultant Q_E is relatively insensitive to length and the initial plasmoid velocity, v_i. This behavior is not observed if classical scaling is used; the plasma temperature rises uncontrollably and longer reactor lengths allow increasingly greater plasma expansion (primarily in length, ℓ) and direct-conversion work. Figure V-15, therefore, is generally valid in the range $v_i \geq 2(\ell/\tau_s)$ and $L \geq 10$ m for the values of Q_E corresponding to thermal stable burns (i.e., Q_E values near or below the inflection points).

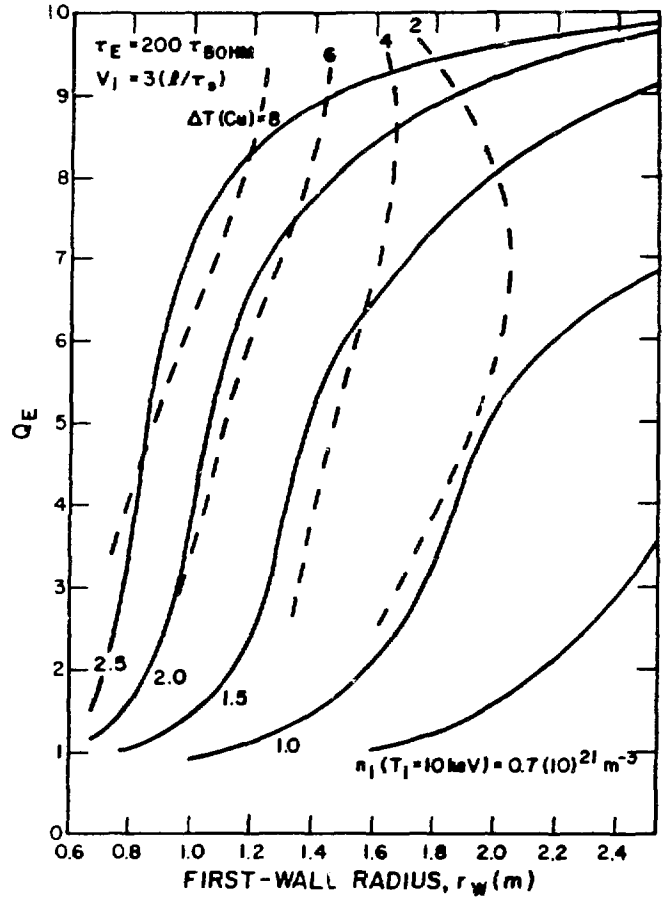

Fig. V-14. Q_E versus first-wall radius at the burn-chamber inlet, r_w, for 200 τ_{BOHM} scaling showing contours of various plasma densities and maximum first-wall temperature gradients (across 1-mm thick copper at burn section inlet), ΔT.

Using the minimum-power relationships derived from the analytic CTOR scaling and summarized in Fig. V-2 (the function f(y) drives the P_{TH} variation using $y = 0.6(1-x_s)$ to calculate x_s, re: Sec. V.A.), the relative thermal power and required FRθP energy, E_s, is shown in Fig. V-17 as a function of the BOHM multiplier. The value of r_w used to calculate x_s ($y = 0.6(1-x_s)$) is taken from Fig. V-15 for $Q_E = 7$ in order to generate Fig. V-17 for this minimum power condition. The required value of P_{TH} and E_s are normalized to 1 for the $200\tau_{BOHM}$ design point. As shown in Sec. V.B., increasing $\delta/\Delta b$ from 0.10 to 0.25 decreases P_{TH} by ~ 2, and lowering r_{vo} from 3 to 2 will further reduce the power (i.e., reactor length) by another factor of two from the value adopted as the design value. These reductions would lower the

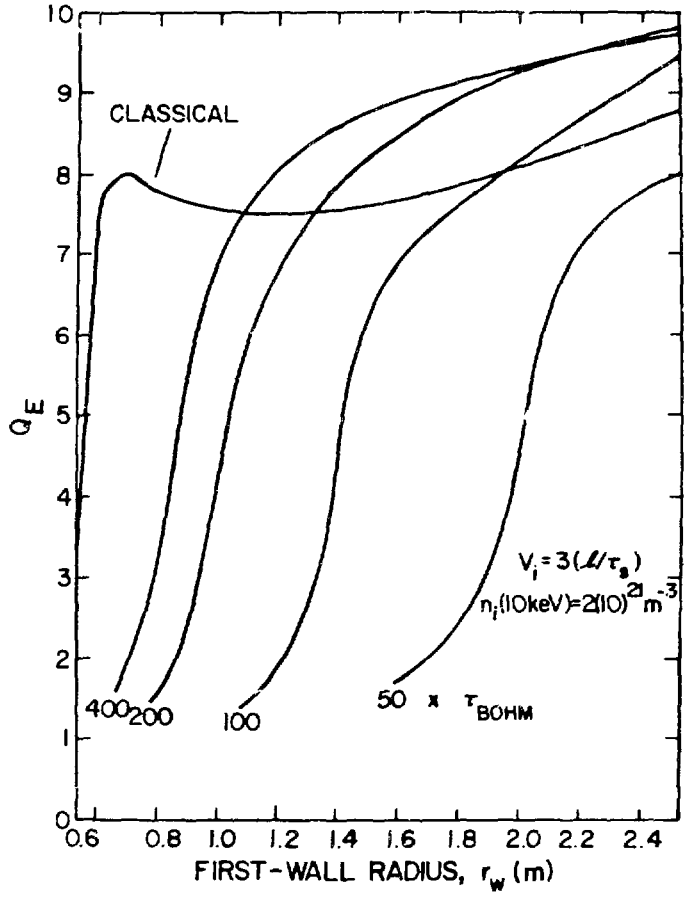

Fig. V-15. Engineering Q-value, Q_E, versus first-wall radius at the burn chamber inlet radius, r_w, for classical and a range of BOHM scalings.

design-point length to only 10-m, which may not represent an economic system (i.e., total power may be too low). As shown in Fig. V-16, the design point corresponding to $200\tau_{BOHM}$ (shown by asterisk) also corresponds to Alcator scaling and is near the minimum thermal power and source size (Fig. V-17). This operating point also achieves a near optimum burn, as is shown in Fig. V-5.

Finally, a scaling relationship based upon the lower-hybrid drift instability (Appendix D) was used to model plasma losses. This scaling is strongly dependent on plasma gradient lengths which tend to be quite sharp for $x_s \lesssim 0.6$ (Appendix A). This behavior, if true, requires operation at larger values of x_s, and, correspondingly, larger values of separatrix radius, r_s,

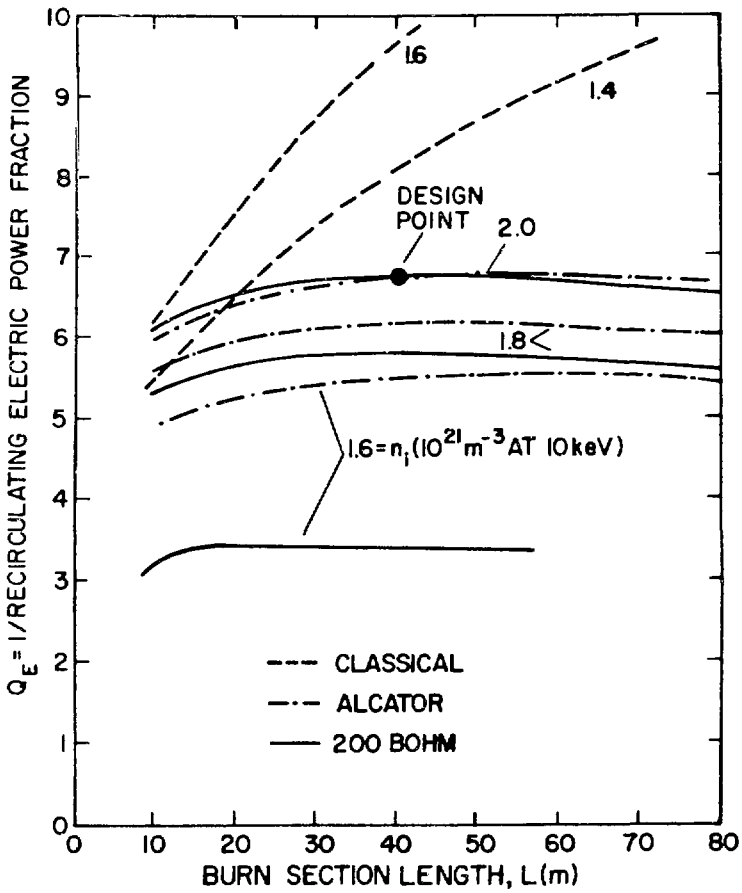

Fig. V-16. Q_E versus reactor length L, achieved using $v_i = 2\text{-}5(\ell/\tau_s)$ for classical, Alcator, and 200 τ_{BOHM} scalings and a range of plasma densities.

are needed to minimize the predicted particle losses, particularly for alpha particles.

A direct comparison between the numerical calculation and the analytical solution for $x_s = 0.75$ is made using the lower-hybrid drift scaling. The resultant numerical solution has $Q_E = 6.7$ at $n_i = 1(10)^{21}$ m^{-3} at 10 keV with the time-dependent dimensional changes shown in Fig. V-18. Once again the agreement is very good for $r_{vo} = 3.0$, as is shown in Table V-V; only the injection time, τ_I, and the value of f_ℓ do not show agreement. The numerical solution uses nearly twice as much plasma as the analytic case requiring τ_I to be increased to maintain the first-wall neutron wall loading, I_w.

TABLE V-V

COMPARISON OF ANALYTICAL (f_ℓ = CONSTANT) AND NUMERICAL CASE FOR LOWER-HYBRID DRIFT TRANSPORT SCALING, r_{vo} = 3.0 and x_s = 0.75

	ANALYTICAL	NUMERICAL (INLET/OUTLET)
Total thermal power, P_{TH}(MWt)	2400	2600
Burn chamber length, L(m)	53	53
Separatrix radius, r_s(m)	2.25	2.25/2.7
Plasmoid length, ℓ(m)	10.5	8.5/7.1
First-wall radius, r_w(m)	2.55	2.55/3.05
Conducting shell radius, r_c(m)	3.0	3.0/3.5
Conducting-shell skin time, τ_s(s)	1.51	1.0/1.5
Burn time, τ_B(s)	7.6	1.9
Injection time, τ_I(s)	15.1	30
Translational velocity, v(m/s)	6.9	25/7
Plasma density, n(10^{21}/m^3)	0.66	4.5/0.6
		2.1 (10 keV)
Plasma temperature, T(keV)[a]	10	5.5/9.0
Lawson parameter, $n\tau_B$(10^{21}s/m^3)	5.0	2.4
Burnup, f_B	0.22	0.14
Duty factor, f_ℓ	0.1	0.033/0.05
Compressed field, B_i(T)	1.3	4.4/3.2
Vacuum field, B_o(T)	0.57	2.0/1.5
FIXED PARAMETERS		
Blanket thickness, Δb(m)	0.4	0.4
Fusion neutron wall loading, I_w(W/m^2)	2.0	2.0
Shell thickness, δ(m)	0.1	0.1
Physics		
• x_s	0.75	0.75
• ℓ/r_s	3.5	

[a]Plasma temperature 10-15 keV during bulk of numerical simulation.

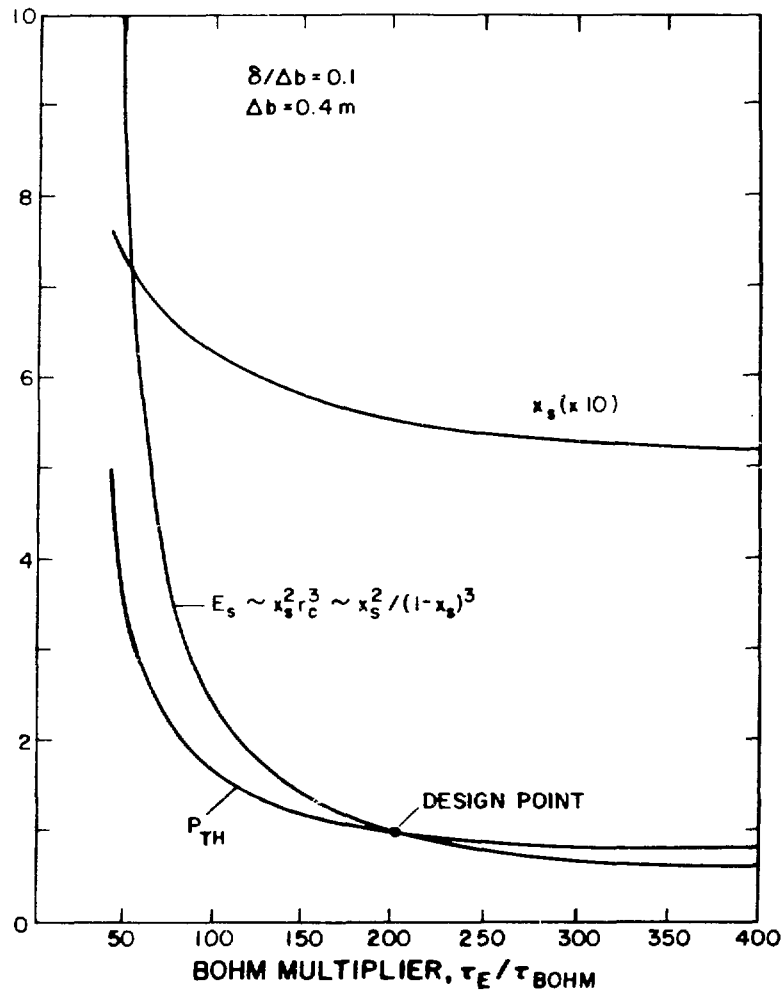

Fig. V-17. Relative thermal power, P_{TH}, and plasma source (FRθP) size, E_s, for various confinement times normalized to the design point value. The minimum-power constraint is imposed.

Although the lower-hybrid drift scaling is radically different from the Bohm-like or Alcator relationships, the resulting reactor system appears quite similar in both cases. The lower-hybrid drift case requires the total power be increased to 2400 MWt and the reactor length increases to 53-m long. The length could be reduced for smaller values of r_{vo} with a corresponding reduction in total power. The reactor system size is only moderately increased although the FRΘP source size must be increased by a factor of ~ 4.

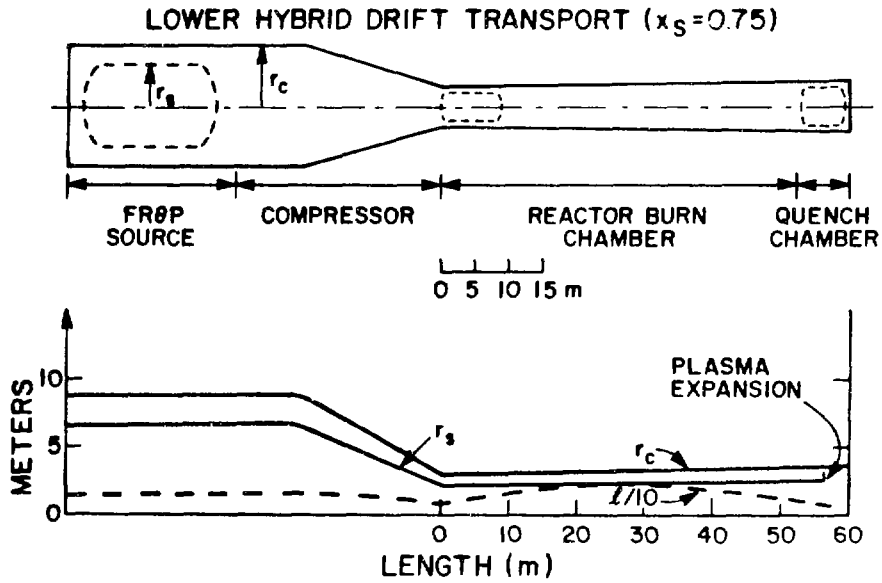

Fig. V-18. Plasmoid trajectory using lower-hybrid drift transport (Appendix D).

VI. POINT-DESIGN PARAMETERS

A. Physics Parameters

The CTOR design point is based on a 200 Bohm confinement time which also yields the same result as Alcator scaling. These scalings produce attractive reactor designs at relatively lower thermal power and small required source size (Sec. V, Fig. V-17). The physics parameters for this design are summarized in Table VI-I.

B. Engineering Parameters

The reactor energy flow is listed in Table VI-II, from which the recirculating power, (Sec. IV.B) is computed. These energy flows are also displayed on the energy flow diagram in Fig. IV-2. The system power is specified by choosing the injection time, τ_I. Taking τ_I = 5.8 s to give a 14.1-Mev neutron wall loading of 2 MW/m^2, a thermal output of 1050 MWt results with a net electric power of 310 MWe for Q_E = 6.8 and η_{TH} = 0.35. Table VI-III summarizes key engineering parameters for the CTOR design point.

TABLE VI-I

PHYSICS PARAMETERS FOR CTOR DESIGN POINT

PARAMETER	VALUE (INLET/OUTLET)
Separatrix radius, r_s(m)	0.85/1.05
Plasmoid length, ℓ(m)	5.0/8.0
Conducting-shell radius, r_c(m)	1.7/2.1
Shell skin time, τ_s(s)	0.48/0.8
Burn time, τ_B(s)	1.95
Energy confinement time, τ_E(s)	0.1
Plasmoid translational velocity, v(m/s)	30/10
Plasma density, n_i ($10^{21}/m^3$)	2.5/0.5
Plasma temperature, T_i(keV)	~ 15
Ion-gyroradii contained in column, R/ρ_{io}[(a)]	170
Ion-gyroradii in minor radius, $S = a/\rho_i$[(b)]	30
Beta, $\beta_s = 1 - 0.5\ x_s^2$	0.87
Separatrix ratio, $x_s = r_s/r_c$	0.5
Burnup, f_B	0.17
Lawson parameter, $n\tau_B$(10^{20} s/m^3)	21.0

(a)Value of ρ_{io} calculated using vacuum field.

(b)Value of ρ_i uses one-half vacuum field value. Actual sheath width expected to be 0.33 of this value (see Appendix A).

C. Design Point Sensitivities

As shown in Sec. V.C., a wide range of transport scalings may be used in modeling CTOR performance that achieve similar values of Q_E. For example, only moderate increases in reactor size (a factor of ~ 4 in thermal power to a few gigawatts) occur over the range of classical to 50 Bohm (characteristic of lower-hybrid drift scaling, Appendix D). Increased losses are supplied by increasing the power density ($\propto n_i^2$). This capability results in a reactor device that is remarkably invariant to plasma transport as the plasma density and plasmoid injection time are adjustable to give a desired wall loading.

The design sensitivity to energy transfer efficiencies is shown in Fig. VI-1. Transfer efficiencies of $\eta_{ETS} = 0.8$ are used in the CTOR design, as detailed in Sec. VII.B.2. The efficient use of magnetic energy by the CTOR

TABLE VI-II

ENERGY INVENTORY FOR CTOR

DESIGN POINT[a]

PARAMETER	VALUE (MJ)
Initial plasma, W_{INT}^{o}	16.4
Final plasma, W_{INT}	81.7
Neutron (16.5 MeV/n), W_N	5090.
Alpha particle, W_α	1090.
Direct conversion, W_{DC}	32.6
Bremsstrahlung, W_{BR}	9.1
Thermal conduction, W_{COND}	897.
Trapped poloidal flux (quench)	7.0
Quench	88.8
Total thermal, W_{TH}	6170.
Conducting shell transport losses[b]	46.3
Auxiliary, W_{AUX}	151.
ETS losses (η_{ETS} = 0.8), W_{ETS}	80.
FROP source bank, W_{BANK}	61.8
Homopolar compressor, W_{COMP}	175.
Homopolar recharge at quench, W_{EXP}	70.
Gross electric, W_{ET} (η_{TH} = 0.35)	2160.
Circulating electric, W_C	318.
Net electric, W_E	1840.

[a]Refer to CTOR energy balance, Fig. IV-2.

[b]Provided by alpha-particles expansion of the FRC plasmoid

is illustrated in Fig. VI-1 where the recirculating power fraction varies only between 12 and 20% for transfer efficiencies of 1.0 and 0.5, respectively.

VII. ENGINEERING CONSIDERATIONS

A. Preliminary Plant Layout

Although the parameters given in Secs. VI and VII.B. are sufficiently extensive to begin a conceptual engineering design of the CTOR power plant, this aspect of the study has not been emphasized, being beyond the context of

TABLE VI-III

CTOR ENGINEERING PARAMETERS

PARAMETER	VALUE (INLET/OUTLET)
Burn section first/wall radius, r_w(m)	1.2/1.6
Burn section length, L(m)	40
Superconducting coil field, B_s(T)	3.1/1.5
Required FROP energy, W_{BANK}(MJ)	62
Required compressor section energy, W_{COMP}(MJ)	175
Burn time, τ_B(s)	2.0
Injection time, τ_I(s)	5.8
First-wall loading, I_W(MW/m^2)	2.0
Engineering Q-value, Q_E	6.8
Recirculating power fraction, ε	0.15
Total thermal power, P_{TH} (MWt)	1050
Gross electric, P_{ET}(MWe)	365
Recirculating power, P_c(MWe)	55
Net electric power, P_E(MWe)	310
Thermal conversion efficiency, η_{TH}	0.35
Plant efficiency, $\eta_p = \eta_{TH}(1-\varepsilon)$	0.30

this Level II study. Nevertheless, a preliminary plant layout has been made and is shown in Fig. VII-1. Future engineering studies will focus on the mechanical and electrical design of the FROP source and the compressional heater, rather than the relatively standard technology expected to be associated with the linear burn chamber.

For this 300-MWe CTOR plant, the plasma is formed in a FROP driven by a 62-MJ, 20-kV capacitor bank. The 175-MJ homopolar motor/generator powers the traveling-wave-network compressor which increases the plasma temperature from 1.5 to 8 keV at the inlet of the burn section. A 48-m long burn/quench section consists of 24 cylindrical 2-m-long modules with a solenoid superconducting coil located every 4 m (12 required). An energy dump is provided at both ends of the burn chamber to intercept the neutron streaming, with most of the alpha-particle energy retained by the plasmoid expected to exit the quench end of the device and to be extracted thermally. Flaring the

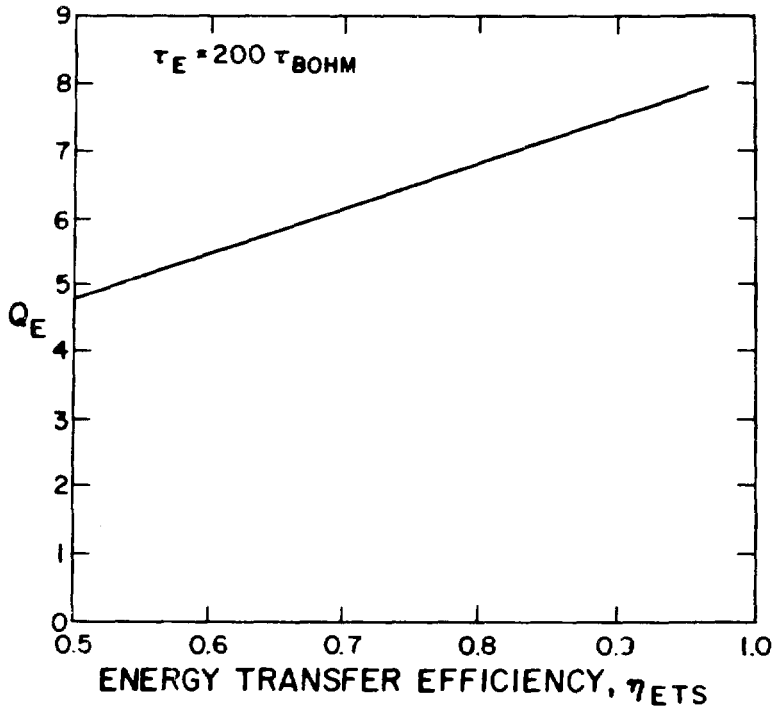

Fig. VI-1. Sensitivity of engineering Q-value, Q_E, on the efficiency of (homopolar) transfer/storage efficiency.

magnetic field at the exit end into a 4-m radius x 8-m long cylindrical beam dump (Sec. VII.B.3) provides 200 m^2 of heat transfer area.

The burn section could be similar to the nuclear island used in the Reverse-Field Pinch Reactor.[23] The 0.5-m-thick stainless steel blanket would contain a 40 v/o Li_2O packed bed into which penetrates radially oriented water steam cooled U-tubes. A low-pressure (0.1 MPa) helium purge gas is drifted through the granular Li_2O bed to extract tritium as an oxide. The slightly superheated (5-K) steam emerging from this blanket would be used to drive a turbogenerator. Despite the pulsed (plasma) nature of the burn, the inherent thermal capacity of this blanket results in less than a 5-K temperature excursion within the blanket structure, although a 1.0-mm-thick copper first-wall undergoes a bulk rise of 26 K (ΔT = 6 K across the material, leading to thermal stresses of 1.2 MPa at the inlet end of the burn chamber). A radiation shield, composed of a 0.1-m thick lead and a 1.4-m thick borated-water region protects the relatively low field (1.5-3.0 T) NbTi-Cu superconducting magnet coils (15 MA/m^2 average current density exclusive of support structure) from thermal loading and neutron/gamma-ray damage. Each of the 2-m

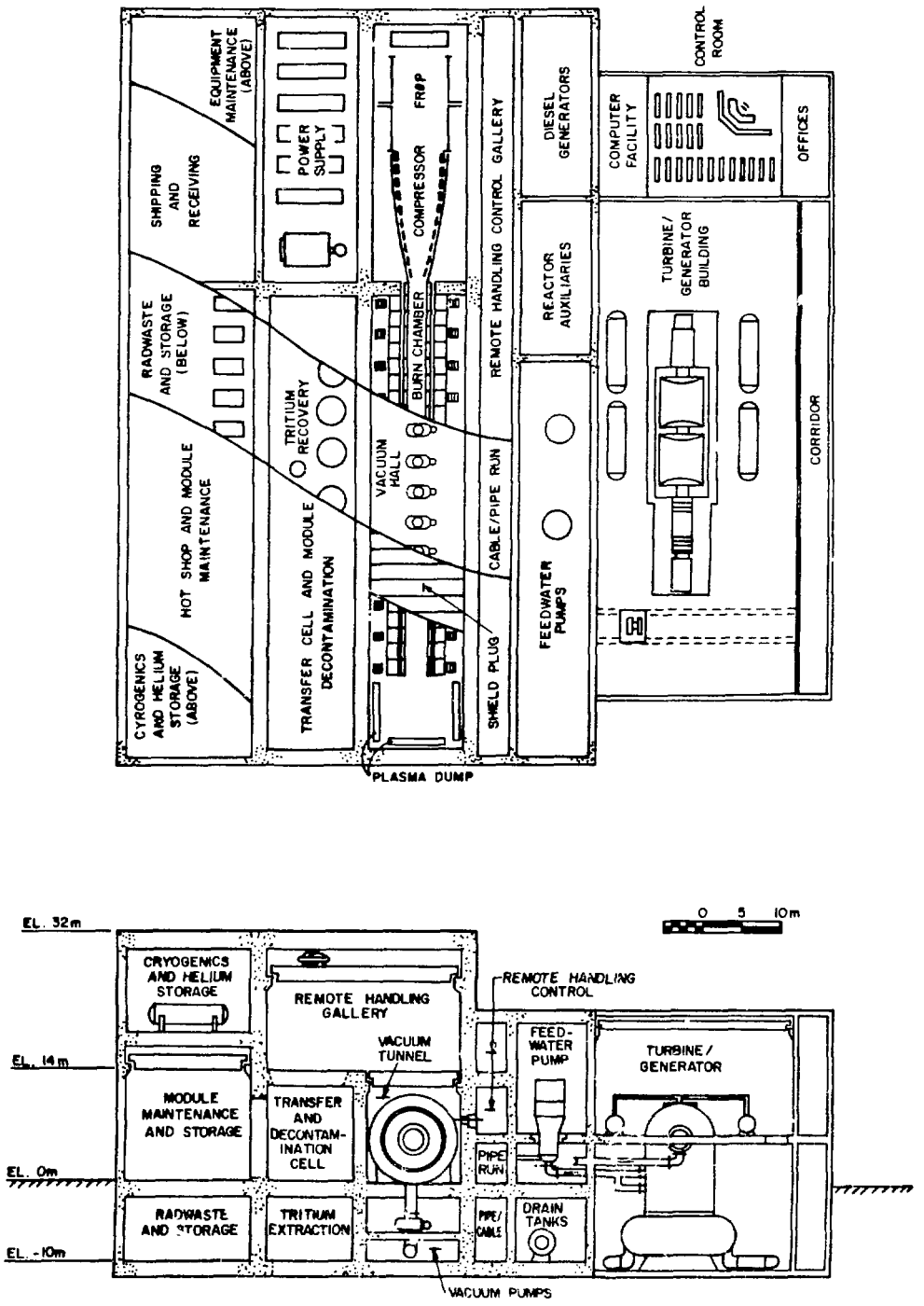

Fig. VII-1. Preliminary plant layout for CTOR.

long burn section modules would be electrically and thermohydraulically independent. The solenoidal field coils would be fixed structures that are adequately spaced to permit removal of the shield and blanket modules. The magnet coils and shield modules are of equal dimensions along the length of the burn section, while the elements of the first wall and blanket are made progressively larger (in a step-wise fashion) along the axial length to provide the modest taper required for alpha-particle-driven plasmoid expansion and translation.

Maintenance equipment for this system is also indicated in Fig. VII-1. The entire CTOR is located inside a vacuum tunnel which allows relatively easy access to the vacuum seals (shield plugs). Upon removal of three adjacent 2-m-long shield plugs, two solenoidal magnet coils are uncovered. The top-hemicylindrical half of the water shield would be removed between the fixed superconducting coils. Simple translating motions then allow the other two shield sections (located under the magnet coils) to be removed, uncovering three 2-m long first-wall/blanket modules. These modules are transferred to the adjacent decontamination cell and ultimately are moved into the hot cell facility.

B. Major Subsystems

1. Field-Reversed Theta-Pinch (FRΘP) Source. The implosion-heating phase is accomplished with a Marshall coil[28,32] (Appendix F). This fractional-turn coil allows lower terminal voltages and minimizes the technological requirements of the capacitor bank. Table VII-I lists important design parameters for this plasma source.

2. Compression Section. A tapered conducting shell in the compressor region of CTOR surrounds a traveling-wave coil network[33] that in turn is driven by a homopolar motor/generator.[32,35,36] The compressor section is modeled by numerical evaluation of an equivalent transmission-line electrical circuit shown in Fig. VII-2. The circuit consists of a number of basic circuit modules that can be electrically connected to simulate the overall compressor system. Referring to Fig. VII-2, the homopolar and compressor section are represented by setting R_1 and R_2 to a large and small value, respectively, with the compression region constructed of 25 series-connected circuit modules. The homopolar motor/generator is represented by a capacitive element that is connected directly to the first coil of the traveling wave network. For this simulation the network is terminated by shorting the last coil of the network to the ground potential.

TABLE VII-I

PARAMETERS OF FRΘP PLASMA SOURCE

PARAMETER	VALUE
Number of coils	2
Radius (m)	3.4
Length (m)	5 (each)
Capacitor energy, W_{BANK}(MJ)	62
Terminal voltage, V_o(kV)	20
Electric field, E_Θ(kV/cm)	0.95
Risetime, τ_R(μs)	47.0
Pre-implosion pressure, P_A(mTorr)	0.5
Post-implosion density, $n_o(10^{20}/m^3)$	1.4
Post-implosion temperature, T(keV)	1.5

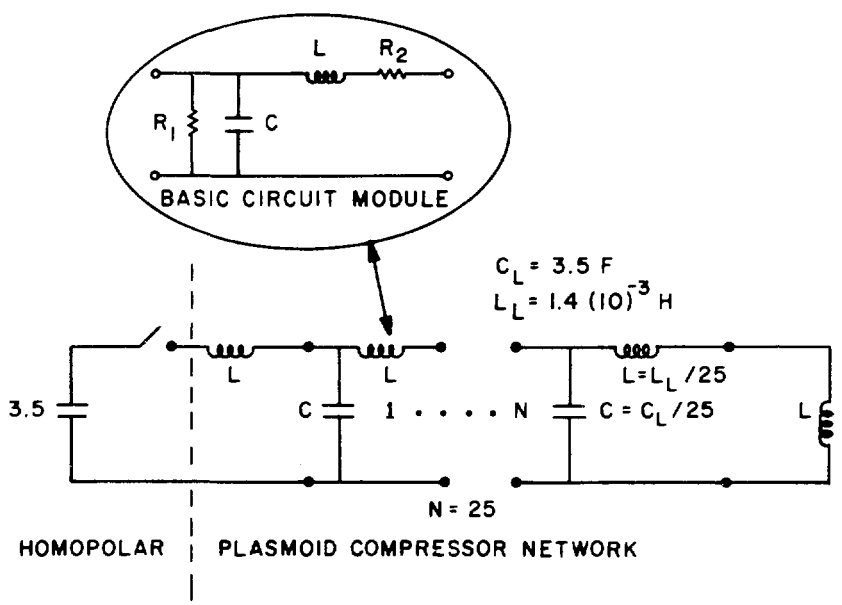

Fig. VII-2. Equivalent circuit of the traveling-wave network used to energize the plasmoid compression region.

The inductance of each compressor coil is given as

$$L = \mu_o \pi r^2 m^2 / \Delta \quad , \qquad \text{(VII-1)}$$

where r is the coil radius, m is the coil turns ratio and Δ is the axial distance between coils. For all calculations the coil turns ratio is taken as m = 1 in order to minimize the voltage requirements for the driving capacitance. The total flux linked by each coil is LI; requiring a constant flux over the length of the compressor implicitly forces the inductance of each coil to be equal. As noted from Eq. (VII-1), this condition implies that the ratio of the coil radius to the distance between coils must vary in a way that keeps r^2/Δ constant.

Specifying the energy to the compressor defines the homopolar energy to be 175 MJ for the reference reactor design, this energy in turn fixes the homopolar motor/generator capacitance, C_H, upon choosing the voltage, V_H. Taking a characteristic voltage[35,36] of 10 kV gives C_H = 3.5 F. An expected peak-load current of approximately 350 kA results if this current is discharged in 0.1 s. Taking the lumped parameter capacitance of the compressor to be equal to the homopolar capacitance, $C_H = C_L$, specifies the lumped inductance of the compressor at $L_L = 1.4(10)^{-3}$ H for a line "length" of 0.1 s ($\sim 2\sqrt{L_L C_L}$); this value has been verified by a computer simulation. The impedance of the compressor, Z_L, is given by $\sqrt{L_L/C_L} = 0.02\Omega$ with the load current given approximately as $V_H/Z_L \sim 0.5$ MA.

Subdividing the lumped electrical components into 25 discrete elements and requiring constant flux (r^2/Δ = CONSTANT) yields a compression section length of 16.2 m, as is shown in Fig. VII-3, where each magnet coil (0.1-m x 0.1-m in cross section) of inductance $L = 5.6(10)^{-5}$ H is displayed. Discrete capacitive elements, C = 0.14 F, are connected as shown in Fig. VII-2.

The time response of the plasmoid compressor is also shown in Fig. VII-3, using the equivalent circuit given in Fig. VII-2. After plasmoid initiation the CT is immediately translated from the Marshall coil in the compression chamber with the vacuum field being 0.41 T. Upon entering this region the homopolar motor/generator is switched into the traveling-wave network forcing flux connection to the bias field from the superconducting coil. The time-dependence of the resultant current ($B = \mu_o Im/\Delta$) pulse is shown in Fig. VII-3

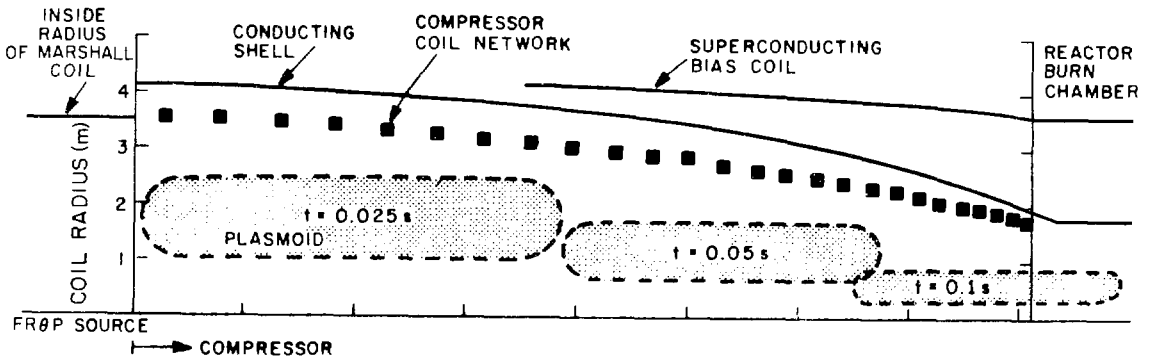

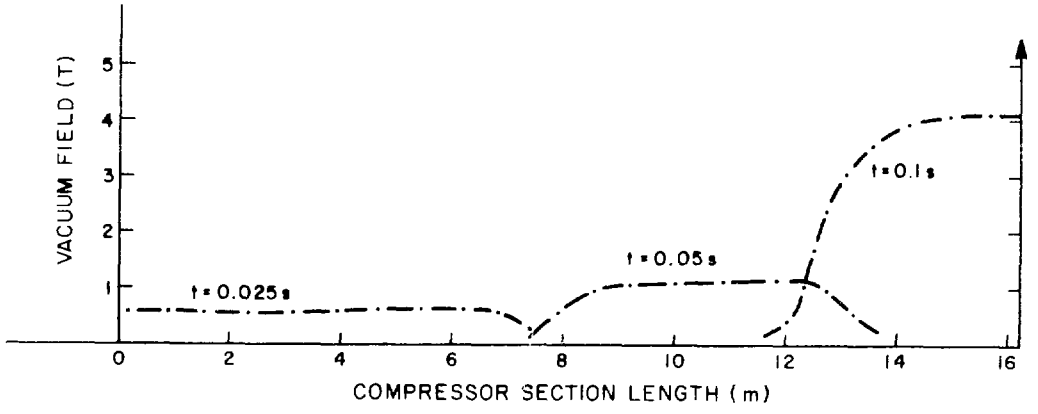

Fig. VII-3 Physical characteristics and time response of plasmoid compressions region showing the magnetic wave at times 0.025, 0.005, 0.105 and expected plasmoid behavior.

at three points in time during the pulse. After 0.1 s the plasmoid enters the burn section with the vacuum field near the required level of 4.2 T. At t = 0.1 s the energy contained in the magnetic field wave is 132 MJ with 9.9 MJ left in the homopolar motor/generator. The fraction of total energy transferred or retained in the driving element is then 0.81 of the pre-discharge energy stored. A value of η_{ETS} = 0.8 has been assumed for the reactor design and energy balance (Sec. VI).

Design characteristics for the compressor section and the driving element are listed in Table VII-II. As listed in Table VII-II the distributed capacitance in the traveling-wave network represents a sizable energy store that is equivalent to the driving capacitance. This requirement is estimated to be satisfied with 25, 7-MJ homopolar machines.

TABLE VII-II

PARAMETERS OF CTOR COMPRESSION REGION

PARAMETER	VALUE
Radius (tapered), r_c(m)	3.6/1.7
Length (m)	16.2
Coil geometry	
• Number	27
• Inductance (H)	$5.6(10)^{-5}$
• Cross section (m x m)	0.1 x 0.1
Distributed capacitance	
• Number	25
• Capacitance (F)	0.14
• Voltage (kV)	10
• Energy (MJ)	7
• Type	Homopolar motor/generator
Network power source	
• Number	1
• Capacitance (F)	3.5
• Voltage (kV)	10
• Energy (MJ)	175
• Type	Homopolar motor/generator

Not included in the above calculations are losses intrinsic to the homopolar motor/generator including[35,36] brush loss, bearing friction and drum Joule losses. Calculated energy transfer efficiencies for devices employing superconducting bias fields are found to be[35,36] in excess of 0.95 and, in fact, may reach 0.98-0.99 for the discharge times 30-100 ms envisaged by the CTOR design. The required energy (175 MJ) is used to charge/discharge the driving component and each compression coil capacitor (7 MJ) once for each plasmoid. For 0.95 efficient systems the energy loss is $\sim (0.95)^2 = 0.9$. This loss lowers the calculated transfer efficiency from 0.81 (Sec. VII.B.2) to $\simeq 0.73$, although the efficient use of energy in CTOR (Fig. VI-1) causes this lower value of η_{ETS} to increase the recirculating power fraction from 14.7% ($\eta_{ETS} = 0.8$) to only 15.6%. It is noted that this transfer efficiency is computed for an unoptimized compression section which may be capable of achieving $\eta_{ETS} = 0.8$ as assumed, by the design point, even when considering intrinsic homopolar losses.

3. Burn Chamber. Unlike other reactor systems in which the plasma source and burn chamber coincide, the CTOR burn section has considerably reduced technological requirements. The physical parameters of this passive burn chamber are listed in Table VII-III. Magnetic bias field levels of ~ 3.5 T are maintained by NbTi superconducting magnet coils. No active coil structures are present in the burn section. The blanket structure operates in a thermally steady state because of the large energy content of the blanket and the short time interval (~ 5 s) between the translating plasmoids. The 0.5-mm-thick stainless steel blanket would contain a 40 v/o Li_2O packed bed into which penetrates radially-oriented water/steam coolant tubes.[23] A low-pressure (0.1 MPa) helium purge gas is drifted through the granular Li_2O bed to extract tritium as an oxide.[23] The slightly superheated (5-K) steam emerging from this blanket would be used to drive a turbo-generator. Despite the pulsed nature of the plasma burn, the inherent thermal capacity of this blanket results in less than a 5-K temperature excursion within the blanket structure, although a 1.0-mm-thick copper first-wall undergoes a bulk rise of 26 K (maximum $\Delta T \simeq 6$ K across the structure, Fig. VII-4) leading to a maximum thermal stress of 1.2 MPa at the inlet end of the burn section. A radiation shield composed of a 0.1-m thick lead and a 1.4-m thick borated-water region protects the relatively low field (1.5-3.0 T) NbTi - Cu superconducting magnet coils.

TABLE VII-III

CHARACTERISTICS OF CTOR BURN SECTION

PARAMETER	VALUE
Length, L(m)	40
Blanket thickness, Δb(m)	0.48
Conducting shell	
• Thickness (m)	0.05
• Fraction of conductor in shell	0.7
Shield thickness (m)	1.5
Superconducting coil	
• Radius (m)	3.2-3.6
• Magnetic field strength (T)	3.5-1.5
First wall	
• Flared radius, r_w(m)	1.2-1.6
• Material	AMAX Cu (water cooled)
• Thickness (mm)	1.0
• Maximum bulk temperature rise (K)[a]	23
• Maximum thermal differential (K)	6
• Maximum thermal stress (MPa)	1.2
Beam dump (end of burn chamber)	
• Cylindrical geometry (radius(m) x length (m))	4 x 8
• Surface area (m^2)	200
• Maximum thermal load (MW/m^2)	2.5
• Average thermal load (MW/m^2)	0.77
• Material	AMAX Cu (water cooled)
• Thickness (mm)	1
• Maximum bulk temperature rise (K)	24
• Maximum thermal differential (K)	7.5
• Maximum thermal stress (K)	1.5

[a]Excursion at most severe location (burn chamber inlet).

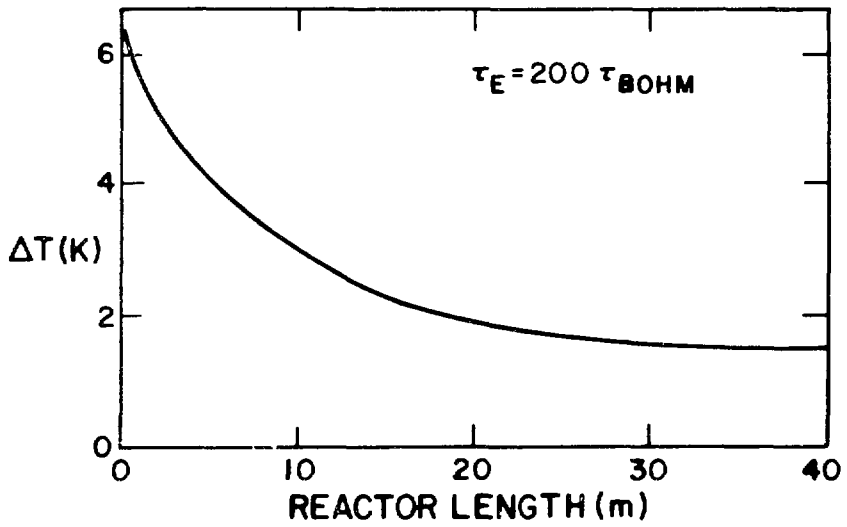

Fig. VII-4. Thermal gradient, ΔT, across 1-mm-thick water-cooled copper first wall along reactor burn section.

A major concern in any pulsed-plasma system is the thermal-fatigue lifetime of the first wall. As seen in Fig. VII-4 the most severe first-wall thermal cycling occurs at the inlet of the reactor burn chamber. Curves of temperature differential across the first wall, ΔT, versus number of thermal cycles is given in Fig. VII-5 using the procedure defined in Ref 37 for stainless steel, niobium and a high-strength copper alloy[38] (AMAX - 0.06% Mg, 0.15% Zr, 0.4% Cr, balance Cu). Also plotted on Fig. VII-5 are the corresponding temperature differences, ΔT, for each of the three materials if used in the burn section inlet of the reference CTOR design. Stainless steel would withstand the thermal cycling for only 6600 cycles or 11 hours in the reference design. Both niobium and the high-strength copper alloy are expected to present no fatigue problems, although neutron damage effects must also be considered. From Fig. VII-5, the copper alloy represents a superior choice and is suggested as the potential first-wall material, at least for the first few meters of CTOR length.

At the exit end of the reactor the magnetic field lines are flared, and the thermal conduction energy (900 MJ/pulse) is collected in a 200 m^2 cylindrical beam dump 8-m long and 4-m in radius, as is listed in Table VII-III. The heat load on this surface (2.5 MW/m^2 peak), is then similar to

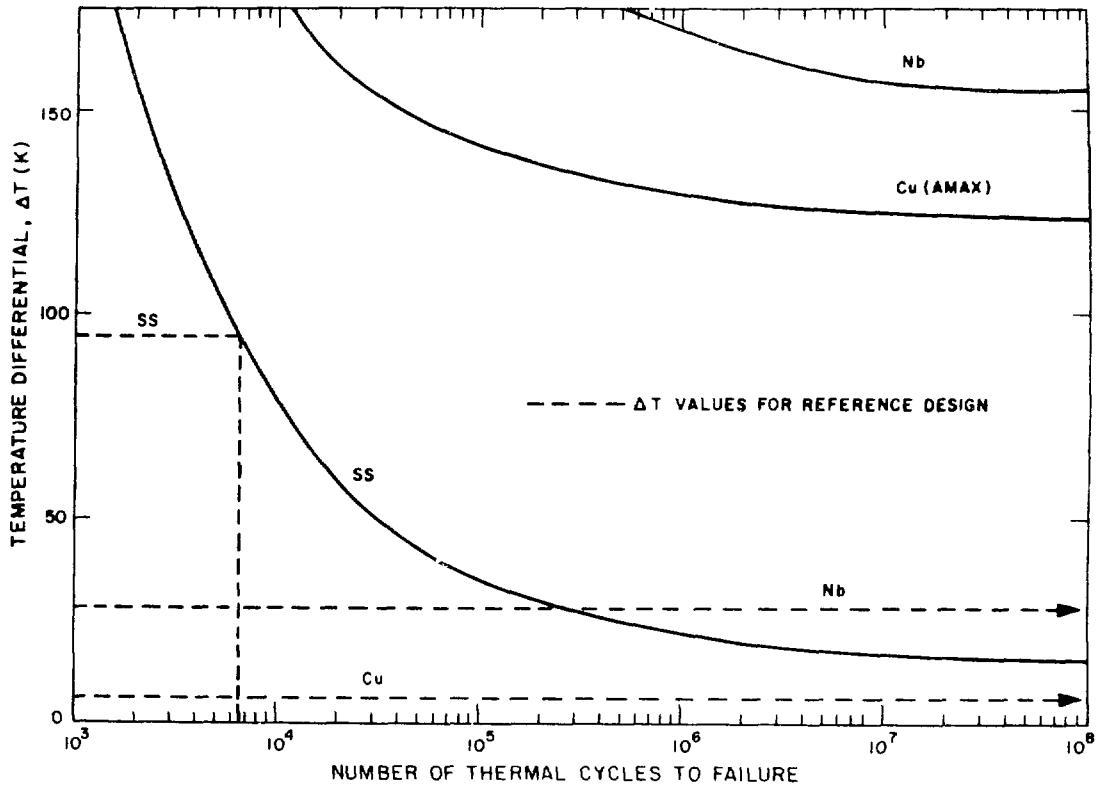

Fig. VII-5 Temperature differential, ΔT, versus first-wall lifetime for stainless steel, copper (AMAX)[38] and niobium. All shown are the values of ΔT for the same materials placed at the most severe location (burn section inlet).

that encountered by the first wall (2.0 MW/m^2) and using a similar construction no thermal fatigue problems are expected. In both cases these water-cooled surfaces are expected to be maintained below the burnout flux for subcooled boiling[39] (3-6 MW/m^2) although this point must be carefully considered to prevent local "hot spots".

VIII. CONCLUSIONS AND FUTURE DIRECTIONS

A parametric evaluation of sample design points for a Compact Toroid reactor that uses a Field-Reversed Theta Pinch for a plasma source has been performed numerically for a wide range of plasma transport, plasma densities, reactor radii and lengths. For an energy confinement time of 200 Bohm times (projected from tokamak confinement) an optimal burn is achieved at a first-wall radius of 1.2 m. The radius of the conducting shell must be tapered 40%

from 1.7 m to 2.1 m over the 40-m reactor length as the plasmoid velocity varies from 30 to 10 m/s. The reactor length could be shortened by increasing the shell thickness ($\delta \sim 0.05$ m) or decreasing the inlet plasmoid velocity; the 40-m reactor length is considered to give an optimal system, however, in terms of minimizing the FROP source requirements while simultaneously minimizing the total reactor power. This reactor system produces 310 MWe with a recirculating power fraction of 0.15. Smaller radius systems are achievable, although to maintain a good energy balance, the plasma density must be increased, leading to a higher first-wall thermal cycle.

Generally, the CTOR is represented as a high-Q system of modest size. The pulsed energy storage requirements are only ~ 60 MJ of capacitive energy for the FROP, a 175-MJ homopolar generator and 25, 7-MJ homopolar machines distributed along the traveling-wave network. Energy recovery is achieved in the quench region without the use of opening switches, with the plasma motion providing the necessary switching characteristics. The high-voltage and active source elements have been completely removed from the totally passive burn section. The linear system configuration simplifies maintenance and construction procedures. A natural divertor is also presented by the open-field line geometry outside the separatrix.

The realization of this attractive system is contingent upon the transport properties assumed for the plasma. Systems with high losses ($\tau_E \sim$ 0.1 s for the design plant) will either require higher operating densities (leading to higher first-wall thermal cycle) or systems of larger radial dimensions. Since the magnitude of the source requirements increase in proportion to $\sim nr_w^3$, larger pulsed power requirements will be imposed. Particle transport rates above those assumed here may also have adverse effects on the burn cycle. The batch-burn system used here assumes little change in the particle inventory during the ~ 2-s burn. Particle loss is likely to occur along with injestion of gas streaming to the plasmoid from the quench region. The competition of these two processes will determine the time-dependent particle inventory, a process that requires more detailed modeling.

Recommendations for future work include primarily engineering considerations, although further understanding of plasma transport must be incorporated in the design-point determination. Detailed designs of the FROP and compressor sections must be undertaken to define more clearly the energy

losses and physical dimensions of these two important systems. Slower plasma sources, such as the coaxial theta-pinch, should be investigated in order to minimize the use of high-voltage elements. The quench region must also be more clearly defined along with the necessary neutral particle densities needed to quench the plasma. Implications of the power streaming from the plasma and deposited at reactor ends requires quantification; such streaming is expected to result in a density gradient along the machine which will certainly impact energy/particle transport. The first-wall/blanket temperature and mechanical stresses must be optimized in terms of burn chamber lifetime and required maintenance intervals; even more conventional thermal systems, such as the pressurized water blanket system proposed for the Starfire tokamak reactor,[40] should be considered. Maintenance procedures and overall plant layout would also be refined. Lastly, a technological assessment of the CTOR plant should then be made, particularly with respect to the new technologies required of the plasma source, heater and quench sections.

The reactor study presented herein in conjunction with other CT design efforts (Sec. I and Sec. III) has led[4] to several general conclusions that are summarized in Table VIII-I.

TABLE VIII-I

GENERAL CONCLUSIONS FOR THE COMPACT TOROID REACTOR

- Steady-state, in situ plasma startup CT reactor does not exist. A mechanism other than active feedback is needed to stabilize such a steady-state device.
- MRFRMR/CTOR/IRC are moving independently toward similar reactor embodiments using pulsed-plasmoids translating in a linear burn chamber.
  - Fractional GW(e) systems
  - High-Q low-recirculating-power systems
  - Relatively low pulsed power requirements
  - Segregation of key functions (startup, burn, exhaust etc.)
- Potential for attractive CT reactors exist. Small reactor plasmas appear achievable without extravagant extrapolation of technology.

- Level of CT reactor studies are not sufficient to make quantitative economic intercomparisons with other more developed systems.

- Physics basis is not adequate to make a clear-cut choice between concepts, and economic analysis should ultimately be used to examine tradeoffs within a given system.

- Present knowledge allows a pulsed-plasmoid CT reactor which reflects to some degree a system of lower reliability, higher design constraints and potentially higher cost. In these systems only the plasmoid, the plasmoid source and the first-wall are pulsed with all other engineering systems being steady state.

  - A search for a truly steady-state CT reactor should continue

  - The actual cost of pulsed operation should be quantified; steady-state operation requires new physics, new plasma engineering systems and added costs.

- CT reactor studies are beginning to give some feedback to experiment/theory and this useful symbiosis should continue. Reactor physics models should strive for more uniformity of assumption and level of detail resulting from enhanced communication between physicists and reactor designers.

REFERENCES

1. H. Alfvén, "Magnetohydrodynamics and the Thermonuclear Problem," 2nd UN Conference on the Peaceful Uses of Atomic Energy 31, 3-5 (1958).

2. M. N. Bussac, H. P. Furth, M. Okabayashi, M. N. Rosenbluth, and A. M. M. Todd, "Low-Aspect-Ratio Limit of the Toroidal Reactor: The Spheromak," Proc. of the 7th Inter. Conf. on Plasma Physics and Controlled Nuclear Fusion Research, Innsbruck, Austria, IAEA-CN-37/X-1, III, 249-264 (1978).

3. H. Furth, "The Compact Torus Concept and the Spheromak," Proc. US/Japan Joint Symp. on Compact Toruses and Energetic Particle Injection, Princeton Plasma Physics Laboratory, Princeton, NJ, 3-7 (December 12-14, 1979).

4. Compact Toroid Symposium held at Los Alamos Scientific Laboratory, Los Alamos, NM (December, 1980).

5. G. A. Carlson, W. C. Condit, R. S. Devoto, J. H. Fink, J. D. Hanson, W. E. Neef, and A. C. Smith, Jr., "Conceptual Design of the Field-Reversed Mirror Reactor," Lawrence Livermore Laboratory report UCRL-52467 (1978).

6. W. C. Condit, G. A. Carlson, R. S. Devoto, J. N. Doggett, W. S. Neff and J. D. Hanson, "Preliminary Design Calculations for a

Field-Reversed Mirror Reactor," Lawrence Livermore Laboratory report UCRL-52170 (1976).

7. G. Carlson, K. R. Schultz, A. C. Smith, Jr., "Neutral-Beam-Sustained, Field-Reversed Mirror Reactor," Proc. US/Japan Joint Symp. on Compact Toruses and Energetic Particle Injection, Princeton Plasma Physics Laboratory, Princeton, NJ (December 12-14, 1979).

8. A. C. Smith, Jr., G. A. Carlson, K. R. Schultz, W. S. Neef, D. M. Woodall and R. E. Price, "Preliminary Conceptual Design of the Moving Ring Field-Reversed Mirror Reactor," Pacific Gas and Electric Company report 78FUS-1 (1978).

9. A. C. Smith, Jr., G. A. Carlson, H. H. Fleischmann, T. Kammash, K. R. Schultz, and D. M. Woodall, "The Moving-Ring Field-Reversed Mirror Reactor Concept," Symp. on Compact Toruses and Energetic Particle Injection, Princeton Plasma Physics Laboratory, Princeton, NJ (December 12-14, 1979).

10. A. C. Smith, Jr., G. A. Carlson, H. H. Fleischmann, T. Kammash, C. P. C. Wong and D. M. Woodall, "The Moving-Ring Field-Reversed Mirror Reactor Concept," Proc. 4th ANS Topical Meeting on the Technology of Controlled Nuclear Fusion, King of Prussia, PA (October 14-17, 1980).

11. J. D. Galambos, R. E. Olson, J. G. Gilligan, and G. H. Miley, "Operating Parameters for a Moving Plasmoid Heater (MPH) Reactor Concept," Trans. Amer. Nucl. Soc., 32, 28-29 (1979).

12. C. H. Choi, J. G. Gillegan and G. H. Miley, "The Saffire D-3 He Pilot Plant Concept," 1979 Annual report Fusion Studies Laboratory, University of Illinois.

13. A. M. M. Todd, R. E. Olson, J. G. Gilligan and G. H. Miley, "The Spheromak Fusion Reactor," Proc. 15th Intersoc. Energy Conversion Eng. Conf., 3, 2229-2236 (August 18-22, 1980).

14. A. E. Robson, "A Conceptual Design for an Imploding-Liner Fusion Reactor," 2nd Inter. Conf. on Megagauss Magnetic Field Generation and Related Topics, Washington, DC (May 29 - June 1, 1979).

15. R. L. Miller and R. A. Krakowski, "Assessment of the Slowly-Imploding Liner (LINUS) Fusion Reactor Concept," Proc. 4th ANS Topical Meeting on the Technology of Controlled Nuclear Fusion, King of Prussia, PA (October 14-17, 1980).

16. H. J. Willenberg, A. L. Hoffman, L. C. Steinhauer, and P. H. Rose, "TRACT: A Small Fusion Reactor Based on a Compact Torus Plasma," Proc. US/Japan Joint Symp. on Compact Toruses and Energetic Particle Injection, Princeton Plasma Physics Laboratory, Princeton, NJ (December 12-14, 1979).

17. H. J. Willenberg, "TRACT Fusion Reactor Studies," Proc. 4th ANS Topical Meeting on the Technology of Controlled Nuclear Fusion, King of Prussia, PA (October 14-17, 1980).

18. N. C. Christofilos, "Astron Thermonuclear Reactor," Proc. of the 2nd U.N. Conf. on the Peaceful Uses of Atomic Energy, 32, 279 (1958).

19. N. C. Christofilos, "Astron Plasma Parameters Confined in the Closed Magnetic Well of a Proton E-Layer," Proc. of Energy 70, Inter. Soc. Energy Conversion Eng. Conf., Las Vegas, NV, 1-36 (1970).

20. H. H. Fleischmann and T. Kammash, "System Analysis of the Ion-Ring Compressor Approach to Fusion," Nucl. Fus., 15, 1143-1155 (1975).

21. R. L. Hagenson and R. A. Krakowski, "Conceptual Physics Design of a Compact Torus Fusion Reactor (CTOR)," Los Alamos Scientific Laboratory report LA-8448-MS (July, 1980).

22. R. Hancox, R. A. Krakowski, W. R. Spears and R. L. Hagenson, "The Reverse-Field Pinch Reactor," Nucl. Eng. and Design (to be published, 1981).

23. R. L. Hagenson, R. A. Krakowski and G. E. Cort, "The Reversed-Field Pinch Reactor (RFPR) Concept," Los Alamos Scientific Laboratory report LA-7973-MS (August, 1979).

24. W. T. Armstrong, R. K. Linford, J. Lipson, D. A. Platts and E. G. Sherwood, "Field Reversed Experiments (FRX) on Compact Toroids," submitted to Physics of Fluids (1980).

25. R. K. Linford, W. T. Armstrong, J. Lipson, D. A. Platts and E. G. Sherwood, "Field Reversal Experiments," submitted to the 9th European Conf. on Controlled Fusion and Plasma Physics, Culham Laboratory, Abingdon, UK (1979).

26. C. E. Seyler, W. Grossmann, and L. C. Steinhauer, "End Stoppering by the Reversed Field Multiple-Mirror Concept," Comments Plasma Phys. Cont. Fusion 4, 21-30 (1978).

27. R. L. Miller and R. A. Krakowski, "Thermal Conduction and Alpha-Particle Constraints for the Ignition of a D-T Linear Magnetic Fusion (LMF) Reactor," Nucl. Fus., 18, 1722 (1978).

28. R.A. Krakowski, F. L. Ribe, T. A. Coultas, and A. J. Hatch, "An Engineering Design Study of a Reference Theta-Pinch Reactor (RTPR)," Los Alamos Scientific Laboratory report LA-5336 and Argonne National Laboratory report ANL-8019 (1974).

29. D. J. Rej, D. A. Larrabee, and H. H. Fleischmann, "Resistive Wall-Interaction of Axially Moving Field-Reversed E-Layers or Plasma Rings," School of Applied and Engineering Physics, Cornell University report FRL-12 (1979).

30. LASL CTR-Division Staff, "Proposal for FRX-C and Multiple-Cell Compact Torus Experiments," Los Alamos Scientific Laboratory report LA-8045-P (1979).

31. R. K. Linford, D. A. Platts, and F. G. Sherwood, "Field-Reversed Experiment (FRX)," in Controlled Thermonuclear Research Program (Compiled by K. S. Thomas and G. A. Sawyer), Los Alamos Scientific Laboratory report LA-7474-PR (1979).

32. K. I. Thomassen, "Conceptual Design Study of a Scyllac Fusion Test Reactor," Los Alamos Scientific Laboratory report LA-6024 (1976).

33. P. M. Bellan, "Spontaneous, Three-Dimensional, Constant-Energy Implosion of Magnetic Mirror Fields," Physical Review Letters 43, 858 (1979).

34. T. A. Oliphant, G. E. Gryczkowski and T. Kammash, "Transient Charge-Exchange Effects in a Neutral-Gas Layer," Nucl. Fus., 16, 263-268 (1976).

35. K. I. Thomassen (ed), "Conceptual Engineering Design of a One-GJ Fast Discharging Homopolar Machine for the Reference Theta-Pinch Reactor," Electric Power Research Institute report EPRI-ER-246, Project 469 (1976).

36. H. F. Vogel, M. Brennan, W. G. Dase, K. M. Tolk and W. F. Weldon, "Energy Storage and Transfer with Homopolar Machine for a Linear Theta-Pinch Hybrid Reactor," Los Alamos Scientific Laboratory report LA-6174 (1976).

37. L. F. Coffin, Jr., "Fatigue at High Temperature - Prediction and Interpretation," Proc. Instn. Mech. Engrs., 188, 109-127 (1974).

38. P. W. Taubenblat, W. R. Opie and Y. T. Hsu, "A New Copper Alloy with High Strength and Conductivity," Metals Engineering Quarterly, 39 (November, 1972).

39. S. Glasstone and A. Sesonske, Nuclear Reactor Engineering (Published by Van Nostrand Reinhold Company, New York, 1967).

40. C. C. Baker, G. A. Carlson and R. A. Krakowski, "Trends and Developments in Magnetic Confinement Fusion Reactor Concepts," Nuclear Technology - Fusion, 1, 5-77 (January, 1981).

41. R. K. Linford, personal communication, Los Alamos Scientific Laboratory, (1980).

42. D. Driemeyer, G. H. Miley and W. C. Condit, "A Monte Carlo Method for Calculating Fusion Product Behavior in Field-Reversed Mirrors," ANS Proceedings of the Topical Meeting on Computational Methods in Nuclear Engineering, Williamsburg, VA (1979).

APPENDIX A: PLASMA PROFILE MODELS

Since experimental evidence for the actual plasma profiles in the compact toroid plasma is rather sparse, several models can be postulated that exhibit roughly the same behavior observed under experimental conditions; generally flux conservation and equilibrium expressions are imposed. The rigid-rotor model assumes no velocity shear between the ions and electrons. The particle force equation may be written in cylindrical coordinates as

$$E_r + v_\Theta B_z = \frac{1}{qn}\frac{\partial p}{\partial r} \quad . \tag{A-1}$$

Assuming that T_i and T_e are independent of radius r, it follows that $\partial p/\partial r = \kappa_B T \partial n/\partial r$. Consequently, the electron and ion momentum equations may be written as

$$\frac{v_i}{r} + \frac{E}{rB} = \frac{k_B T_i}{erB}\frac{1}{n}\frac{\partial n}{\partial r} \tag{A-2}$$

$$\frac{v_E}{r} + \frac{E}{rB} = -\frac{k_B T_e}{erB}\frac{1}{n}\frac{\partial n}{\partial r} \quad , \tag{A-3}$$

which, upon subtracting, gives

$$\frac{1}{rB}\frac{1}{n}\frac{\partial n}{\partial r} = \text{CONSTANT} \quad . \tag{A-4}$$

In arriving at Eq. (A-4) the velocity shear, $(v_i - v_e)/r$, is assumed constant under the rigid-rotor approximation. The solution to Eq. (A-4) for the boundary conditions of interest is

$$B = B_o \tanh K \left(\frac{r^2}{R^2} - 1\right) \tag{A-5}$$

$$n = n_m \operatorname{sech}^2 K\left(\frac{r^2}{R^2} - 1\right) \quad , \tag{A-6}$$

where B_o is the vacuum field, and n_m is the maximum density at $r = R$, as is shown in Fig. A-1. Defining an equivalent sharp-boundary radius, a, (Fig. A-1), the value of K may be defined as

$$\frac{R}{a} = \frac{4K}{1 + \tanh K} \quad . \tag{A-7}$$

This expression allows the calculation of an equivalent volume of plasma as determined from the integration of Eq. (A-6). The radius of the separatrix, r_s, is found from the integration of Eq. (A-5) to be

$$r_s = \sqrt{2}\, R \quad . \tag{A-8}$$

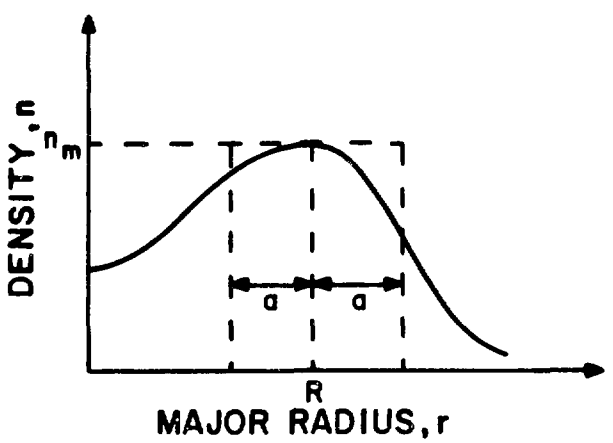

Fig. A-1. Definition of major radius R and equivalent sharp-boundary minor radius, a, for a FRC plasmoid.

The value of K is defined from the average-beta relationship found from the equilibrium expressions given in Appendix B. This expression is independent of profile and must be satisfied by the rigid-rotor expression. The average beta equation is

$$\langle\beta\rangle = \frac{\int_0^{r_s} (nk_BT)\, dV_s}{(n_m k_B T)\, V_s} = 1.0 - \frac{1}{2} x_s^2 \qquad \text{(A-9)}$$

where $V_s = \pi r_s^2 \ell$. Using Eq. (A-8), the value of K can be determined from

$$\frac{\tanh K}{K} = 1 - \frac{1}{2} x_s^2 \quad . \qquad \text{(A-10)}$$

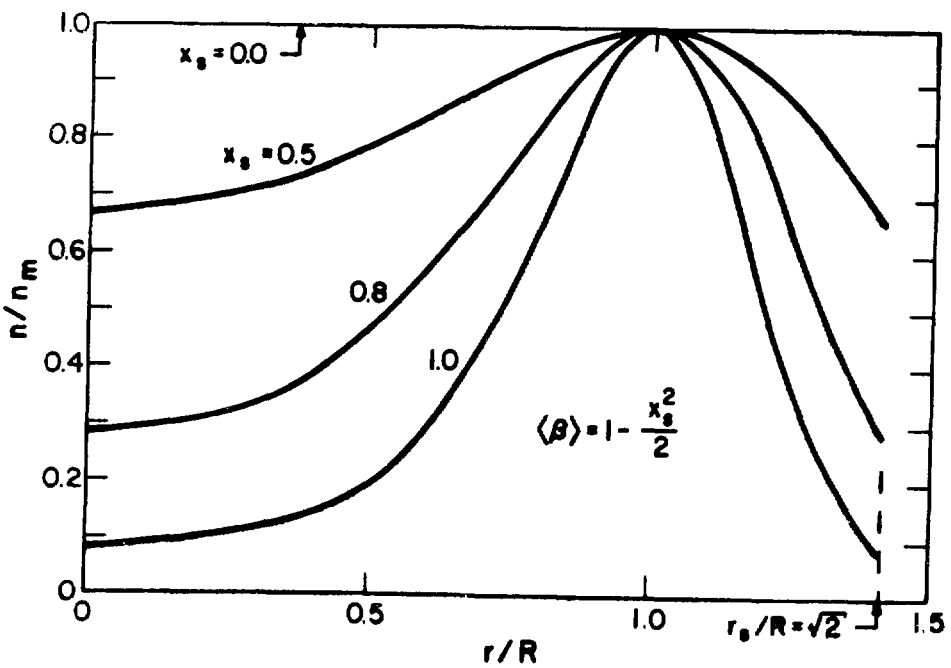

Fig. A-2. Rigid-rotor model profiles for various values of x_s.

Plots of density profiles for various values of x_s are shown in Fig. A-2. The profiles for $x_s \simeq 0.5$-0.7 are expected to be a good representation of present day experiments having relatively large ion-gyroradii (i.e., $R/\rho_i \lesssim 10$). These profiles, however, require large plasma pressures at the separatrix and are not expected to be a good representation of the profiles in a reactor system in which negligible plasma pressure should exist outside the separatrix (i.e., rapid particle loss along open field lines).

In order to better represent the expected plasma profiles, two conditions must be satisfied:

- negligible plasma pressure should exist after approximately one ion-gyroradii outside the separatrix radius, r_s.
- symmetry of flux surfaces about R should exist.

These conditions are satisfied by a simple power function given below.

$$n = n_m\left\{ 1 - \left|\frac{(r/R)^2 - 1}{[(r_s + \rho_i)/R]^2 - 1}\right|^{\nu}\right\} , \qquad \text{(A-11)}$$

where ν is determined by imposing the average beta expression, $\langle\beta\rangle = 1 - x_s^2/2$, as has been done for the rigid-rotor model. The result is given by

$$x_s = \frac{\sqrt{2}}{\left\{[(r_s + \rho_i)/R]^2 - 1\right\}^{\nu/2}\,(\nu + 1)^{1/2}} , \qquad \text{(A-12)}$$

which upon defining ρ_i/R specifies ν if it is noted that, $r_s/R = \sqrt{2}$.

A plot of density <u>versus</u> radius is shown in Fig. A-3 for $x_s = 0.5$ and for a range of R/ρ_i values. Also shown on Fig. A-3 is the rigid-rotor model which approximates the profile for $R/\rho_i \sim 10$. Sample profiles for $R/\rho_i \to \infty$, a condition that approximates reactor conditions ($R/\rho_i \sim 50$-100), are shown in Fig. A-4 for various values of x_s. For the value used to model the reactor, $x_s = 0.5$, the sharp-boundary model represents an excellent approximation to the expected profile. An interesting consequence of the sharp-boundary nature

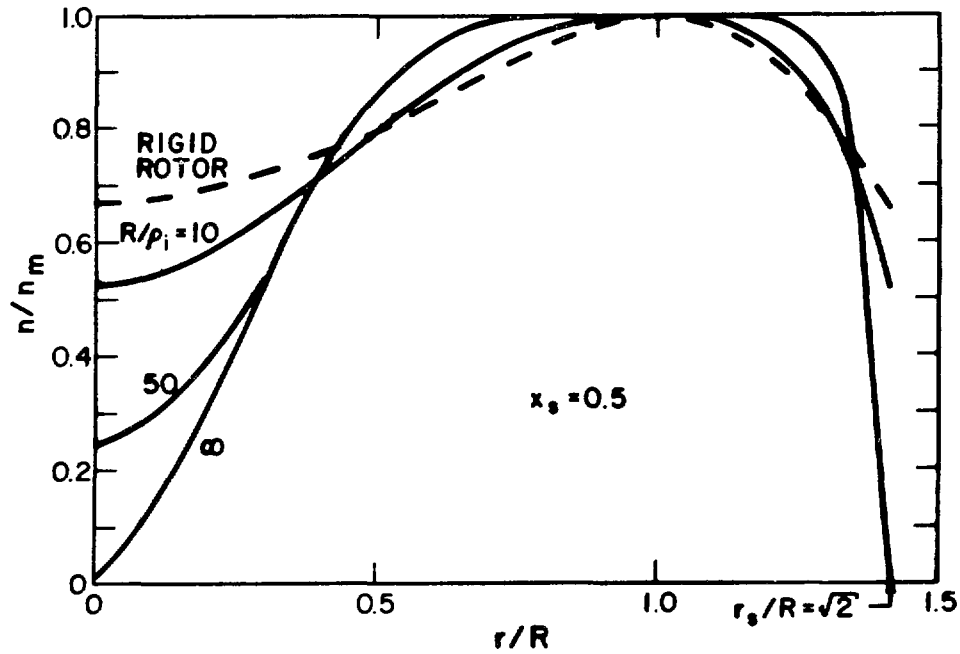

Fig. A-3. Sample profiles assuming a power function model for various ion-gyroradii. The rigid-rotor model is also shown.

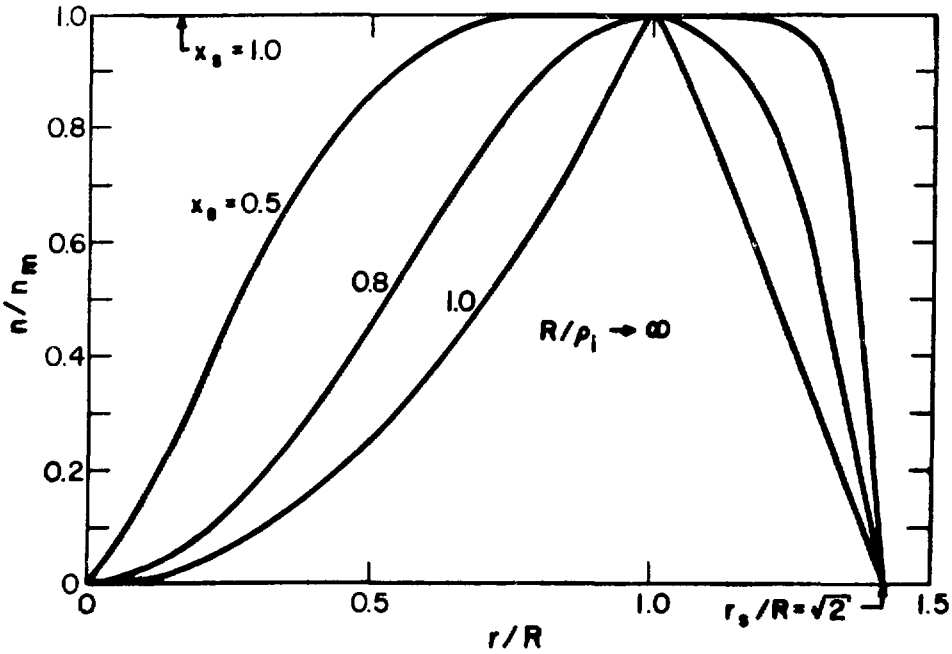

Fig. A-4. Sample profiles assuming a power function model, small ion-gyroradii ($R/\rho_i \to \infty$) and satisfying the average-beta condition.

of the profile at $x_s = 0.5$ is the small effective thickness of the plasma sheath region. A value of $R/\rho_i = 100$ actually corresponds to a sheath thickness of only seven ion-gyroradii. This behavior probably explains the reduction in confinement time as x_s is lowered under experimental conditions.

In summary, reactor plasmoids may contain 100's of ion-gyroradii across the macrodimensions (i.e., R or a), but less than 10 ρ_i may define the typical gradient length. Hence, these high R/ρ_i systems may still be FLR stabilized, but the steep (relative to the plasmoid dimensions) gradients may drive unacceptably large transport losses. This stability may be crucial for all reactors based on FRC's and requires considerably more study. It is emphasized that this prognoses is based on only two assumptions: a) equilibrium and b) zero pressure at one ion gyroradius outside the separatrix.

APPENDIX B: COMPACT TOROID EQUILIBRIUM

Before even a global plasma energy balance can be formulated and evaluated, a three-dimensional equilibrium for the CT plasma must be defined. An analytic equilibrium expression is determined from an axial force balance that in turn is used in conjunction with radial pressure balance. An approximate equilibrium expression as proposed by R. Linford[24] is given here. This result is used in Appendix A to model profile effects.

Three regions are identified in the vicinity of the CT plasma, as is shown in Fig. B-1. Region I includes the closed field plasmoid, but the regions near the separatrix are excluded; Region II contains the complex transition between regions of closed and open field lines; and Region III includes all open field lines located far away from the separatrix. Regions I and III are considered to be sufficiently long to ensure that changes in the plasma length do not alter the magnetic field/plasma configuration. The energy contained in Region II then remains unchanged when the plasma column undergoes axial motion.

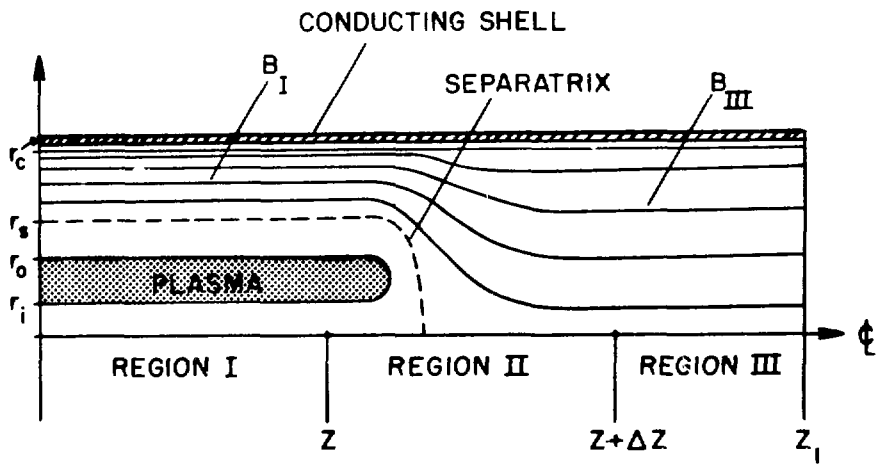

Fig. B-1. Schematic diagram of model used to generate the CT equilibrium expressions.

Assuming a sharp-boundary plasma, the axial force exerted by the plasma and magnetic field trapped inside the plasma column is given by

$$F_p = \frac{B_I^2}{2\mu_o} \pi \, (r_o^2 - r_i^2) \quad , \tag{B-1}$$

where the pressure exerted by the plasma column must equal that provided by the vacuum field in Region I, $B_I^2/2\mu_o$. This force must be counterbalanced by the vacuum fields and is given as

$$F_B \simeq \frac{\partial}{\partial z} \quad \frac{B_I^2}{2\mu_o} \pi \, [r_c^2 - (r_o^2 - r_i^2)]z + W_{BII}$$

$$+ \frac{B^2_{III}}{2\mu_o} \pi \, r_c^2 \, (z_1 - z - \Delta z) \quad , \tag{B-2}$$

where the energy associated with the assumed "invariant" Region II is designated as W_{BII}, and B_{III} is the magnetic field in Region III. Performing the differentiation, the opposing force becomes

$$F_B \simeq \frac{B_I^2}{2\mu_o} \pi \, [r_c^2 - (r_o^2 - r_i^2)] - \frac{B_{III}^2}{2\mu_o} \pi r_c^2 \quad . \tag{B-3}$$

Imposing flux conservation between the conducting wall radius, r_c, and the separatrix radius, r_s, leads to

$$B_I \, \pi(r_c^2 - r_s^2) = B_{III} \, \pi r_c^2 \quad . \tag{B-4}$$

Flux conservation inside the separatrix results in

$$r_i^2 = r_s^2 - r_o^2 \quad , \tag{B-5}$$

and the force exerted by the vacuum fields becomes

$$F_B = \frac{B_I^2}{2\mu_o} \pi \left[r_o^2 + 3r_i^2 - (r_i^2 + r_o^2)^2/r_c^2 \right] \quad . \tag{B-6}$$

Equating the two forces given by Eqs. (B-1) and (B-6) leads to

$$2r_i r_c = r_i^2 + r_o^2 \quad , \tag{B-7}$$

and using Eq. (B-5) gives the following relationship between the separatrix radius, r_s, and the conductor radius, r_c

$$r_s^2 = 2r_i r_c \quad . \tag{B-8}$$

Simplifications of these equilibrium equations are found if the separatrix is located at the conducting shell ($r_c \simeq r_s$), which from Eqs. (B-7) and (B-8) yields

$$r_o/r_i = \sqrt{3} \quad . \tag{B-9}$$

Defining an effective major radius, R, for the CT plasmoid, and defining a thickness or "minor diameter", 2a, of the plasma column (Figs. A-1 and B-1) give the following relationships

$$r_o = R + a \tag{B-10A}$$

$$r_i = R - a \quad . \tag{B-10B}$$

For the case where $r_c = r_s$, Eq. (B-9) becomes

$$R/a = 2 + \sqrt{3} \quad . \tag{B-11}$$

For highly elongated plasmoids with the separatrix located near the conducting shell, the aspect ratio of the toroidal plasma, R/a, is predicted to lie in the range 3 to 4.

The fraction of cross-sectional area within the separatrix that is occupied by plasma is defined as the average beta, $\langle\beta\rangle = \pi(r_o^2 - r_i^2)/\pi r_s^2$. Using Eqs. (B-7) and (B-8), this expression reduces to

$$\langle\beta\rangle = 1 - 0.5x_s^2 \quad , \tag{B-12}$$

which directly shows the rapid increase in beta as $x_s = r_s/r_c$ is reduced. For the case $x_s = 1$, half the area would be filled with plasma. This expression for $\langle\beta\rangle$ can be shown[24] to be generally valid for any plasma profile. In fact, diffuse profile equilibrium calculations[41] produce substantially the same behavior as the sharp-boundary model.

APPENDIX C: ADIABATIC COMPRESSIONAL HEATING

Using the equilibrium results from Appendix B and applying the adiabatic law results in the scaling relationships that describe the thermodynamic response of the plasma to geometric changes. The vacuum magnetic field pressure can be expressed as

$$P = B_o^2/2\mu_o = \Phi_i^2/(2\mu_o\pi^2 r_i^4) \quad , \tag{C-1}$$

where the flux, Φ_i, inside the radius r_i is assumed constant with time. Substituting Eq. (C-1) into the adiabatic relationship

$$PV^\gamma = \text{Constant} \quad , \tag{C-2}$$

gives

$$[2r_i(r_c - r_i)\ell]^\gamma/r_i^4 = C_1 \quad , \tag{C-3}$$

where the plasma volume

$$V_p = \pi(r_o^2 - r_i^2)\ell \quad , \tag{C-4}$$

has been used, and C_1 is a constant. Equation (C-3) can be rearranged into the following form in conjunction with Eq. (B-8)

$$\ell/\ell_o = (\rho_o/\rho)^{4/\gamma}\,(r_s/r_{so})^{2[2/\gamma-1]}\,[1-1/2\rho_o^2]/[1-1/2\rho^2] \quad , \tag{C-5}$$

where $\rho = r_c/r_s$, and the subscript "o" indicates an initial or reference state. For the case of a plasmoid compressed by a radially-inward moving liner[14,15] with ρ = constant, Eq. (C-5) becomes for $\gamma = 5/3$

$$\ell/\ell_o = (r_s/r_{so})^{2/5} \quad . \tag{C-6}$$

This relationship between plasmoid length and radius is appropriate if the flux between the conducting shell and the separatrix is conserved, which for realistic liner compressions may not be completely true.[15] On the other hand, taking r_c as a constant, Eq. (C-5) reduces to

$$\ell/\ell_o = (r_s/r_{so})^{14/5} \left[1-1/2\rho_o^2\right]/\left[1-r_s^2/2\rho_o^2 r_{so}^2\right] \quad . \tag{C-7}$$

The two extreme cases represented by Eqs. (C-6) and (C-7) are depicted in Fig. C-1 for a range of initial values of conduction-to-separatrix ratios, ρ_o.

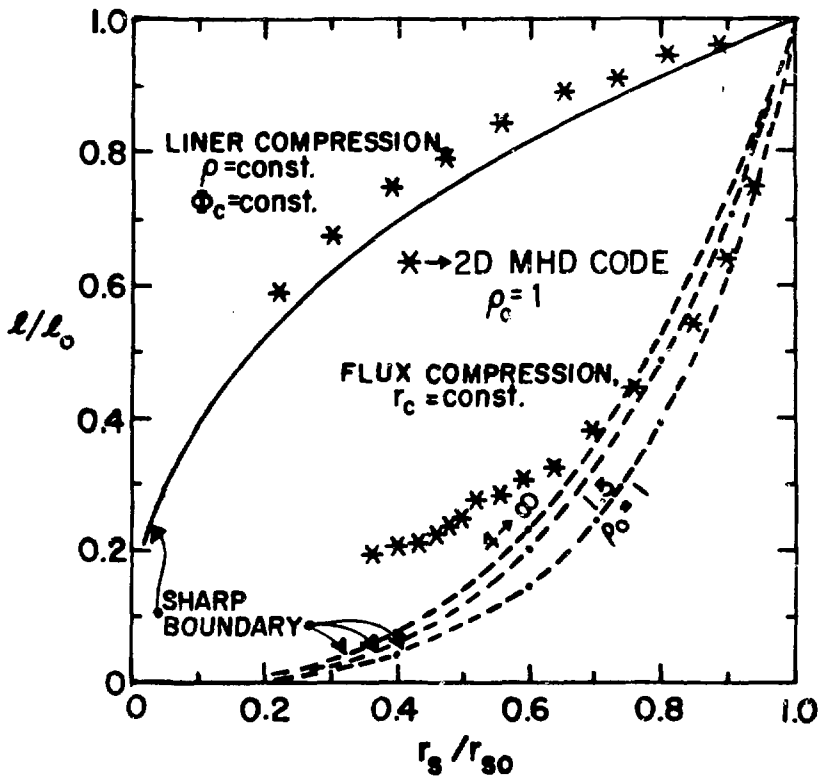

Fig. C-1. Length versus radius relationships for CT plasmoids compressed by flux conserving shells that either move with the separatrix radius (liners) or are stationary (FRΘP).

Good agreement is shown between the analytic curves and results from a two-dimensional simulation.[24] Deviations of the two results occur as the plasmoid becomes spherical and violates the analytic assumption $\ell \gg r_s$. The plasmoid exhibits considerably less length compression if the conducting shell is maintained near the plasma than for the case when the conducting shell radius is fixed as compression of the separatrix occurs. The insensitivity of the trajectory of ℓ/ℓ_o versus r_s/r_{so} to values of ρ_o for the flux-compression case (r_c is constant) allows Eq. (C-7) to be simplified

$$\ell/\ell_o = (r_s/r_{so})^{14/5} \quad , \tag{C-8}$$

where the bracketed terms in Eq.(C-7) have been taken to be of order one.

Using the adiabatic relationships, Eqs. (C-2),(C-6) and (C-8), a set of adiabatic invariants can be constructed, which are listed in Table C-I. Only for the case where r_c/r_s = constant is the conducting shell radius forced to vary as the plasmoid changes dimensions, whereas r_c is constant for the other two cases. The variation in plasmoid length with the separatrix radius is large for $r_s < r_c$ = constant, resulting in correspondingly large increases in temperature and density with decreasing separatrix radius, r_s. For compression by radially-moving liners, where $r_s \approx r_c$, only a modest length

TABLE C-I

ADIABATIC INVARIANTS[(a)] FOR TEMPERATURE, DENSITY AND PLASMOID LENGTH

COMPACT TORI		CYLINDRICAL PLASMA
r_c/r_s = Constant	$r_s < r_c$[(b)] r_c = Constant	ℓ = Constant
$Tr_s^{8/5}$	$Tr_s^{16/5}$	$Tr^{4/3}$
$nr_s^{12/5}$	$nr_s^{24/5}$	nr^2
$\ell r_s^{-2/5}$	$\ell r_s^{-14/5}$	ℓ

(a) Listed quantities are constant to changes in plasma dimensions assuming no heat gain or loss from the plasma.

(b) These quantities are approximately constant, subject to the simplification of Eq.(C-7) to Eq. (C-8) and r_c being fixed.

variation is envisaged during the compression, with the density and temperature variations being much closer to those expected for a purely cylindrical plasma. A graphic illustration of this behavior is shown in Fig. C-2, where the efficiency, η_{AC}, is defined as the ratio of the plasma cross-sectional area to the total cross-sectional area inside the radius r_c, assuming a plasma configuration with $\beta \simeq 1$. For a purely cylindrical plasma, which (initially) completely fills a chamber formed by the conductor at radius r_c, r/r_o begins at unity with the temperature varying as $T/T_o \propto (r/r_o)^{-4/3}$ (Table C-I). For the CT configuration, however, the plasma initially fills half the plasma chamber inside the conducting radius, r_c, as is given by Eq. (B-12). For the case where $r_s = r_c$, the efficiency of compression does not change, because the relative volume of plasma to magnetic field inside the conducting shell is constant. A compression that allows the separatrix to

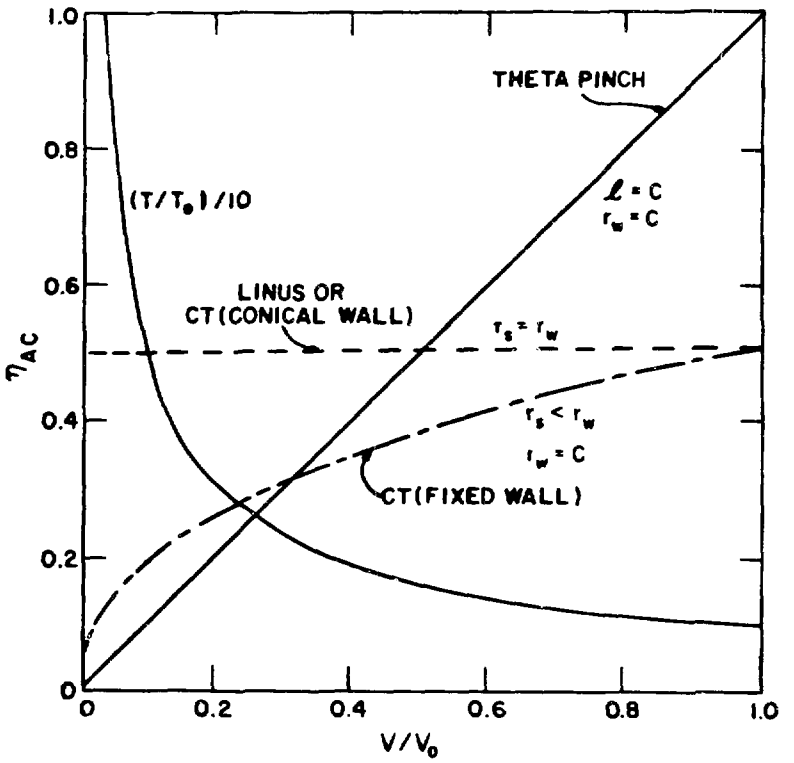

Fig. C-2. Dependence of adiabatic compression efficiency on a range of assumed equilibrium constraints.

move away from the conducting shell is less efficient because of the increased volume of magnetic field that must be introduced as the plasma is forced away from a stationary conductor.

The magnetic field energy necessary to perform a given compression can be minimized if the shell radius is reduced as the plasmoid is compressed. This prediction represents a distinct advantage of moving shell or liner compressions. Using a tapered compressor section, the ratio r_c/r_s can also be preserved. These approaches not only minimize the required magnetic energy, but the stabilizing effect of the conducting shell is also preserved. Experimental values[24] of $r_c/r_s \simeq 2.0$ are taken as a design criteria imposed here on the reactor scaling.

APPENDIX D: CTOR BURN MODEL AND SYSTEMS COMPUTER CODE

The numerical system model used to describe the CTOR is based on a zero-dimensional, three-particle, time-dependent burn computation. The physics basis for this code is described in this Appendix.

Starting from the post-implosion conditions given by the Marshall coil parameters (Appendix F), the behavior of the compact toroid is numerically followed through the compressor section as adiabatic compression raises the plasma temperature in excess of that required for ignition. The plasma trajectory is subsequently followed through the burn section, where conducting shell losses (translational drag) are supplied by radial plasma expansion that is driven by alpha-particle heating of the plasmoid. The velocity of the plasmoid is reduced during the translation by tailoring the flare of the burn chamber in order to maintain a constant first-wall exposure to fusion neutrons along the burn-chamber length. Additionally, the CTOR code provides the following information for each time-dependent plasma simulation:

- Complete time history of all plasma properties, including plasmoid velocity and spatial position versus time along axial length of reactor burn section.
- Required dimensional changes in conducting shell along axial length, specifying dimensions of the reactor device.
- Complete reactor energy balance and a listing of all system energy requirments for the engineering Q-value, Q_E, or recirculating power fraction, $\varepsilon = 1/Q_E$.
- A simultaneous, time-dependent one-dimensional response of the first wall during the burn phase at selected intervals along the axial length.
- A simultaneous, time-dependent one-dimensional mechanical/structural response of the first wall at selected intervals along the axial length.
- required values of bias magnetic field produced by the superconducting magnet coil versus axial length.

1. Plasma Model. Modeling the three-dimensional time-variation in plasma size requires the development of dynamics equations that include a description of variations in conducting-shell radius and the level of the magnetic field. These dynamics equations are derived from the plasma energy

balance subject to the constraints imposed by the equilibrium equations given in Appendix B.

The plasma energy balance is given by

$$\frac{d}{dt}\left[1.5pV\right] = \sum_i P_i - p\frac{dV}{dt} \quad , \tag{D-1}$$

where the plasma pressure, p(Pa), volume, $V(m^3)$, and plasma powers, $P_i(W)$ are used. Performing the derivative, Eq. (D-1) can be written as

$$\frac{5}{2} p \frac{1}{V}\frac{dV}{dt} = \frac{\sum P_i}{V} - \frac{3}{2}\frac{dp}{dt} \quad . \tag{D-2}$$

Noting that the plasma volume is

$$V = \pi(r_o^2 - r_i^2)\ell \quad , \tag{D-3}$$

and using the equilibrium expression given in Eq. (B-7), the volumetric term in Eq. (D-2) becomes

$$\frac{1}{V}\frac{dV}{dt} = \frac{\dot{r}_i\left[\frac{r_c}{r_i} - 2\right] + \dot{r}_c}{r_c - r_i} + \frac{\dot{\ell}}{\ell} \quad , \tag{D-4}$$

where $\dot{r}_i$ represents the time derivative of the radius r_i. The sharp-boundary plasma model requires $p = B^2/2\mu_o$ where B is the vacuum magnetic field level. Substituting this identity into Eq. (D-2) and using Eq. (D-4), the time-dependent plasma length is described by

$$\dot{\ell} = \ell \left\{ \frac{0.4}{pV} \sum P_i - \frac{1.2\dot{B}_z}{B_z} - [\dot{r}_i(\frac{r_c}{r_i} - 2) + \dot{r}_c]/(r_c - r_i) \right\} . \qquad \text{(D-5)}$$

The variation in radial plasmoid dimension is obtained by imposing flux conservation inside the separatrix radius. This condition implies that

$$\pi r_i^2 B_Z = \Phi = \text{CONSTANT} \quad , \qquad \text{(D-6)}$$

Taking the appropriate derivatives result in

$$\dot{r}_i = - \frac{\dot{B}}{B} \frac{r_i}{2} \quad . \qquad \text{(D-7)}$$

Using Eq. (D-5) and (D-7) along with the equilibrium Eqs. (B-7) and (B-8) completely defines the time-dependence of three-dimensional variations in plasmoid shape as the magnetic field, B, and/or the radius of the conducting shell, r_c, is varied.

As noted in Eq. (D-5), evaluation of a plasmoid burn cycle also requires a plasma power balance. Specifically,

$$\sum_i P_i = P_\alpha - P_{RAD} - P_{COND} \qquad \text{(D-8)}$$

which corresponds, respectively, to alpha-particle heating, radiation losses and thermal conduction. The alpha-particle power is given by

$$P_\alpha = 5.64(10)^{-13} n_D n_T \langle \sigma v \rangle V \quad , \qquad \text{(D-9)}$$

where n_D and n_T are the deuterium and tritium number densities. The radiation term consists primarily of Bremsstrahlung, with cyclotron being insignificant

in the high-beta systems being considered here. The Bremsstrahlung loss term is given by

$$P_{BR} = 5.35(10)^{-37}\, n_e^2\, Z_{eff}\, T_e^{1/2}\, V \quad , \tag{D-10}$$

where Z_{eff} is the sum of $n_K Z_K^2$ divided by the sum of $n_K Z_K$ over all ion species, K.

The conductive plasma losses can be properly treated as a function of time only by a one-dimensional MHD code, and even then, only if the transport properties are known. A calculation at this level is beyond the scope of this study; a number of scaling expressions, instead, are used to investigate the sensitivity of the reactor design to a range of reasonable transport models. The various transport models used by the computer simulation are given below.

The gyroradius for any species, s, is

$$\rho_s = 310B(Z_s/T_s a_\rho)^{1/2} \quad , \tag{D-11}$$

where the magnitude of the particle charge, Z_s, temperature, T_s, and atomic mass number, a_s, are used. The ion-ion and electron-ion collision times are, respectively,

$$\tau_{ii} = 4.526(10)^{17}\, a_i T_i^{1.5}/n_i \ell n\Lambda \tag{D-12}$$

$$\tau_{ei} = 1.853(10)^{16}\, T_e^{1.5}/n_e \ell n\Lambda \quad , \tag{D-13}$$

with the corresponding classical thermal conduction being represented by the following loss times

$$\tau_i = \tau_{ei}\, (a/\rho_i)^2 \tag{D-14}$$

$$\tau_e = \tau_{ee} \, (a/\rho_e)^2 \quad . \tag{D-15}$$

The average plasma radius, a, is used to estimate transport losses in this "point-plasma" approximation. Since $\tau_i << \tau_e$, ion-thermal conduction is a dominant classical loss mechanism. Other transport scalings include a Bohm-like formalism

$$\tau_{BOHM} = a^2 B/63 \, T_e \quad , \tag{D-16}$$

and an Alcator (tokamak) scaling

$$\tau_{AL} = 3(10)^{-21} \, na^2 \quad . \tag{D-17}$$

At constant magnetic field level, B, Alcator scaling has exactly the same functional dependence as the Bohm-like formalism and corresponds in magnitude to ~ 200 Bohm confinement times at B = 1 T. Numerous parameter studies were performed through this CTOR study for classical and multiples of the Bohm confinement time.

The numerical simulation of CTOR accomodates particle loss and refueling, although, particle inventory variations are assumed to be affected only by burnup in the burn cycles exhibited in this report. This assumption is essentially equivalent to substantial particle recycle between the moving plasmoid and particles propagating from the enhanced region of density in the quench region.

Particle loss is assumed for the lower-hybrid-drift case which corresponds to an anomalous escape of all particle species. The loss rate is taken as[37]

$$\tau_{ND} = \left(\frac{2}{\pi}\right)^{1/2} \frac{\mu_o^{3/2} \, e^{5/2}}{m_i^{1/2} \, m_e^{1/2}} \frac{1}{a_i^{1/2}} \left(\frac{1+\Theta}{\Theta}\right)^{1/2} \langle\beta\rangle \frac{n^{3/2} R^4}{(\kappa_B T_i/e)^{1/2}} \, f_p \quad , \tag{D-18}$$

where $\Theta = T_i/T_e$, a, is the ion mass in amu, and f_p relates to the cube of the

plasma gradient length and is taken as[41] $\sim x_s^6/40$. This scaling is indicative of the sharp edge gradients that are expected as x_s is reduced (Appendix A). The above expression is used separately for the energetic alpha-particles and the deuterium-tritium species.

Lastly, alpha-particle heating is treated by a Fokker-Planck calculation which utilizes fifty velocity groups to model alpha-particle slowing down in a homogeneous spatial region. The addition of particles to the alpha-particle distribution function as a result of the fusion yield is given by

$$\Delta f_\alpha(n/v^3) = (\Delta n_\alpha/\sqrt{\pi}\ \Delta_d 4\pi v_\alpha^2)e^{-[(v - v_\alpha)/\Delta_d]^2} \quad , \tag{D-19}$$

where v_α is the velocity corresponding to the 3.52 MeV alpha-particle, Δn_α is the number density of alpha-particles added at each time step Δt, and the Doppler broadening caused by the background ion species is $\Delta_d = (\kappa_B T_i/2m_i)^{1/2}$. Prompt-alpha losses are also taken into account using the results from particle-orbit calculation[42] in a Hill's vortex. The fraction of alphas retained at any given time is used in the form of the following fitted function

$$f_\alpha = 0.33\ r_s B_v + 0.03, \quad 0.0 < r_s B_r < 2.94$$

$$f_\alpha = 1.0, \ r_s B_v > 2.94 \quad . \tag{D-20}$$

The value of f_α is typically near unity for an attractive plasma burn cycle.

During each time step the electron temperature is adjusted according to the varying plasma volume, alpha-particle heating, classical electron-ion equipartition and plasma powers P_{RAD} and P_{COND}. Similarily, the ion temperatures reflect the volume change, ion-electron equipartition, alpha-particle heating and power loss P_{COND}. At the end of each time step the alpha-particle-velocity distribution is modified to take into account plasma expansion. The energy equipartition between plasma species is followed by the Fokker-Planck calculation.

2. Plasmoid Driving Function. Achieving burn cycles that operates on the basis of a high-yield plasmoid requires the appropriate variation in conducting shell radius and bias field along the length of the device. The radial compression required to achieve ignition from the initial FRΘP implosion may be estimated from the analytical results in Appendix C. This estimate of required compression provides guidance and input to the numerical calculation. The magnetic flux inside the conducting shell is assumed conserved along the length of the machine (excluding quench). This condition implies

$$\dot{B} = B[2\dot{r}_c/r_c] \tag{D-21}$$

and also maintains a constant value of x_s along the machine. Specifying $\dot{r}_c$ then allows the plasma dynamics to be calculated. Typically, $\dot{r}_c$ is taken as a linear function in the compressor section.

The required expansion of the conducting shell in the burn section is calculated from the following expression

$$p \frac{dV}{dt}\Big|_r = P_\eta \quad , \tag{D-22}$$

where P_η is the ohmic dissipation (translation drag) imposed by the presence of the shell near the plasmoid. The left-hand side of Eq. (D-22) represents the direct-conversion work resulting from the radial expansion of the FRC plasmoid which must be realized in the form of plasmoid translational motion. Using Eq. (D-4), omitting the $\dot{\ell}/\ell$ term, allows Eq. (D-22) to be written as

$$\dot{r}_c = r_c P_\eta / 2pV \quad . \tag{D-23}$$

The conducting shell dissipation, P_η, is calculated in Appendix E.

Finally, the quench region allows flux to escape through a fixed conducting shell ($\dot{r}_c = o$). The magnetic field between the conducting shell and separatrix is reduced linearly until $r_w \simeq r_s$. This procedure directly

extracts approximately 30-40% of the energy stored within the translating plasma/field system.

Completing the calculation of the burn and conducting-shell requires the plasmoid velocity, v, to be externally imposed. The variation in velocity is constrained by requiring a uniform first-wall neutron loading throughout the burn section. This condition is achieved by requiring that

$$v \propto P_\alpha / r_w \quad . \tag{D-24}$$

The magnitude of the velocity at the inlet of the burn section is varied parametrically from $v = 1\text{-}5(\ell/\tau_s)$, where the time, τ_s, is associated with the loss of flux between the separatrix and first wall (Appendix E). The plasmoid expands and reduces its velocity as the burn proceeds until $v \leq (\ell/\tau_s)$, whereupon the plasmoid motion is terminated, a quench is allowed to occur and the CTOR burn-chamber length is determined.

3. Evaluation of Energy Flows. From Sec. IV.B. and Fig. IV-2 the system energy balance was given as

$$Q_E = \eta_{TH} W_{TH} / (W_{BANK} + W_{COMP} - W_{EXP} + W_{AUX}) \quad , \tag{D-25}$$

where W_{TH} is the total plasmoid thermal yield and η_{TH} the thermal-to-electric conversion efficiency. The plant auxiliary energy requirements, W_{AUX}, is taken as a fraction (0.07) of the gross electric, W_{ET}. The energy requirements of the FRΘP plasma source capacitor bank, W_{BANK}, the homopolar motor/generator plasmoid compressor, W_{COMP}, and the plasmoid expansion energy, W_{EXP}, recovered at quench remain to be determined. This section describes in detail the calculation of the later quantities.

The total energy stored inside a radius r_c (typically, that of the conducting shell) over the plasmoid length ℓ is

$$W_B = \frac{B^2}{2\mu_o} \left[\pi r_c^{\,2} \ell - V_p\right] + W_p \quad , \tag{D-26}$$

where the vacuum field, B, plasma volume, $V_p(m^3)$ and plasma energy, $W_p(MJ)$ are used. The initial field energy, W_{BO}, stored inside the Marshall coil at a time corresponding to the post-implosion phase is evaluated from Eq. (D-26) using $r_c = r_s/0.7$ as typical[32] for the inside coil radius. For a 50% efficient transfer the capacitor bank energy is then computed to be $W_{BANK} = 2.0W_{BO}$.

The plasmoid and associated magnetic field subsequently leaves the Marshall coil with an energy W_{BO} and enters the compressor region. The quantity of energy added to this system in the compressor region must be given by

$$W_{COMP}\eta_{ETS} = W_{BI} - \frac{B_o^2}{2\mu_o}\pi r_c^2 \ell - W_{BO} + W_{RC} \quad , \tag{D-27}$$

where the bias field generated by the superconducting coil, B_o, is ultimately compressed to the vacuum magnetic field level, B, as the plasmoid is injected into the burn section. The first term in Eq. (D-27) represents the total energy of the plasmoid and associated magnetic field, as determined by Eq. (D-26) evaluated at the burn-section inlet. Subtracting the initial energy present inside the conducting shell (second term), the energy already added by the Marshall gun, W_{BO}, and accounting for resistive losses in the compressor, W_{RC}, gives the required energy store, W_{COMP}, of the homopolar generator. Imposing flux conservation between the plasmoid separatrix and the conducting shell, Eq. (D-27) can be written as

$$W_{COMP}\eta_{ETS} = \beta\frac{B^2}{2\mu_o}\pi r_s^2 \ell + W_p - W_{BO} + W_{RC} \quad , \tag{D-28}$$

where $\beta = 1-x_s^2/2$ from Appendix B.

At quench the conducting shell is connected as a magnet coil, allowing flux to escape until $B \sim B_o$, using the dynamics equations listed in Appendix D.1. Using Eq. (D-26) to calculate the change in energy inside the conducting shell before and after this process gives W_{EXP}, with the remaining plasmoid energy inside the separatrix radius, r_s, being thermally dissipated.

APPENDIX E: TRANSLATION PROPERTIES

The FRC plasmoid is to be stabilized by a passively conducting shell during a reactor burn. If a stationary plasmoid is used under these circumstances, the electrical skin time for the shell, τ_s, must be greater than the burn time, τ_B. On the other hand, the translating FRΘP approach requires a passively conducting shell with a skin time that is comparable with the plasma residence time within the conducting shell. In addition, first-wall thermal cycling is minimized when using the translating approach. This Appendix includes computations of the conducting shell electrical skin depth and associated translation drag powers, along with quantitative arguments for locating the shell outside the blanket region.

As the FRΘP plasmoid is translated into the burn chamber, the flux, Φ_c, contained inside the conducting shell is conserved and compressed between the separatrix and the conducting shell, as is illustrated in Fig. B-1. Conservation of Φ_c is provided by the superconducting coils generating a vacuum field, B_o, and upon compression leads to an internal field B_i. The flux conservation is given by

$$B_i \left[(r_c + \delta)^2 - r_s^2\right] = B_o (r_c + \delta)^2 \quad , \tag{E-1}$$

were δ is the shell thickness. Taking $\delta/r_c \ll 1$, Eq. (E-1) becomes

$$B_i \simeq B_o/(1 - r_s^2/r_c^2) \quad . \tag{E-2}$$

The flux that would ultimately diffuse through the shell at long times equals $B_o \pi r_s^2$. A characteristic time, τ_s, for this flux penetration into the conducting shell can be estimated from the expression

$$d\phi/dt \simeq \frac{B_o \pi r_s^2 (r_w^2 - r_s^2)}{\tau_s (r_c^2 - r_s^2)} = I_c R \quad . \tag{E-3}$$

Equation (E-3) includes the possiblity of placing the (vacuum) first wall

inside the conducting shell (i.e., $r_w < r_c$). For this case the amount of flux that is allowed to leave the system before the plasmoid would contact a surface is reduced by the ratio $(r_w^2 - r_s^2)/(r_c^2 - r_s^2)$. The current induced in the shell is given by

$$I_c = (B_i - B_o)\ell/\mu_o \quad , \tag{E-4}$$

where ℓ is the length of the plasmoid. The resistance of the shell is given by

$$R = \eta 2\pi r_c/\delta\ell \quad , \tag{E-5}$$

where η(ohm-m) is the resistivity of the conducting shell. Substituting Eqs. (E-2), (E-4) and (E-5) into Eq. (E-3) gives the following expression for the resistive diffusion time of the conducting shell

$$\tau_s = \frac{\mu_o}{2\eta}\frac{\delta}{r_c}(r_w^2 - r_s^2) \quad . \tag{E-6}$$

Typical values of the electrical skin time are summarized in Table E-I for two sample cases. The maximum thickness of a first-wall shell is taken to be 0.05 m, as dictated by neutronics considerations; the skin time for this case is computed from Eq. (E-6) to be ~ 0.3 s. Re-location of the conducting shell

TABLE E-I

COMPARISON OF FIRST-WALL VERSUS ROOM-TEMPERATURE CONDUCTING SHELL LOCATED OUTSIDE THE BLANKET REGION

CASE	r_s(m)	r_w(m)	r_c(m)	$\eta_{Cu}(\Omega\text{-m})$	δ(m)	τ_s(s)	P_α/P_η
$r_w = r_c$	0.7	1.0	1.0	$5.0(10)^{-8}$	0.05	0.3	4.3
$r_w < r_c$	0.7	1.0	1.4	$2.0(10)^{-8}$	0.1	1.1	59.

outside the neutron-moderating and tritium breeding blanket allows the use of a nearly room-temperature shell of a somewhat greater thickness (0.1 m). The shell thickness for the case where $r_c > r_w$ cannot be arbitrarily increased and in cross-sectional area must be significantly smaller than the crucial area where flux is being displaced; otherwise the conducting shell represents a significant energy sink for magnetic field and its effectiveness is thereby reduced. As seen from Table E-I, positioning the shell outside the blanket allows a factor of four increase in the estimated skin time, presuming that $r_c/r_s \simeq 2$ is adequate from the stability/equilibrium viewpoint.

The power dissipated in the conducting shell is directly related to the electrical skin depth and is given by

$$P_\eta(W) = I_c^2 R \simeq \frac{(B_i - B_o)^2}{\mu_o^2} \eta \frac{2\pi r_c \ell}{\delta} \quad . \tag{E-7}$$

When combined with Eq.(E-2), Eq. (E-7) reduces to

$$P_\eta(W) = \frac{\eta}{\mu_o^2} \frac{2\pi\ell}{\delta} \frac{r_s^4}{r_c^3} B_i^2 \quad . \tag{E-8}$$

The relative magnitude of this electrical loss is better appreciated if it is compared to the alpha-particle power, as given by

$$P_\alpha(W) = n^2 \langle\sigma v\rangle E_\alpha \pi r_s^2 \ell/8 \quad , \tag{E-9}$$

where the ($\beta \simeq 1$) plasma occupies one-half of the volume inside the separatrix, and $E_\alpha = 5.63(10)^{-13}$ J/fusion (3.5 Mev/alpha-particle). Using pressure balance and forming the ratio P_η/P_α gives for $\beta \simeq 1$

$$P_\alpha/P_\eta = 8.6(10)^{16} \frac{\delta}{\eta} \frac{r_c^3}{r_s^2} \frac{\langle\sigma v\rangle}{T^2} B_i^2 \quad . \tag{E-10}$$

The quantity $\langle\sigma v\rangle/T^2 \simeq 10^{-24}$ s/m^2 keV^2 is nearly constant over the temperature range (10-20 keV) of interest. Taking $B_i \sim 5$ T for illustrative purposes, the power ratio, P_α/P_η, is also listed in Table E-I. Substantial electrical dissipation can be associated with the presence of a conducting shell that is positioned near the first wall; this ohmic dissipation is greatly reduced if the shell is moved outside the blanket region, where it can be thick and operate at or near room temperature.

Another difficulty associated with locating the conducting shell at the first wall is the availability of translational power required for a moving ring reactor. This power is associated with the translation and cannot realistically be provided by the initial translational velocity, which according to the sample comparison given in Table E-I would have to be of the same order as the plasma thermal velocity ($v \sim 10^6$ m/s). The plasmoids must, therefore, be driven through the system using mirror coils or by relying on the direct conversion of alpha-particle power to translational power as the plasmoid moves through the reactor chamber of ever-enlarging radial dimension. Operating active mirror coils at or near the first wall or externally driving a first-wall conducting shell is considered unattractive because of severe thermal and neutron loadings.

Generation of the required translational power from the alpha-particle heating requires the expansion of the plasma during the burn translation. The thermodynamic work available in plasma expansion from an initial volume, V_i, to final volume, V_f, is

$$\Delta W_{PV} = \int_{V_i}^{V_f} p\,dV = \int_{V_i}^{V_f} (pV)\,dV/V \quad . \tag{E-11}$$

Assuming the plasma temperature remains essentially constant during this alpha-particle driven expansion, $pV = 2NkT$ is a constant, where N is the total number of plasma particles. Equation (E-11) is readily integrated to yield

$$\Delta W_{PV} = 3NkT \ \ell n(V_f/V_i)^{2/3} \quad . \tag{E-12}$$

For an equivalent conversion of all of the plasma internal energy, $\Delta W \sim 3NkT$, the volume ratio V_f/V_i must equal approximately 4.5. This substantial dimensional change alters the plasma density by 4.5 and lowers the fusion power density by roughly a fractor of ~ 20. A characteristic energy loss time associated with ohmic dissipation is defined as the ratio of plasma energy to ohmic power

$$\tau_L \sim \frac{\mu_o}{8} \frac{\delta}{\eta} \frac{r_c^3}{r_s^2} \quad , \tag{E-13}$$

where pressure balance ($\beta = 1$) and Eq. (E-2) has been used. Using the properties given in Table E-I for a hot (first-wall) conducting shell gives τ_L ~ 0.3 s. Therefore, the plasma must undergo large dimensional changes in a relatively short time in order to provide the necessary translational power from alpha-particle heating. This unattractive option provides further impetus to locate the shell outside of the blanket region, a conclusion that is further reinforced when the nonlinear time dependence of alpha-particle production and the largely unknown confinement properties of alpha-particles in the CT geometry are considered.

The reactor estimates presented herein, therefore, are based on a conducting shell positioned outside the first-wall/blanket region with r_c/r_s taken as ~ 2.0. The translation power is provided by moving mirror fields produced by tapering the conducting shell and extracting alpha-particle energy directly. In order to provide the necessary stabilization, the plasmoid must have a velocity, v, given by $\ell/v < \tau_s$, where τ_s is defined by Eq. (E-6) and ℓ is the total plasmoid length. The CTOR power level and physical size is estimated on the basis of these constraints.

APPENDIX F: STARTUP-MARSHALL COIL SYSTEM

A considerable body of information[28,32,41] exists on the optimum operation of a Marshall-coil system. Only the summary equations are given here. In a Marshall-coil operating near optimum efficiency the separatrix radius is expected to be generated for $x_s = 0.7$, with the final plasma length being one-half the coil length. The post-implosion density is then four times the initial filling pressure. The required terminal (capacitor) voltage is then

$$V_o(kV) = 3.5\ell\ P_o\ T^2 \quad , \tag{F-1}$$

where P_o is the initial filling pressure in mTorr and the other parameters are post implosion. The electric field is then

$$E_\Theta(kV/m) = 89 P_o^{1/2} T \quad . \tag{F-2}$$

Another quantity of interest is the risetime which can be expressed as

$$\tau(\mu s) = 3.3\ r_c/T^{1/2} \quad . \tag{F-3}$$

The energy, W_{BANK}, stored in the fast implosion bank that drives the FRΘP has been used to size qualitatively the CTOR reactor. Typically, values, of W_{BANK} much in excess of a hundred MJ have been judged to be impractical for a frequently pulsed system ($\tau_I \simeq 5$ s). The expression used to compute W_{BANK} is given in Appendix D.3.

★U.S. GOVERNMENT PRINTING OFFICE: 1981-0-777-022/42